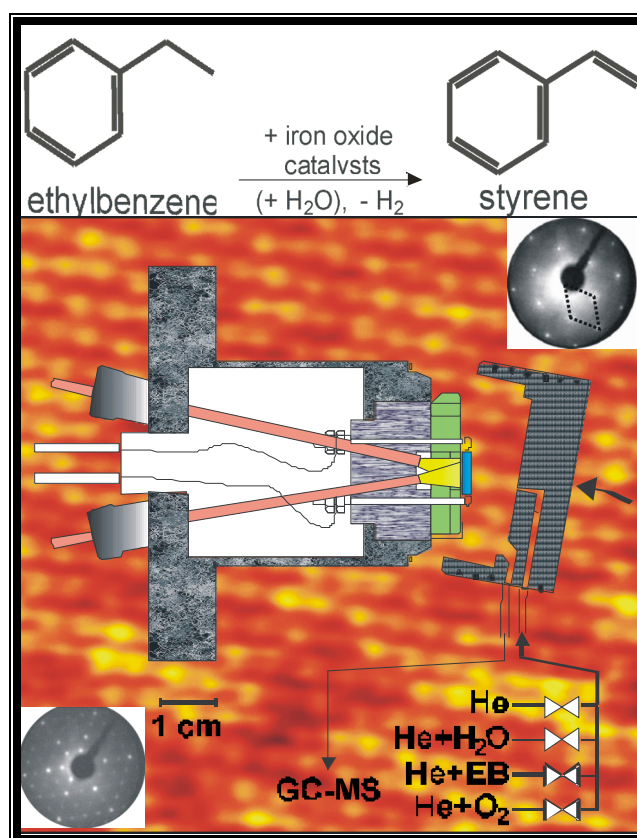


Styrene synthesis:

In-situ Characterization and Reactivity Measurements over Unpromoted and Potassium Promoted Iron Oxide Model Catalysts



By

Osama Shekhah

**Styrene synthesis:
In-situ Characterization and Reactivity
Measurements over Unpromoted and Potassium
Promoted Iron Oxide Model Catalysts**

Inaugural-Dissertation

zur Erlangung des Grades
Doktor der Naturwissenschaften
Am Fachbereich Biologie, Chemie, Pharmazie
Der Freien Universität Berlin

Vorgelegt in englischer Sprache

von

Osama Shekhah
Aus Jordanien
Berlin 2004

Gutachter:

**Prof. Dr. R. Schlögl
Fritz Haber Institut
der Max-planck-Gesellschaft
Abt. Anorganische Chemie
Faradayweg 4-6
14195 Berlin**

**Prof. Dr. K. Christmann
Freie Universität Berlin
Fachbereich Biologie, Chemie, Pharmazie
Institut für Chemie- Physikalische und Theoretische Chemie
Takustr. 3
14195**

Tag der Prüfung : 06-Mai-2004

Contents

Chapter-1: Introduction (styrene synthesis)

1.1	History.....	2
1.2	Reaction thermodynamics	3
1.3	Reaction kinetics and mechanism	5
1.4	Industrial catalysts composition.....	6
1.5	Catalyst deactivation.....	8
1.5.1	Coke deposition.....	8
1.5.2	Loss or redistribution of promoters.....	9
1.5.3	Oxidation state.....	10
1.5.4	Physical degradation	11
1.6	Alternative processes for styrene St synthesis (oxidative dehydrogenation of EB).....	11

Chapter-2 Iron oxide model catalysts: A surface science approach to styrene synthesis

2.1	Introduction	15
2.2	Preparation and characterization of iron oxide thin films.....	16
2.2.1	Geometric surface structures and stability ranges of iron oxides...	16
2.2.2	Potassium iron oxide compounds: Structure and stability ranges ..	21
2.3	Surface and structure Characterization	23
2.3.1	LEED and STM.....	23
2.3.2	AES measurements.....	26
2.3.3	Adsorption properties (TDS, UPS and NEXAFS).....	27
2.3.4	Low and medium pressure reactivity measurements.....	30
2.4	Aims and work strategy.....	32

Chapter-3 Experimental

3.1	Instrumentation setup.....	35
3.1.1	UHV analysis system.....	35
3.1.2	Sample transfer and heating.....	36
3.1.3	High pressure reaction cells.....	38
3.1.4	The reactor.....	49
3.1.5	The laser heating system.....	40
3.1.6	The gas supply system.....	41
3.2	Spectroscopic and microscopic characterization methods.....	42
3.2.1	LEED, TPO and AES.....	42
3.3	Preparation of epitaxial iron oxide thin films.....	43
3.4	Pressed powder samples of unpromoted Fe ₂ O ₃	45
3.4.1	Preparation of the pressed powder samples	45

3.4.2	Characterization of the pressed powder samples (BET, XRD and SEM-EDX).....	46
3.4.3	Cleaning of the pressed powder samples.....	47
3.4	Reaction experiments.....	47
Chapter 4 Results		
4.1	Blank reactivity experiments.....	51
4.2	Unpromoted model catalysts	51
4.2.1	Dehydrogenation reaction on Fe ₂ O ₃ (0001) and Fe ₃ O ₄ (111) model catalysts in presence of steam(normal conditions).....	51
4.2.2	Dehydrogenation reaction on Fe ₂ O ₃ (0001) model catalysts without steam (reductive conditions).....	56
4.2.3	Dehydrogenation reaction on Fe ₂ O ₃ (0001) model catalysts in presence of steam and oxygen (oxidative conditions).....	58
4.2.4	Dehydrogenation reaction on Fe ₂ O ₃ (0001) model catalysts in presence of steam and oxygen, effect of oxygen concentration on the activity.....	60
4.2.5	Dehydrogenation reaction on Fe ₂ O ₃ (0001) model catalysts in presence of steam. Oxygen on and off experiments	62
4.2.6	Dehydrogenation reaction on Fe ₂ O ₃ (0001) model catalysts in presence of steam and oxygen at different temperatures.....	64
4.3	Promoted iron oxide (KFe _x O _y) model catalysts	66
4.3.1	Dehydrogenation reaction on KFe _x O _y model catalysts in presence of steam (normal conditions), effect of potassium content.....	66
4.3.2	Carbon formation from reaction on KFe _x O _y promoted and unpromoted catalysts (normal conditions).....	69
4.3.3	The effect of reactivation with steam on the dehydrogenation reaction on potassium promoted (KFe _x O _y) model catalysts....	70
4.3.4	Dehydrogenation reaction on KFe _x O _y model catalysts in presence of steam and oxygen (oxidative conditions).....	73
4.3.5	Dehydrogenation reaction on KFe _x O _y model catalysts without steam (reductive conditions), effect of potassium promoting on the reduction of the catalyst.....	75
4.3.6	Dehydrogenation reaction on KFe _x O _y model catalysts in presence of steam. Oxygen on off experiments.....	77
4.3.7	Dehydrogenation reaction on KFe _x O _y model catalysts in presence of steam and oxygen, effect of oxygen concentration ..	77
4.3.8	Dehydrogenation reaction on KFe _x O _y model catalysts in presence of steam and oxygen at different reaction temperatures.....	79

4.4	Pressed hematite (Fe ₂ O ₃) powder samples	
4.4.1	Reaction on pressed powder samples in fixed bed reactor.....	80
4.4.2	Reaction on pressed powder samples in micro flow reactor	81
	a) Reaction in the presence of EB and steam in the feed.	84
	b) Reaction in the presence of EB, steam and oxygen in the feed.....	91

Chapter-5 Discussion

5.1	Unpromoted model catalyst.....	97
5.2	Promoted model catalyst.....	102
5.3	Pressed powder samples.....	113
5.4	Reaction model and mechanism.....	115
5.5	Conclusions.....	118

References

Acknowledgement

Curriculum vita

Abstracts

Acronyms

AES	Auger-Electron Spectroscopy
E_{ads}	Adsorption energy
EDX	Energy Dispersive X-ray Emission Analysis
EB	Ethylbenzene
St	Styrene
fcc	face centered cubic
FID	Flame Ionization Detector
hcp	hexagonal close packed
ISS	Ion Scattering Spectroscopy
k_i	rate constant
K	Equilibrium constant
LEED	Low-Energy Electron Diffraction
ML	monolayer
n	frequency factor
NEXAFS	Near-Edge X-ray Absorption Fine Structure
p	gas pressure
PEEM	Photoelectron Emission Spectroscopy
q_{st}	Isosteric heat of adsorption
r	Reaction rate
RDS	Rate Determining Step
SEM	Scanning Electron Microscope
SIMS	Secondary Ion Mass Spectrometry
STM	Scanning Tunneling Microscopy/Microscope
T	Temperature
TCD	Thermal Conductivity Detector
TDS	Thermal Desorption Spectroscopy
TEM	Transmission electron microscopy
TPO	Temperature Programmed Oxidation
UPS	Ultraviolet Photoelectron Spectroscopy
XPS	X-ray Photoelectron Spectroscopy
XRD	X-ray Diffraction

List of Schemes

Scheme(1)	Reaction network (products and byproduct) in the dehydrogenation of ethylbenzene. Toluene and benzene are formed by (1) dealkylation reaction, (2) Hydrodealkylation reaction, (3) steam dealkylation, the Coke formation and gasification with steam are also shown in (4).....	4
Scheme(2)	Schematic of the life cycle of styrene catalyst with potassium and no other promoter additives as found from in-situ and ex-situ characterization work on the working catalyst by Muhler et. al. [74].	10
Scheme(3)	Schematic drawing of the catalytic oxidative dehydrogenation over carbon nanofilaments, (1) adsorption of ethylbenzene, (2) dehydrogenation at basic centers, (3) desorption of styrene, (4) adsorption of oxygen and reaction with oh groups, (5) desorption of water.....	13
Scheme(4)	An illustrative scheme for the main and side reaction pathways of the dehydrogenation of EB over the unpromoted Fe ₂ O ₃ model catalyst.....	115
Scheme(5)	An illustrative scheme explaining the role of water in preventing the reduction of the catalyst and the gasification of carbon deposits.....	116
Scheme(6)	(a) The main and side reaction pathways over the potassium promoted iron oxide model catalyst. (b) The role of water in the gasification of carbon deposits and the acceleration of potassium loss.....	117

List of Figures

Figure 2.1	<i>p</i> (O ₂)- <i>T</i> phase diagram of the iron-oxygen system. The ranges where Fe ₃ O ₄ (A) and Fe ₂ O ₃ (B) films were grown on Pt (111) are indicated.....	16
Figure 2.2	Perspective side views of iron oxide crystal structures and top views cut parallel to the close packed oxygen layers. Bulk truncated (111) and (0001) surface structures terminated by outermost iron planes are shown. The surface unit cells are indicated. The top views are drawn with the full cation and anion sizes. In the side views the ionic radii were reduced by a factor of two.....	20
Figure 2.3	Structure models and layer arrangement for the ternary compound K ₂ Fe ₂₂ O ₃₄ (a) and KFeO ₂ (b). K is the large gray balls, O is the small dark balls and the Fe atoms are located in the center of the octahedral and the tetrahedral.....	22
Figure 2.4	LEED patterns at E=60 eV and top views of the corresponding surface structures of the different iron oxide films grown onto Pt(111). The unit cells in real and reciprocal space and the crystallographic directions in the cubic (a-c) and hexagonal crystal structures (d) are indicated. The epitaxial relationships between the oxide films and the substrate surface lattice are reflected in this figure.....	25
Figure 2.5	a)AES spectra of epitaxial iron oxide films grown onto Pt(111). (1)α-Fe ₂ O ₃ (0001), (2) the Fe ₃ O ₄ (111) before reaction, (3) Fe ₃ O ₄ (111) after reaction and (b) KFe _x O _y films are at least 100 Å thick.....	27
Figure 2.6	Energetic and structural results for EB (filled symbols) and St (open	

	<i>symbols) adsorption on different substrate films. (a) Desorption energies from TDS [28] for chemisorbed (g) and physisorbed (b) species and adsorbate arrangement at low coverages of the initially adsorbing species (b on FeO, g on the others). Shown is adsorbed EB, the arrangement for St is similar. Adsorbate structure for Fe_xO_y from NEXAFS measurements [11]. The arrangement on $K_xFe_{22}O_{34}$ is hypothetical. (b) Dependence of the desorption energy for the initially adsorbing species on the position of the first iron layer relative to the first oxygen layer.....</i>	28
Figure 2.7	<i>Mass spectrometer traces for EB and St under low pressure reaction conditions as indicated over poorly ordered and well ordered Fe_2O_3 samples. Water was admitted at $t=0$. The traces reflect the periods of EB admission.....</i>	31
Figure 2.8	<i>Mass spectrometric analysis of a batch reactor experiment at intermediate pressure conditions as indicated for three Fe_2O_3 model catalysts with differing surface quality. (1) well ordered, (2) intermediate order, (3) poorly ordered.....</i>	32
Figure 3.1	<i>Experimental setup, schematic, consisting of the preparation and analysis chamber (TDS) (1), PEEM (2) working at ultrahigh vacuum and the reactor chamber (3), working at pressures up to 1 bar. The sample on its support (figure 3) is moved by a magnetically coupled transfer rod. The transfer between the rod and the manipulator (M) or the reactor is accomplished by wobble sticks.....</i>	36
Figure 3.2	<i>a) Schematic side view of the magnetic transfer rod, the wobble stick, and the heating-cooling station in the transfer position, b) Front view photograph of the sample heating-cooling station on the manipulator.....</i>	37
Figure 3.3.	<i>A side view of the high pressure reaction cell with the flow reactor located inside. The sample is transferred fro UHV chamber using magnetic transfer line. With the help of wobelstick the sample is transferred and placed inside the reactor down in the chamber.....</i>	39
Figure 3.4	<i>Stagnation point micro-flow reactor for model catalysis at high pressure. 1: sample on sapphire support; 2: reactor cap; 3: fibber rods for coupling in laser irradiation; 4: thermocouple feed-through. (a) during insertion of the sample on a wobble stick, reactor cap withdrawn. (b) reactor cap closed, gas admission and analysis lines are schematically shown.....</i>	40
Figure 3.5	<i>The gas supply system used for the investigation of the styrene synthesis reaction carried out over iron oxide based catalysts in the presence of steam. All tubes are 1/16 inch in diameter. Helium (5.0) is used as carrier gas. The helium passes a 0.5 μm filter located directly in front of mass flow controllers (Bronkhorst).....</i>	42
Figure 3.6	<i>Schematic representation of the preparation of epitaxial iron oxide films Fe_xO_y and KFe_xO_y on Pt(111), accomplished by repeated cycles of iron deposition and subsequent oxidation.....</i>	44
Figure 3.7	<i>a) The pressed hematite (Fe_2O_3) powder samples in form of pellets. b) A side view of the pressed pellet (1) mounted on a sapphire sample support with the help of Pt clamps (2) designed for this purpose, the thermocouple is mounted on the Pt holder. c) A heating homogeneity test for the sample holder using a laser source at</i>	

	890K.....	46
Figure 4.1	Time dependence of the St conversion rate at 870 K, normal conditions, EB and H ₂ O in the feed, over (a) α -Fe ₂ O ₃ (0001). The labels A-C give the positions where sample characterization was performed (see table (4.1)).....	52
Figure 4.2	STM images of unpromoted Fe ₂ O ₃ model catalyst surface a) before, b) after 3 hours from reaction at normal reaction conditions, with the height profile along the indicated lines of each image is shown below.....	54
Figure 4.3	Time dependence of the St conversion rate at 870 K, normal conditions, EB and H ₂ O in the feed, over Fe ₃ O ₄ . The label D and E give the position where sample characterization was performed (see table (4.2)).....	55
Figure 4.4	Time dependence of the St conversion rate at 870 K, reductive conditions, EB and He in the feed, over Fe ₂ O ₃ . The labels F and G give the position where sample characterization was performed (see table (4.3)).....	57
Figure 4.5	AES spectrum of Fe ₂ O ₃ model catalyst after reaction at 870 K, reductive conditions, EB and He in the feed. Position G in Fig. (4.4).....	58
Figure 4.6	Time dependence of the St conversion rate at 870 K, oxidative conditions, EB, H ₂ O and O ₂ in the feed, over Fe ₂ O ₃ . The label H gives the position where sample characterization was performed (see table (4.4)).....	59
Figure 4.7	a) Conversion dependence of the St conversion rate at 870 K, oxidative conditions, EB, H ₂ O and O ₂ in the feed, over Fe ₂ O ₃ on EB/O ₂ molar ratio which is changed at the position labeled by numbers (1) 1:0.5, (2) 1:0.3, (3) 1:0.13, (4) 1:0.3 and (5) 1:0.13. b) Dependence of the steady state rate after 50 min of reaction at constant O ₂ /EB molar ratio(r_{50}). The dotted line is the estimated O ₂ /EB molar ratio which is theoretically needed to stabilize the high initial St conversion (see chapter 5).....	61
Figure 4.8	Deactivation dependence of the St conversion rate at 870 K, oxidative conditions, EB, H ₂ O and O ₂ in the feed, over Fe ₂ O ₃ after switching O ₂ on and off. The label I and J give the position where sample characterization was performed (see table (4.5)). For comparison, the deactivation when starting with a well ordered Fe ₂ O ₃ without O ₂ in the feed (from Fig. (4.1)) is shown in (a).....	63
Figure 4.9	The dependence of the St conversion rate at, oxidative conditions, EB, H ₂ O and O ₂ in the feed, over Fe ₂ O ₃	65
Figure 4.10	Time dependence of the St conversion rate at 870 K, normal conditions, EB and H ₂ O in the feed, over KFe _x O _y with a ($I_K/I_{Fe} \sim 2.2$). The lower curve shows the St conversion rate over unpromoted Fe ₂ O ₃ for comparison.....	66
Figure 4.11	Time dependence of the St conversion rate at 870 K, normal conditions, EB and H ₂ O in the feed, over KFe _x O _y with a) ($I_K/I_{Fe} \sim 0.9$), b) ($I_K/I_{Fe} \sim 4.2$).....	68
Figure 4.12	The build-up of carbon deposits over the unpromoted Fe ₂ O ₃ and potassium promoted (KFe _x O _y) catalyst ($I_K/I_{Fe} \sim 2.7$), expressed by the intensity ratios of the main Auger peaks of carbon to iron (I_C/I_{Fe})	

	<i>with time on stream (normal conditions).....</i>	70
Figure 4.13	<i>Time dependence of the St conversion rate at 870 K, normal conditions, EB and H₂O in the feed, over a potassium promoted (KFe_xO_y) with (I_k/I_{Fe}~ 2.2), a) before reactivation with water, b) after reactivation with water for ~15 min.....</i>	72
Figure 4.14	<i>Time dependence of the St conversion rate at 870 K, oxidative conditions, EB, H₂O and O₂ in the feed, over a potassium promoted (KFe_xO_y) model catalyst with (I_k/I_{Fe}=0.9).....</i>	76
Figure 4.15	<i>Time dependence of the St conversion rate at 870 K, normal conditions, over KFe_xO_y with (I_k/I_{Fe}= 1.9), after 2 hrs H₂O was switched, and the reaction is run under reductive conditions</i>	78
Figure 4.16	<i>Conversion dependence of the St conversion rate at 870 K, oxidative conditions, EB, H₂O and O₂ in the feed, over a KFe_xO_y (I_k/I_{Fe}~2.7) after switching O₂ off and on. B) Conversion dependence of the St conversion rate at 870 K, oxidative conditions, EB, H₂O, and O₂ in the feed, over KFe_xO_y (I_k/I_{Fe}~2.7), on EB/O₂ ratio, (1) 1:0.5, (2) 1:0.3, (3) 1:0.13 and (4) 1:0.3 and (5) 1:0.5.</i>	79
Figure 4.17	<i>The dependence of the St conversion rate at, oxidative conditions, EB, H₂O and O₂ in the feed, over a KFe_xO_y (I_k/I_{Fe}~2.8) on reaction temperature</i>	80
Figure 4.18	<i>Time dependence of the rate of St production (molecules. s⁻¹. cm⁻² BET surface) over pressed pellets of Fe₂O₃ powder in a fixed bed reactor. Reaction temperature 895 K, atmospheric pressure. : 1) EB/H₂O = 1:6, 2) EB/H₂O/O₂ = 1:6:0.4. In region A the GC measurement was switched from fast FID analysis to the combined FID-TCD method. This caused a shift in the baseline.....</i>	83
Figure 4.19	<i>SEM-EDX the pressed Fe₂O₃ powder of unused samples (a) and(b). (c) carbon contaminated part. (e) and (f) after cleaning treatment for 30 min.....</i>	86
Figure 4.20	<i>a) St conversion over the pressed powder Fe₂O₃ pellets used in the micro flow reactor at the same conditions like the model catalysts of 870 K and EB and H₂O in the feed (normal conditions). b) XRD spectrum of the powder sample after reaction. The asterisk mark the positions of Fe₃O₄ related diffraction peaks.....</i>	87
Figure 4.21	<i>SEM and EDX of the powder sample after reaction with EB and H₂O in the feed. The dashed line separates the red from the black parts of the sample.....</i>	87
Figure 4.22	<i>SEM and EDX of the powder sample after reaction with EB and H₂O in the feed. The back was black (Fe₃O₄). The Image (b) shows also small 0.1 μm particles.....</i>	88
Figure 4.23	<i>SEM and EDX of the black part of the powder sample after reaction with EB and H₂O in the feed (normal conditions). showing clearly the carbon deposits after reaction.....</i>	89
Figure 4.24	<i>SEM and EDX of the black part of the powder sample after reaction with EB and H₂O in the feed normal conditions).....</i>	90
Figure 4.25	<i>a) St conversion over the pressed powder Fe₂O₃ pellets used in the micro-flow reactor at the same conditions like the model catalyst of 870 K and EB and water in the feed, normal conditions. b) in the presence of oxygen in the feed, oxidative conditions,.....</i>	92
Figure 4.26	<i>SEM and EDX of the powder sample after reaction with EB and H₂O</i>	

	<i>in the feed. The sample was red (Fe_2O_3) and the EDX spectra shows that the surface is almost clean from the carbon deposits.....</i>	93
Figure 4.27	<i>SEM and EDX of the powder sample after reaction with EB and H_2O and O_2 in the feed, oxidative condition).....</i>	94
Figure 4.28	<i>SEM and EDX of the powder sample after reaction with EB and H_2O in the feed, oxidative conditions.....</i>	95
Figure 5.1	<i>Initial St conversion rate r_{in} and time constant for deactivation τ_{de} for samples with different initial K-content in terms of the Auger peak height ratio I_K/I_{Fe}. The composition where the ordered (2x2) structure is formed is indicated.....</i>	103
Figure 5.2	<i>Temperature dependence of the rate of styrene formation over the unpromoted and potassium promoted iron oxide model catalysts.....</i>	106
Figure 5.3	<i>EB dehydrogenation mechanism over the defects sites on the unpromoted (Fe_2O_3) [54]. Step 4 was found not to happen in case of reaction in presence of water alone. A side reaction (reduction of the Fe_2O_3 to Fe_3O_4) also occurs.....</i>	108
Figure 5.4	<i>Reaction mechanism proposed by Muhler et. al. [74] proposed reaction mechanism for the dehydrogenation of EB to St over potassium promoted iron oxide catalysts.....</i>	110
Figure 5.5	<i>Comparison of the EDX C-K intensity peak between pressed powder samples after different treatments. The unused fresh pressed powder is also shown for comparison. The spectra are normalized to equal Fe-L intensity.....</i>	114

List of Tables

Table 3.1	<i>Partial pressures and molar ratios of reactive gases in the gas feed for the used standard reaction conditions. The rest to the working pressure of 1 bar is He. The standard reaction temperature is 870 k, the standard total flow 25 ml min⁻¹.....</i>	48
Table 4.1	<i>LEED patterns and intensity ratios of the main Auger peaks of carbon, oxygen and iron before and after reaction for the unpromoted Fe_2O_3 model catalysts.....</i>	53
Table 4.2	<i>LEED patterns and intensity ratios of the main Auger peaks of carbon, oxygen and iron before and after different treatments for the unpromoted Fe_3O_4 model catalysts.....</i>	55
Table 4.3	<i>LEED patterns and intensity ratios of the main Auger peaks of carbon, oxygen and iron before and after reaction (reductive conditions) for the unpromoted Fe_2O_3 model catalysts.....</i>	57
Table 4.4	<i>LEED patterns and intensity ratios of the main Auger peaks of carbon, oxygen and iron for the unpromoted Fe_2O_3 model catalysts before and after reaction with water and oxygen in the..</i>	59
Table 4.5	<i>LEED patterns and intensity ratios of the main Auger peaks of carbon, oxygen and iron for the unpromoted Fe_2O_3 model catalysts after oxygen on - off experiments (Fig. (4.8a,b)).....</i>	64
Table 4.6	<i>LEED patterns and intensity ratios of the main Auger peaks of carbon, oxygen, potassium and iron before and after reaction with EB and H_2O in the feed (normal conditions) for the promoted (KFe_xO_y) model catalysts with different K-loading.....</i>	69
Table 4.7	<i>LEED patterns and intensity ratios of the main Auger peaks of</i>	

	<i>carbon, oxygen, potassium and iron before and after reaction with EB and H₂O in the feed for the promoted KFe_xO_y model catalysts effect of reactivation with steam.....</i>	<i>71</i>
<i>Table 4.8</i>	<i>LEED patterns and intensity ratios of the main Auger peaks of carbon, oxygen, potassium and iron before and after reaction with EB and H₂O in the feed for the promoted KFe_xO_y model catalysts with ($I_K/I_{Fe} \sim 2.8$), before and after reactivation with water for 15 min.....</i>	<i>73</i>
<i>Table 4.9</i>	<i>LEED patterns and intensity ratios of the main Auger peaks of carbon, oxygen, potassium and iron before and after reaction with EB, H₂O and O₂ in the feed (oxidative conditions) for the promoted KFe_xO_y model catalysts with ($I_K/I_{Fe} = 1.0$).....</i>	<i>74</i>
<i>Table 4.10</i>	<i>LEED patterns and intensity ratios of the main Auger peaks of carbon, oxygen, potassium and iron before and after reaction with EB and H_e in the feed over the promoted KFe_xO_y model catalysts</i>	<i>76</i>

Chapter-1

Introduction (Styrene synthesis)

1.1 History

Styrene (St) is one of the most important monomers in modern petrochemical industry. The world production at present is approximately 20 million tons per year. The styrene process was developed in the 1930s independently and simultaneously by BASF in Germany and by DOW Chemical in the USA. St is mainly used for the production of many different polymeric materials, the most important being polystyrene, styrene-acrylonitrile and acrylonitrile-butadiene-styrene (ABS). Another important application is in producing styrene-butadiene latex [1-3].

St is produced in industry mainly by two processes:

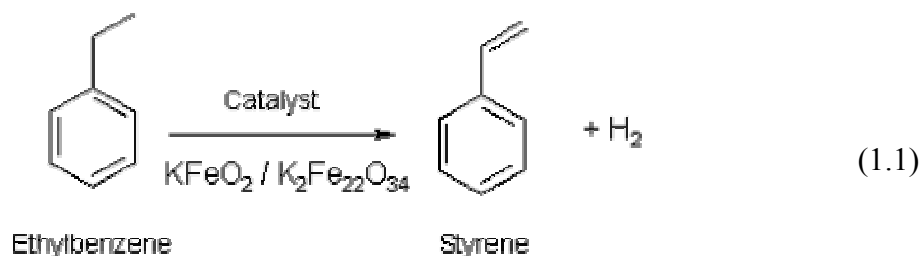
- I. dehydrogenation of ethylbenzene (EB) in presence of steam over iron oxide based catalysts
- II. as a by-product in the epoxidation of propene with ethylbenzene hydroperoxide and Mo complex-based catalysts.

The former process (I), accounts for more than 90% of the worldwide capacity. The catalytic dehydrogenation route, in which the potassium promoted iron oxide catalyst is typically used since 1957, produces most of the St. The process can be run industrially either adiabatically or isothermally over a fixed bed reactor in which the reactants are passed over the catalyst bed employing radial or axial flow [1,3].

Several catalysts, such as cobalt, copper, iron and zinc oxides, have been studied, both with and without promoters, but the potassium promoted iron oxide catalyst was found particularly efficient with respect to both selectivity and activity [2,3].

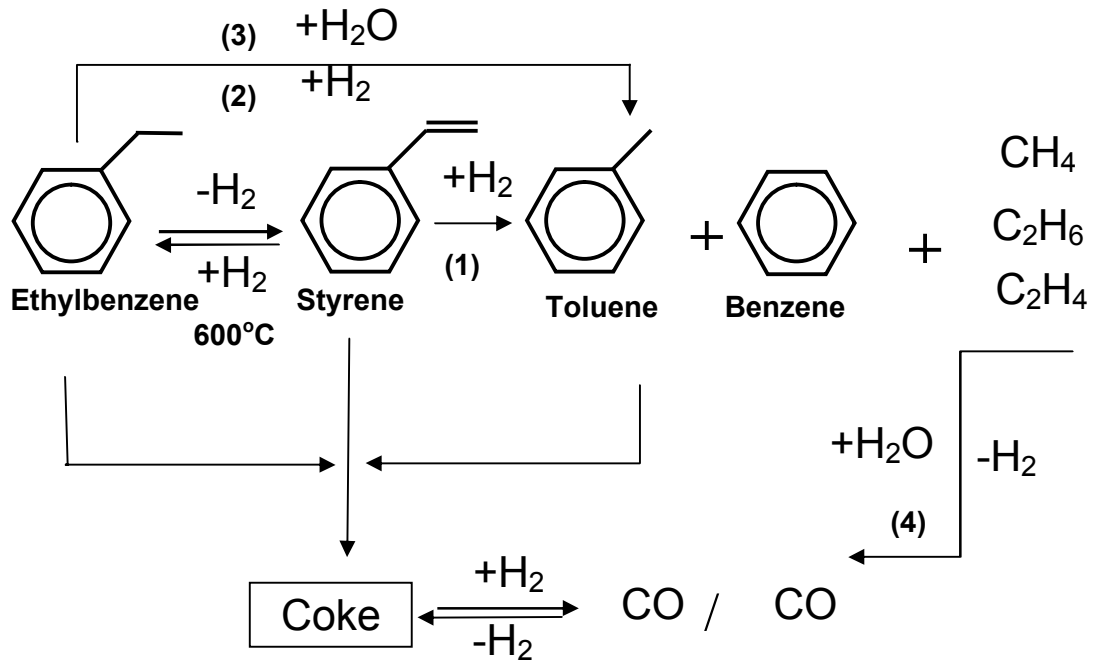
1.2 Reaction thermodynamics

The dehydrogenation reaction of EB to St (equation 1.1) is endothermic ($\Delta H=129.4$ kJ/mol) and equilibrium limited [4]



At room temperature, the reaction equilibrium is located far towards the educts side. It can be shifted towards the product side by increasing the temperature, which increases the equilibrium constant K due to the van't Hoff relationship and by reducing the pressure, since two moles of product are formed from one mole of EB. Therefore the technical St synthesis is run at around 600°C with an excess of steam, the steam-EB mixtures has a molar ratios from 5:1 to 12:1. Styrene plants run their reactors under isothermal or adiabatic conditions with flow rates that ensure short contact times in order to prevent polymerization of St [2]. The equilibrium EB conversion at 600°C and 0.1 bar pressure is ~ 83% [6], and conversions between 50 and 60% are obtained in technical reactors. The typical byproducts of the EB dehydrogenation are (~1%) benzene and (~2%) toluene formed by catalytic dealkylation (1) and hydrodealkylation (2) of EB, respectively, or they also can be formed by steam dealkylation (3) as shown in scheme (1).

All these reactions are accompanied by the formation of coke that can deactivate the catalysts. This coke is removed by combustion with steam according to the water-gas shift reaction (4) (scheme (1)) [7].



Scheme (1). Reaction network (products and byproduct) in the dehydrogenation of ethylbenzene. Toluene and benzene are formed by (1) dealkylation reaction, (2) hydrodealkylation reaction and (3) steam dealkylation. The Coke formation and gasification with steam is also shown (4).

The dilution of EB with superheated steam is believed to have several desired advantages for the styrene synthesis [1-3]:

- Shift of equilibrium towards higher EB conversion, (reduce educts partial pressure).
- Supplies part of the heat needed for the endothermic reaction.
- Decrease carbonaceous deposits by steam reforming reaction.
- Avoid catalyst over reduction and deactivation by controlling the valence state of iron i.e. prevent reduction to metallic state and limiting it to Fe_3O_4 under reaction conditions.

1.3 Reaction kinetics and mechanism

The kinetic aspects of the EB dehydrogenation were first investigated by Carra and Forni [8]. They described the reaction by a unimolecular Langmuir-Hinshelwood mechanism, where the reaction rate depends on the adsorption-desorption equilibrium of EB and St. The preferred adsorption of St can lead to a site-blocking effect by the product. These findings were supported by further studies of Lebedev et al. [9], Hirano [10,11], and Goodman [12].

It is believed that water vapor does not participate in the reaction itself, i.e. not involved in the rate determining step (RDS) of the reaction mechanism, but acts purely as inert dilution agent. However, as discussed above, it prevents the formation of inactive carbonaceous surface deposits and the reduction of the iron oxide to metallic iron by the produced hydrogen from reaction. Whereas Carra and Forni [8] assume one type of active sites generating all products in parallel reactions, several specialized reaction sites were postulated by Hirano [11]. For potassium promoted catalysts activation energies ranging between 120 and 190 kJ/mol were found. Since the activation energies for unpromoted α -Fe₂O₃ catalysts were similar (150 to 170 kJ/mol) [8, 11, 13, 14] identical active sites for the St formation on potassium promoted and unpromoted iron oxide catalysts were proposed [12, 14].

Muhler [15] has proposed that the active catalyst exposes a surface containing Fe³⁺ ions and K⁺ ions at a ratio of 1:1, which was already suggested in the model of Lee [2]. In analogy to the oxidative dehydrogenation of butadiene over MgFe₂O₄ catalysts [16], a two step mechanism associated with an acidic and a basic site is postulated for the dehydrogenation of EB over iron oxide and other transition metal oxide catalysts [15] [17]. Such a reaction scheme was also previously proposed by Muhler [18].

The C-H groups of the EB-ethyl group get deprotonated at basic oxygen sites and two hydroxyl groups are formed at the surface [19]. Simultaneously or subsequently an electron transfer to acidic Fe^{3+} sites is required before the styrene product molecule can desorb from the catalyst surface. Finally, the hydrogen atoms forming the two hydroxyl groups somehow leave the catalyst surface, the reduced Fe^{2+} species get reoxidized to Fe^{3+} , and the basic oxygen sites are reestablished for the next turnover cycle.

This picture agrees with results from an infrared spectroscopy study, where St formed by EB dehydrogenation was observed to be bonded to the catalyst surface through the vinyl group, whereas St adsorbed from the gas phase was bound via the aromatic ring [14]. In the proposed active KFeO_2 surface phase, potassium saturated Fe-O bonds increase the basicity of the oxygen sites. They also must be located in an adequate geometry with respect to the acidic Fe^{3+} sites, so that an effective deprotonation of the EB becomes possible.

1.4 Industrial catalyst composition

The dehydrogenation of EB to St in industry is carried out over potassium promoted iron oxide catalysts [4]. About 23 million tons of St are produced per year worldwide [5], which makes even small improvements of the catalysts profitable. An extensive review on the development of St synthesis catalysts was first published by Lee in 1973 [2], a recent review can be found in reference [2]. Potassium was found to increase the activity of pure Fe_2O_3 (hematite) catalysts by one order of magnitude, and is believed to play a role in the removal of carbonaceous surface deposits, by catalyzing the combustion of coke with steam [2,11,12]. Potassium carbonate (K_2CO_3) is believed to be the active site for the coke gasification process [20,21].

Technical catalysts are prepared from about 80 wt% of iron oxide Fe_2O_3 (hematite) and at least 10 wt% of potassium oxide. Small amounts of alumina and chromia act as structural promoters and increase the lifetime of the catalysts [6]. Oxides of V, Ce, W or Mo improve the selectivity, but their effect is only moderate [11]. Therefore any catalyst model can be restricted to systems consisting of iron and potassium oxides.

An interesting question is why potassium is clearly the most used alkali promoter in commercial styrene catalysts. Mross [20] indicates that this is most probably a result of secondary effects. Under operating conditions (part of) the iron oxide exists as Fe_3O_4 (magnetite). Smaller alkali ions like, e.g. Li^+ can more easily migrate into the magnetite lattice and are no longer available for the gasification reaction. Larger ions, such as Cs^+ , catalyze the gasification reaction so strongly that also more St is gasified, resulting in a lower selectivity. Another important effect, that has to be taken into account, is the melting point of the alkali compounds present on the catalyst. Mross [20] points out that the activity for graphite gasification is approximately inversely proportional to the melting points of the carbonates, i.e. $\text{Li}_2\text{CO}_3 > \text{Cs}_2\text{CO}_3 > \text{Rb}_2\text{CO}_3 > \text{K}_2\text{CO}_3 > \text{Na}_2\text{CO}_3$. Even the anion with which the alkali metal was formally associated was considered to be a factor of importance for the gasification activity.

After starting the catalytic reaction in a steam-EB mixture the EB conversion to St increases gradually. The steady state is reached within 20 hours time on stream [11,22]. This indicates formation of the active phase under reaction conditions. Mross proposed the working catalyst to consist of Fe_2O_3 , $\text{K}_2\text{Fe}_{22}\text{O}_{34}$, and Fe_3O_4 covered by a liquid film of KOH [20], a model that was ruled out later on. Hirano first proposed an active KFeO_2 phase to exist, based on X-ray diffraction (XRD) measurements on spent and "steamed" catalysts in the absence of air [11]. This proposal was also supported later by Muhler et al., who performed a detailed study on the catalyst

precursor and on the working catalyst, applying a variety of in-situ and ex-situ techniques [15,18,22]. The precursor material consists of α -Fe₂O₃ (hematite) and the ternary K₂Fe₂₂O₃₄ phase which has a cubic crystal structure similar to the spinel structure of Fe₃O₄ (magnetite). Muhler proposed that under reaction conditions the active catalyst phase is formed, which he believes that it could be of a thin KFeO₂ layer supported on a solid solution of K₂Fe₂₂O₃₄ in Fe₃O₄, and that K₂Fe₂₂O₃₄ phase could act as a storage medium from which the active surface is continuously supplied with potassium ions. Muhler found from ISS measurement that the ratio of K to Fe is 1:1 in the active phase and refer it to the KFeO₂, which is not completely true as the recent characterization of different iron-potassium phases showed.

1.5 Catalyst deactivation

For economical reasons most styrene production units have large capacities (in excess of 400,000 t per year). The catalyst slowly deactivates and typically needs to be replaced every 1-2 years. In view of the process scale this is a costly operation and, hence, much research has been dedicated to understanding of the deactivation mechanism and to developing possible method for preventing this deactivation. From a survey of almost all the literature on the studies done on this reaction four main reasons are generally brought forward for the catalyst deactivation [1] which are:

1.5.1 Coke deposition

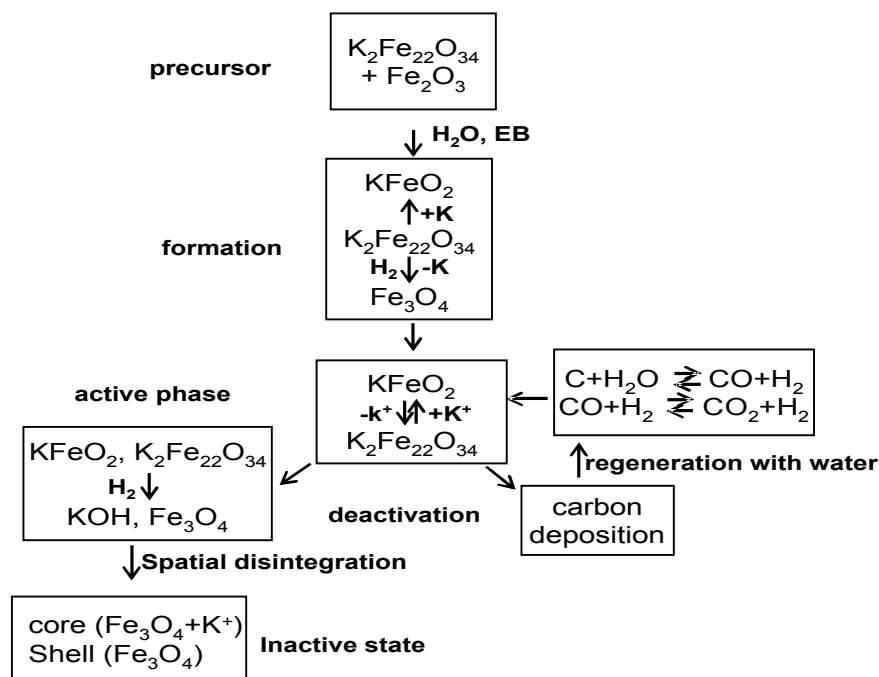
The amount of coke deposited on a typical (promoted) iron oxide catalyst during EB dehydrogenation depends on several factors. Besides the specific catalyst and promoters, important features are the steam to oil ratio (steam/aromatic ratio, usually designed as S/O) and the temperature used. When lower S/O ratios and higher temperatures are used [23-25], this leads to higher coke levels. Regeneration is done

by continuous gasification by steam. Often K_2CO_3 is proposed to be the catalyst for the coke gasification. Careful review of the literature data indicates that a steady state layer of coke is always present during typical styrene synthesis conditions.

1.5.2 Loss or redistribution of promoters

As already indicated, alkali metals are important promoters for the gasification of carbonaceous deposits. The most applied promoter in St synthesis is potassium, which as mentioned earlier plays many roles in this process. It is not surprising that its loss, changes in composition or migration will alter the catalytic properties of the iron oxide. At reaction conditions the potassium compounds, especially KOH, are slightly volatile, leading to a gas-phase transport to the outlet of the reactor. Also, potassium migrates from the exterior to the core of the catalyst pellet due to a temperature gradient resulting from the endothermicity of the reaction Lee [2,7]. Also recent studies by Holmeid et.al, indicated that potassium could be lost also as neutral atoms or as excited states [26,27]

Muhler investigated the life cycle of the catalyst and proposed a model which is shown schematically in scheme (2). The potassium migration causes a continuous solid-state transformation of the catalyst during its lifetime. An irreversible deactivation is caused by spatial disintegration of the iron oxide and the potassium compound leading to a core of potassium rich Fe_3O_4 and a shell of only Fe_3O_4 , by the total loss of potassium, and by the reduction of $KFeO_2$ and $K_2Fe_{22}O_{34}$ into Fe_3O_4 and KOH. A reversible deactivation of the catalyst is caused by blocking of active surface sites with CO_2 adsorbed in competition with the reactant, as well as by the formation of inactive carbonaceous surface deposits. These species can be removed by a steam treatment. A catalytically active role of the carbonaceous species was never discussed in literature for the non-oxidative dehydrogenation process.



Scheme (2). Schematic of the life cycle of styrene catalyst with potassium and no other promoter additives as found from in-situ and ex-situ characterization work on the working catalyst by Muhler et. al [15].

1.5.3 Oxidation state

Hydrogen is formed (locally) at the catalyst surface, whereas steam and hydrocarbons are present in the feed. This results in a complex and dynamic system, especially at the high temperatures ($600^\circ C$) involved. Moreover, solid-state changes, that are kinetically slow, can still take place considering the typical lifetime of a St catalyst [2,28-32].

Overall, the feed composition is considered reducing at temperatures above $600^\circ C$. Lee [2] observed that the iron compound in a fresh catalyst consisted of mainly Fe_2O_3 (hematite) which is reduced to Fe_3O_4 (magnetite). He noted that Fe_3O_4 is more selective. This was also seen by Yang et al.. Muhler et al. found also that the $KFeO_2$ is also slowly reduced with time on stream to Fe_3O_4 . However, he proposed that the $K_2Fe_{22}O_{34}$ could serve as a potassium storage medium supplying the surface with a

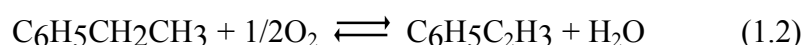
near-monolayer coverage of potassium ions and preventing the reduction of Fe⁺³ ions. Irreversible deactivation occurs when the K₂Fe₂₂O₃₄ becomes exhausted.

1.5.4 Physical degradation

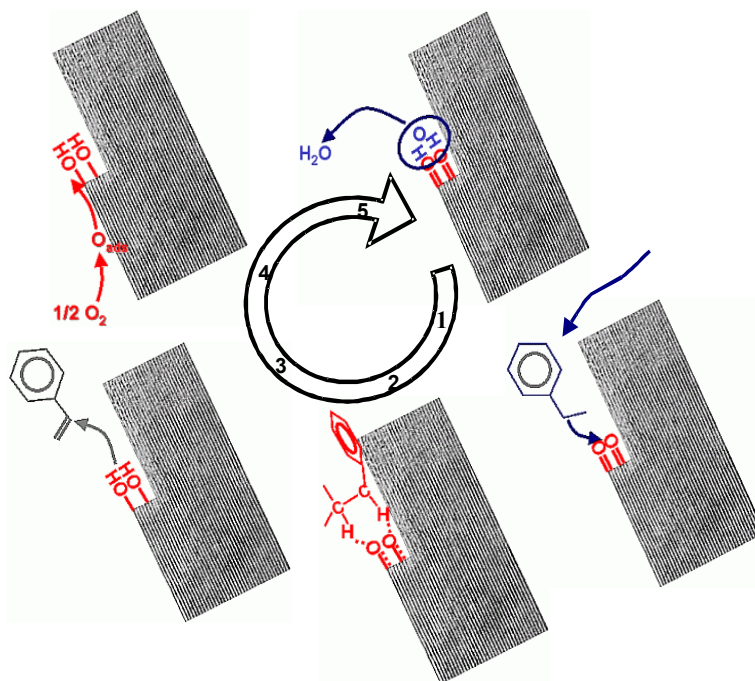
The physical degradation of iron oxide catalyst during St synthesis has been recognized as an important problem [1]. The cause is closely related to the change in the oxidation state of the iron oxide (Fe⁺³ to Fe⁺²). Under reaction conditions the Fe₂O₃ is reduced to Fe₃O₄. Fe₂O₃ has a hexagonal lattice structure whereas Fe₃O₄ has a cubic lattice structure. This lattice structure change, along with the high mechanical forces in the catalyst bed, results in degradation or pulverization of the catalyst particles. Also, the slow density changes due to migration of the potassium promoter contribute to the weakening of the catalyst crush strength. Also the potassium depletion leads to higher coking levels and the pores of the catalyst can become plugged. The overall result of the above processes is that the pressure drop over the catalyst bed becomes larger, which adversely affects the selectivity and the yield of the working catalyst [1,32]

1.6 Alternative processes for styrene synthesis-Oxidative dehydrogenation of EB

Oxidative dehydrogenation is one of the many alternative techniques which have been proposed to overcome some of the disadvantages of the styrene synthesis by EB dehydrogenation like the high endothermicity of the reaction and product separation. Alkhazov et al. proposed that carbonaceous deposits which were formed in the first hours of time on stream on the surface of acidic catalysts act as the real active centers for the oxidative dehydrogenation of EB to St [33]:



Since then, there has been a great deal of interest in oxidative dehydrogenation schemes [34- 37]. The formation of water as a byproduct makes the process exothermic and thermodynamically enables complete conversion. This also reduces the energy consumption for the St synthesis over iron oxide catalysts considerably. In more recent studies various carbon materials exhibited higher activities and selectivities than iron oxide based catalysts at much lower reaction temperatures than 600°C [38,39]. For example, 80% conversion and 90% selectivity were achieved at 350°C over ultrahigh surface area carbon molecular sieves [42]. The oxidative dehydrogenation of EB was investigated over various oxide compounds [43, 44] and phosphates [43-46], the carbonaceous layers that form on the surface were found to act as the true catalyst. This "active coke" is an organic polymer that is formed from EB and oxygen in the feed and contains carbon, hydrogen and oxygen. XPS and SIMS measurements indicated the presence of quinone-like groups [47, 48]. The oxygen atoms in these quinone groups can dehydrogenate EB forming water as a product, as proposed in a speculative reaction mechanism by Emig [43] in scheme (3) [49,50]. About 50% of the surface is supposed to be covered by these carbonaceous species, after equilibrium between their formation and combustion has established. The formation of this active coke was found to depend on the surface acidity of the inorganic support [52, 53]. Basic substrates like magnesia and titania are nearly inactive, and very acidic sites are also ineffective [43, 54]. Generally, sites with a Lewis acidity of moderate strength are considered to form the active coke most effectively [46]. So far there is no evidence that carbonaceous overlayers act as the true catalyst for the non-oxidative dehydrogenation of EB over iron oxide based catalysts



Scheme (3). Schematic drawing of the catalytic oxidative dehydrogenation over carbon nanofilaments, 1- adsorption of EB, 2-dehydrogenation at basic centers, 3- desorption of St, 4- adsorption of oxygen and reaction with OH groups, 5- desorption of water

Chapter 2

*Iron oxide model catalysts:
A surface science approach
towards styrene synthesis*

2. The Model catalysis approach

2.1 Introduction

Here, I will try to review the model catalysis approach applied to the investigation of the catalytic dehydrogenation of EB to St which has been done so far in our research group over unpromoted and potassium-promoted iron oxide model catalysts. The catalyst is complex. Since the divalent Fe^{2+} and the trivalent Fe^{3+} state are similarly stable, there exist several stable or meta-stable oxide phases. Addition of K produces several stable or meta-stable ternary KFe_xO_y phases [1].

The idea is not new to overcome the pressure gap by combination of a conventional UHV chamber with a high-pressure cell [56-58]. Preparation and characterization of a catalytically interesting surface is performed in UHV using the methods of surface science and after that the sample is transferred under vacuum into a high-pressure cell where catalytic conversion measurements can be performed at pressures far enough away from UHV to yield information relevant to real catalysis conditions.

The basic idea of model catalysis as we apply it is to prepare well defined model catalyst samples and to characterize their surface structure and composition as well as their adsorption-desorption properties for the relevant gases. Then the samples are transferred under vacuum into a reactor which allows determining the catalytic properties (conversion, selectivity, deactivation behaviour) in-situ under realistic temperature and pressure conditions. After that, the samples are transferred back into the main UHV chamber for post-reaction analysis [74].

2.2 Preparation and characterization of iron oxide thin films.

2.2.1 Geometric surface structures and stability ranges of iron oxides

A number of different phases with different stoichiometries and crystal structures were prepared from iron and oxygen (the detailed preparation procedure is explained in the experimental chapter 3) these phases are: FeO (wustite), Fe₃O₄ (magnetite) and α -Fe₂O₃ (hematite), which occur naturally. Under thermodynamic equilibrium their stability ranges depend on the ambient oxygen gas pressure $p(\text{O}_2)$ and on the temperature T . These stability ranges for pressures below 1 bar are shown in the phase diagram for the iron-oxygen system in Fig. (2.1) [59,61]. It was calculated using commercial software [60] for $p(\text{O}_2)$ - T ranges used in the preparation of the iron oxide model catalyst films.

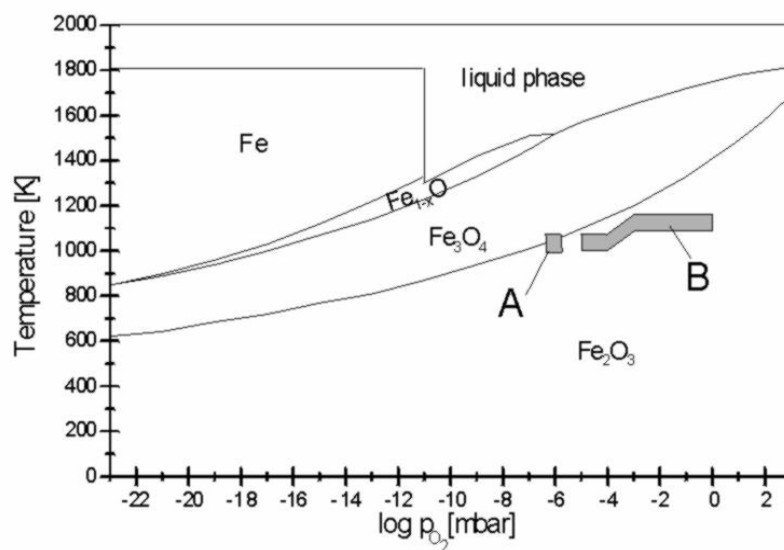


Fig. (2.1). $p(\text{O}_2)$ - T phase diagram of the iron-oxygen system. The ranges where Fe₃O₄ (A) and Fe₂O₃ (B) films were grown on Pt(111) are indicated.

Fig. (2.2) shows a perspective side and top views of the three iron oxide crystal structures studied extensively earlier in our group [74]. They expose surface planes as obtained by truncating the bulk structure. The side views show the hexagonal iron and oxygen (111) and (0001) planes stacked consecutively along the [111] and [0001]

crystal directions, the top views show the unreconstructed (111) and (0001) surfaces terminated by topmost iron layers. The two-dimensional surface unit cells are also indicated.

FeO wustite crystallizes in the sodium chloride structure containing four formula units in the cubic unit cell. The large O^{2-} anions form a close packed fcc sublattice with the small Fe^{2+} cations located in the interstitial sites. All iron ions are octahedrally coordinated to oxygen. Under thermal equilibrium this phase is stable only at low pressures (Fig. (2.1)) and for temperatures above 843 K [64]. In this oxide the oxygen and iron (111) planes form ideal two-dimensional hexagonal lattices with an inter-atomic distance of 3.04 Å, which corresponds to the lattice constant of the hexagonal unit cell on the unreconstructed FeO(111) surface. Along the [111] direction the iron and oxygen (111) planes form the cubic ABC stacking sequence with an interlayer distance of 1.25 Å. The iron-oxygen bond length is 2.16 Å.

Fe_3O_4 magnetite is ferromagnetic and crystallizes in the inverse spinel structure [62]. The oxygen anions form a close-packed fcc sublattice with Fe^{2+} and Fe^{3+} cations located in the interstitial sites. One cation site is tetrahedrally coordinated to oxygen and is occupied only by Fe^{3+} ions. The other site is octahedrally coordinated to oxygen and is occupied by equal numbers of Fe^{2+} and Fe^{3+} ions. The cubic unit cell has a lattice constant of 8.396 Å and contains eight formula units which can be written as $(Fe^{3+})_8[Fe^{3+} Fe^{2+}]_8O_{32}$. The parentheses () denote the tetrahedrally coordinated Fe^{3+} ions, often labeled A sites, and the brackets [] denote the octahedrally coordinated Fe^{2+} and Fe^{3+} ions or B sites. The high electrical conductivity of magnetite at room temperature is attributed to electron hopping processes between the Fe^{2+} and Fe^{3+} ions.

Along the [111] axis of Fe_3O_4 the hexagonal oxygen planes form a cubic ABC stacking sequence. Between the oxygen (111) planes one Kagomé, three hexagonal (mix-trigonal) iron layers alternate. In the Kagomé layer $\frac{3}{4}$ of the octahedrally coordinated B sites are occupied by Fe^{2+} and Fe^{3+} species. The unoccupied sites in these planes are 5.94 Å apart forming an ordered hexagonal lattice. In the mix-trigonal layers only $\frac{1}{4}$ of all sites are occupied within each subplane: The central plane contains octahedrally coordinated Fe^{3+} and Fe^{3+} species located on B sites, the other two planes tetrahedrally coordinated Fe^{3+} species located on A sites. The interatomic iron-iron distance within these planes is also 5.94 Å, which corresponds to the lattice constant of the two-dimensional surface unit cell of $\text{Fe}_3\text{O}_4(111)$ indicated in Fig. 2.2. There is a slight deviation of the oxygen anion positions within the (111) planes from an ideal hexagonal arrangement of this surface, due to two types of oxygen anions which are denoted O_a and O_b in Fig. (2.2). The O_a species are located 0.04 Å closer to the topmost single octahedrally coordinated iron layers than the O_b species. The average oxygen-oxygen interatomic distance within the (111) planes is 2.97 Å. If we consider weighted values for the O_a and O_b sublayers, neighboring oxygen (111) planes separated by the Kagomé layer are 2.37 Å apart, oxygen planes separated by the three mix-trigonal layers are 2.48 Å apart. This leads to a distance of 4.85 Å between every second oxygen layer, which corresponds to the distance between equivalent (111) surface terminations of Fe_3O_4 . The iron sub-planes of the mix-trigonal iron layers are separated by 0.6 Å. The iron-oxygen bond lengths for tetrahedrally coordinated iron is 1.88 Å, that for octahedrally iron is 2.07 Å. The (111) surface plane is stable and frequently occurs on naturally grown crystals which assume octahedral shapes [64].

α -Fe₂O₃ hematite is the only iron oxide phase that is stable at room temperature in thermodynamic equilibrium with ambient oxygen atmospheres. It crystallizes in the corundum structure with the hexagonal unit cell containing six formula units. The lattice constants are $a=5.035$ Å and $c=13.72$ Å [64]. The oxygen anions form an hcp sublattice with ABAB stacking. The Fe³⁺ species in the interstitials are arranged in distorted octahedra and form two sublayers. The interatomic distance within these iron layers is 5.03 Å, which corresponds to the lattice constant of the two-dimensional unit cell of an unreconstructed (0001) surface, as indicated in the top view of Fig. (2.2). The oxygen anion positions within the (111) planes also deviate slightly from an ideal hexagonal arrangement. The average oxygen-oxygen interatomic distance is 2.91 Å. Due to the distortion of the octahedra there are two different iron-oxygen bond lengths, 1.96 Å and 2.09 Å. The two iron subplanes in-between the oxygen planes are separated by 0.6 Å. The distance between two oxygen planes is 2.29 Å, which corresponds to the distance between equivalent (0001) surface terminations.

The quasi-hexagonal surfaces of the three iron oxide phases in Fig. (2.2) form three different unit cells provided no reconstructions occur. They have lattice constants of 3.04 Å (FeO), 5.92 Å (Fe₃O₄) and 5.03 Å (α -Fe₂O₃). The α -Fe₂O₃(0001) unit cell is rotated by 30° with respect to the others. Therefore the LEED patterns of these surfaces can be used to identify the different iron oxide phases.

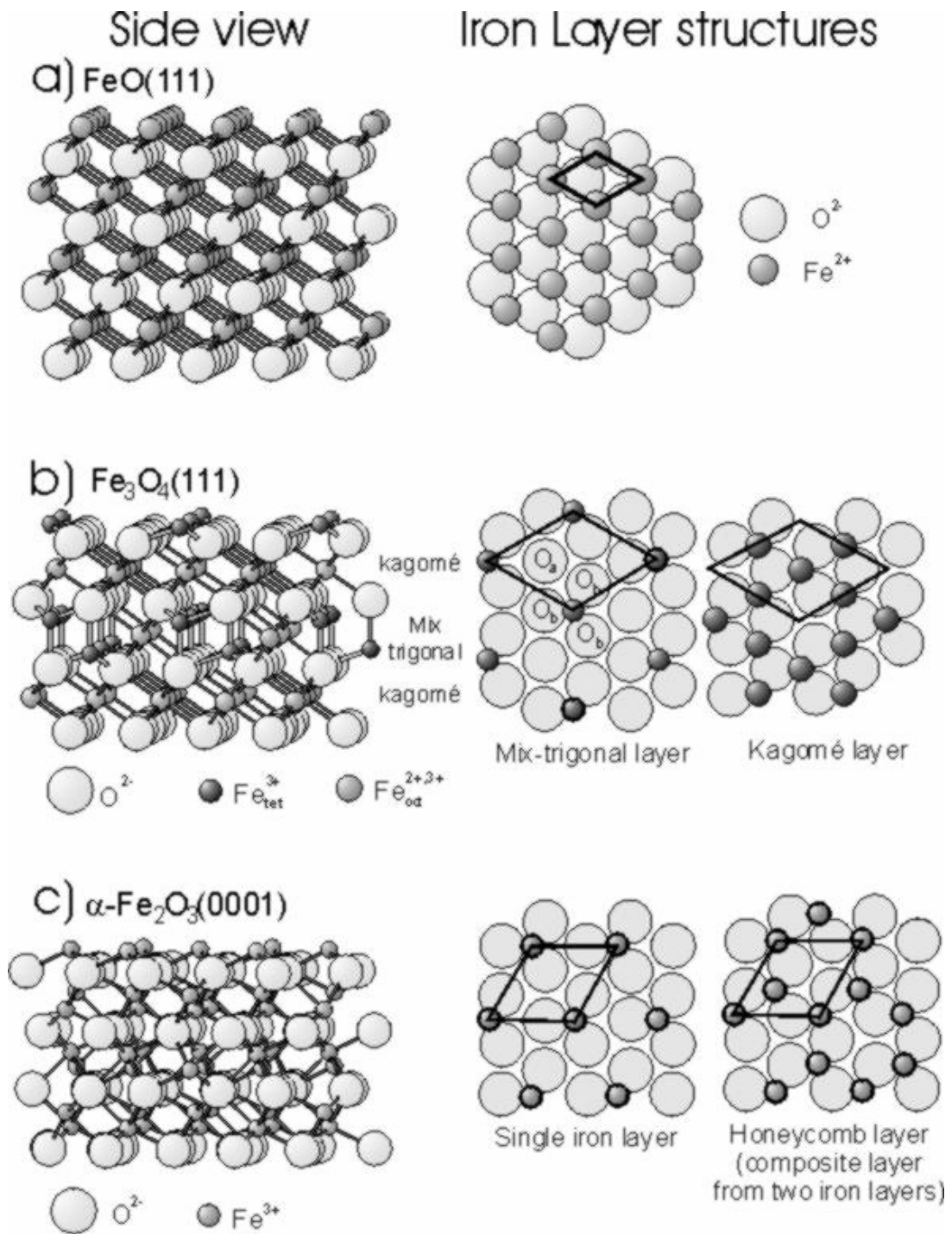


Fig. (2.2). Perspective side views of iron oxide crystal structures and top views cut parallel to the close packed oxygen layers. Bulk truncated (111) and (0001) surface structures terminated by outermost iron planes are shown. The surface unit cells are indicated. The top views are drawn with the full cation and anion sizes. In the side views the ionic radii were reduced by a factor of two.

2.2.2 Potassium-Iron oxide compounds: structures and stability ranges

Several ternary compounds containing both iron oxides and potassium are described in literature like KFeO_2 [67], and various phases with the general composition $\text{K}_2\text{O} \cdot n\text{Fe}_2\text{O}_3$ ($n=2, 5, 6, 7, 11$). Very likely, these compounds are mixtures of hexagonal phases with ideal compositions $\text{K}_2\text{Fe}_4\text{O}_7$, $\text{K}_2\text{Fe}_{22}\text{O}_{34}$ and $\text{K}_4\text{Fe}_{22}\text{O}_{34}$. The formation of KFeO_2 in the technical catalyst was found to proceed with a high yield between 873-1073 K while the transformation of KFeO_2 to $\text{K}_2\text{Fe}_{22}\text{O}_{34}$ ($\text{k-}\alpha\text{-Fe}_2\text{O}_3$) starts around 1023 K. All results in literature suggests that the ternary phases KFeO_2 and $\text{KFe}_{22}\text{O}_{34}$ ($x=2.4$) may occur as stable phases when K_2O and Fe_2O_3 are brought into contact. Similar results are expected when potassium is deposited on Fe_3O_4 and annealed. Stability regions of these ternary compounds also in dependence of the water partial pressure were investigated in our group [22], It showed that below a phase boundary ranging from 447 K at 10^{-11} mbar to 626 K at 10^{-5} mbar, KOH is formed while beyond this phase boundary KOH decomposes and potassium desorbs into the gas phase.

Potassium-promoted thin films were prepared and studied earlier [72,73]. K was deposited using a SAES getter source on Fe_3O_4 or Fe_2O_3 films, followed by annealing in vacuum or at $p(\text{O}_2)=10^{-6}$ mbar. The most stable K-Fe-O phases are the K-rich KFeO_2 (K-ferrite) and the K-poor $\text{K}_x\text{Fe}_{22}\text{O}_{34}$ with $x=2$ (K- β -ferrite) or $x=4$ (K- β' -ferrite). $\text{K}_x\text{Fe}_{22}\text{O}_{34}$ has a hexagonal layer structure which can be considered as a sequence of spinel-like blocks $-(\text{O}_4\text{-Fe}_3)_3\text{-O}_4-$ etc. as in Fe_3O_4 , separated by $-\text{Fe-K}_x\text{O-Fe-}$ layers. Lower K-contents ($x<2$) can be achieved either by increasing the thickness of the spinel blocks, thus continuously approaching the pure Fe_3O_4 , or by a decrease in the occupation of the potassium sublayers. Because of the similarity of the spinel blocks with the Fe_3O_4 spinel structure, the lattice constant of the $\text{K}_x\text{Fe}_{22}\text{O}_{34}(0001)$ and

$\text{Fe}_3\text{O}_4(111)$ surfaces are almost identical and epitaxial growth is easy. KFeO_2 is tetragonal without any layered character and does not fit with the lattice of Fe_3O_4 . In its bulk, the K, Fe and O atoms are quite homogeneously distributed. A structure model for $\text{K}_2\text{Fe}_{22}\text{O}_{34}$ (a) and KFeO_2 phases (b) is shown in Fig. (2.3).

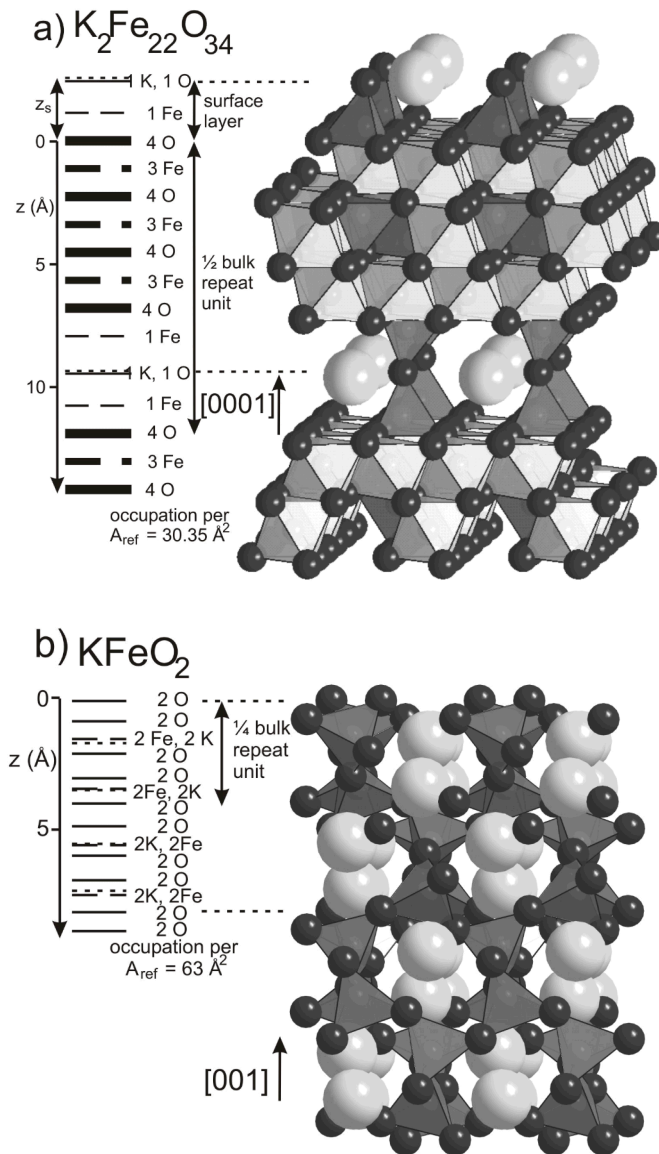


Fig. (2.3) Structure models and layer arrangement for the ternary compound $\text{K}_2\text{Fe}_{22}\text{O}_{34}$ (a) and KFeO_2 (b). K is the large gray balls, O is the small dark balls and the Fe atoms are located in the center of the octahedral and the tetrahedral.

The preparation conditions, composition and stability of these phases have been mapped using XPS, AES, which allows the quantitative determination of the elemental composition within the analysis depth of about 25 Å [72,73]. The most important composition steps observed when a thick layer of K is deposited on a Fe₃O₄(111) thin film at 200 K and annealed stepwise up to 970 K are the following :

- At 700 K a uniform KFeO₂ phase has formed.
- At 800-900 K, a layered structure has formed with a thin KFeO₂ layer structure on the top of a K-poorer K_xFe₂₂O₃₄ phase (0 < x < 2). The analogy with the layered structure of the working real catalyst as proposed by Muhler [15,22] is sticking.
- At 970 K, a well ordered K_xFe₂₂O₃₄ (0001)-(2x2) phase (x ≤ 0.67) is left.
- Beyond 700 K, addition of H₂O accelerates the removal of potassium from the films considerably.

2.3 Surface structure characterization:

2.3.1 (LEED and STM)

Fig. (2.4) shows the LEED patterns, STM images and surface structure models of those model catalyst layers which form ordered surfaces. The hexagonal oxygen layers are very similar in all cases with O-O distances varying only between 0.290 nm in Fe₂O₃, 0.296 nm in Fe₃O₄ and K_xFe₂₂O₃₄ and 0.304 nm in bulk FeO. The thin FeO layers on Pt have expanded lattice constants. The strong differences in the LEED patterns and the STM images result therefore from the different arrangement of the Fe atoms between the oxygen layers. Typical for the quite thin FeO(111) layers (shown is a film only one Fe-O bi-layer thick) are the satellite patterns around the integral order spots in LEED and the Moiré pattern of the STM image. Both are a result of the low film thickness and the misfit between the Pt(111) and the FeO(111) lattice. The

satellite spots result from multiple scattering involving the Pt and FeO lattice. The Moiré pattern reflects the different positions of the Fe atoms on the Pt lattice, periodically changing between on-top, bridge and threefold hollow site positions. All three kinds of sites occur in the shown structure because the FeO layer is rotated with respect to the Pt substrate. Photoelectron diffraction studies [74] have shown that the surface is oxygen terminated. However, the bright dots in STM reflect the positions of the Fe atoms underneath which show both unoccupied and occupied levels near the Fermi level [74]. For details of the structure see ref. [74].

The $\text{Fe}_3\text{O}_4(111)$ surface has a threefold symmetry. Mostly, however, two domains rotated by 60° with respect to each other are equally distributed so that the LEED pattern has six- fold symmetry. As for FeO, the STM image reflects the surface unit cell. Again, the bright spots correspond to surface Fe atoms. They are quite clear on $\text{Fe}_3\text{O}_4(111)$ because this surface Fe forms the top layer as proven by a LEED structure analysis and indicated in the model.

The surface unit cell of $\alpha\text{-Fe}_2\text{O}_3(0001)$ is again different. The STM image is again formed by Fe derived spots but the contrast is lower than on Fe_3O_4 . The reason is that the surface is oxygen-terminated or possibly even hydroxylated as a LEED structure analysis has shown [74]. Also the decrease in the intensity of the spots or there broadening and the high background in the LEED images gave an indication of the increase of the surface roughness or disorder [61].

Depending on the amount of deposited K and the annealing temperature, different ternary K-Fe-O compounds are formed. Already at 300 K, the deposited K diffuses into the bulk and at 700 K, the K-rich KFeO_2 phase forms uniformly as concluded from quantitative XPS measurements [73]. It has, however, no long-range order and no LEED patterns are formed [72].

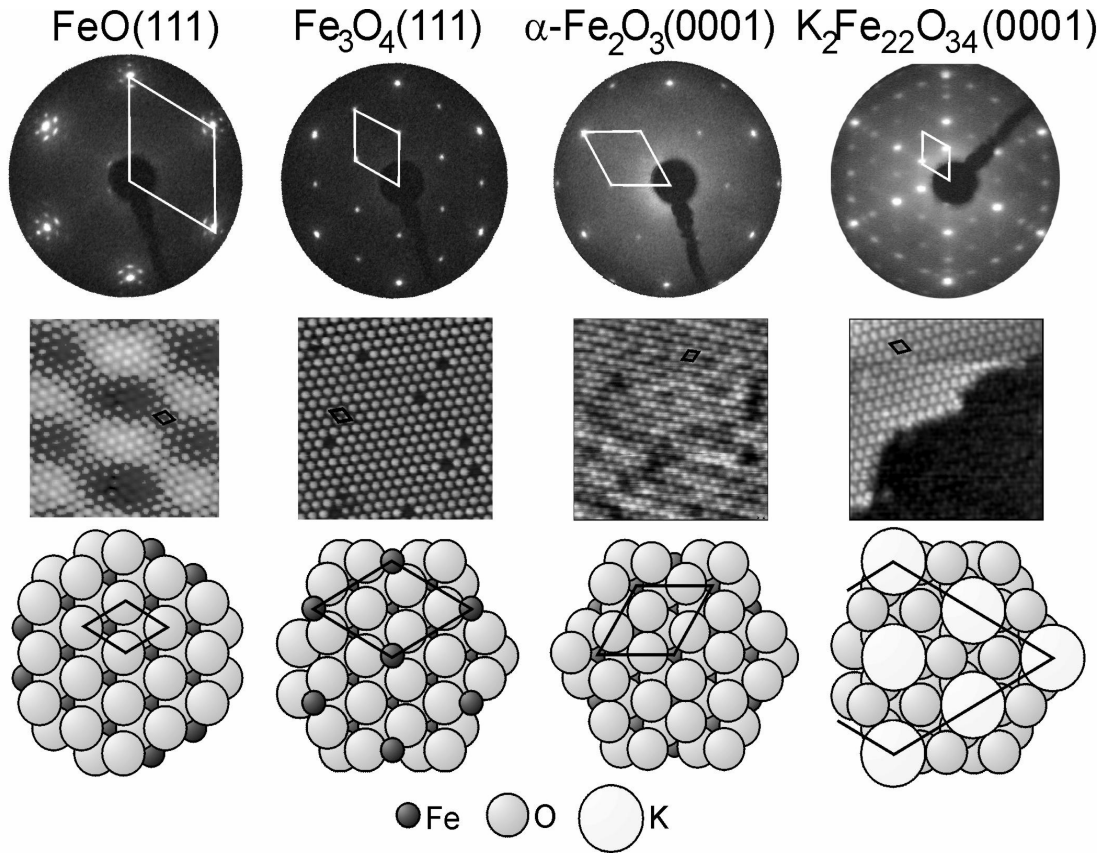


Fig.(2.4). LEED patterns at $E=60$ eV and top views of the corresponding surface structures of the Pt(111) substrate (a), and of the different iron oxide films grown onto Pt(111) (b) to (d). The unit cells in real and reciprocal space and the crystallographic directions in the cubic (a-c) and hexagonal crystal structures (d) are indicated. The epitaxial relationships between the oxide films and the substrate surface lattice are reflected in this figure.

STM imaging is difficult and only possible on a very thin (2 nm) film because of the insulating character of this compound. The film is rough and atomic resolution was not achieved [73]. When annealing between 800 and 900 K, potassium is slowly removed from the film (the speed increases strongly when water is present) in the way that a KFeO_2 layer of decreasing thickness remains at the surface while the underlying film converts to $\text{K}_x\text{Fe}_{22}\text{O}_{34}$. The KFeO_2 disappears completely at 970 K and a $\text{K}_x\text{Fe}_{22}\text{O}_{34}$ layer is left. The XPS results [73] suggest that the surface is terminated by a complete Fe-K-O layer while the bulk contains less potassium, corresponding to

about $x \approx 0.67$. This is then the only KFe_xO_y layer with good long-range order. Its LEED pattern and STM image are shown in Fig. (2.4).

2.3.2 AES measurements

AES provides element-specific information on the surface region of the studied model catalyst. Fig. (2.5) shows AES spectra of the three iron oxide films, no contamination signals are seen here. An AES spectrum for Fe_3O_4 after reaction in the micro flow reactor is shown also, where the carbon deposits are clearly seen on the thin film surface. The AES peak intensity ratios of I_K , I_O , I_C with respect to I_{Fe} are used for comparison of surface composition changes of the different model catalysts. As expected, the α - Fe_2O_3 film has a higher oxygen/iron intensity ratio (I_O/I_{Fe}) than the Fe_3O_4 film. Potassium promoted catalysts (potassium signal appears at 256 eV) with different potassium loading are differentiated by the intensity ratio of potassium/iron (I_K/I_{Fe}) and compared to the β -Ferrite- $K_xFe_{22}O_{34}(0001)$ which has a 2×2 LEED pattern and a moderate potassium content of ($I_K/I_{Fe} \sim 2.7$) (Fig. (2.5b)).

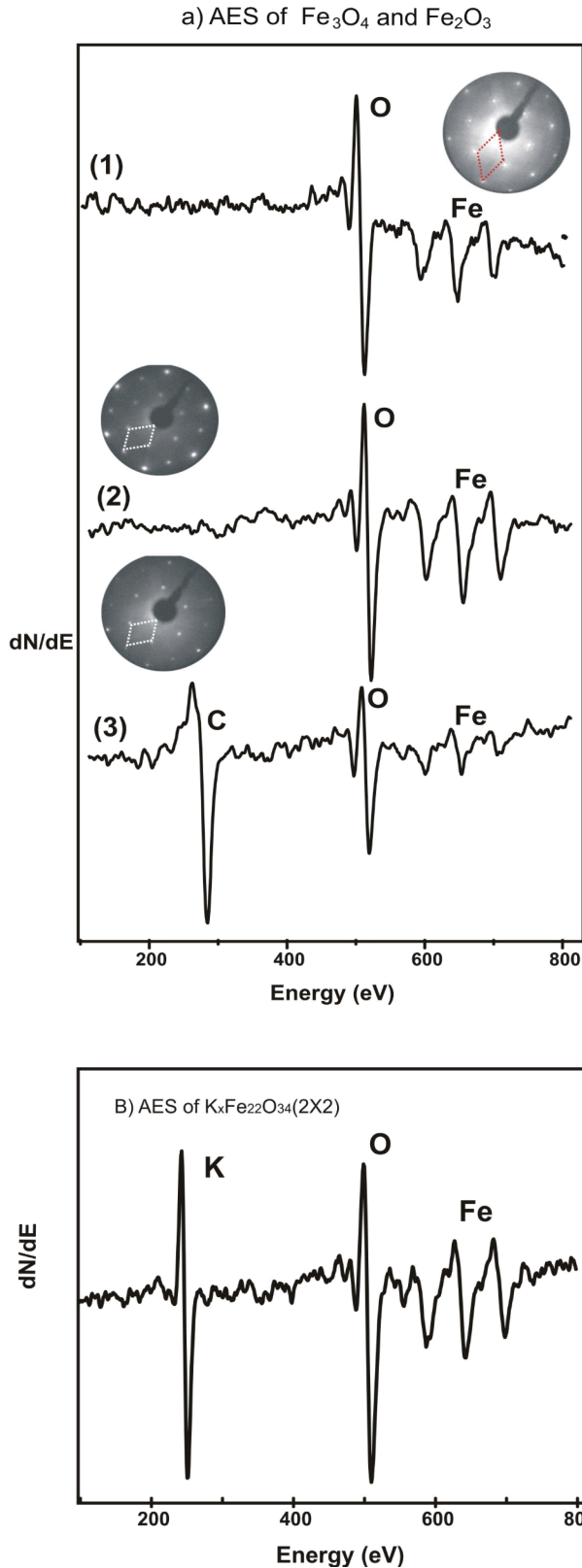


Fig. (2.5).
 a) AES spectra of epitaxial iron oxide films grown onto Pt(111). (1) the $\alpha\text{-Fe}_2\text{O}_3(0001)$, (2) $\text{Fe}_3\text{O}_4(111)$ before reaction (3) $\text{Fe}_3\text{O}_4(111)$ after reaction, b) KFe_xO_y films are at least 100 Å thick.

2.3.3 Adsorption properties (TDS, UPS and NEXAFS)

A great deal of work has been spent on the determination of the surface structure using LEED-(I-V) measurements in combination with dynamic structure analysis

calculations [63,75,76], on the determination of the kind of adsorbed species (molecular or dissociated) after exposure to EB[77], St [78] and H₂O using UPS, on the adsorbate orientation using NEXAFS [79] and on the energetic and kinetic data for adsorption and desorption using TDS and isosteric methods [78]. The collected knowledge for EB and St is summarized in Fig. (2.6a).

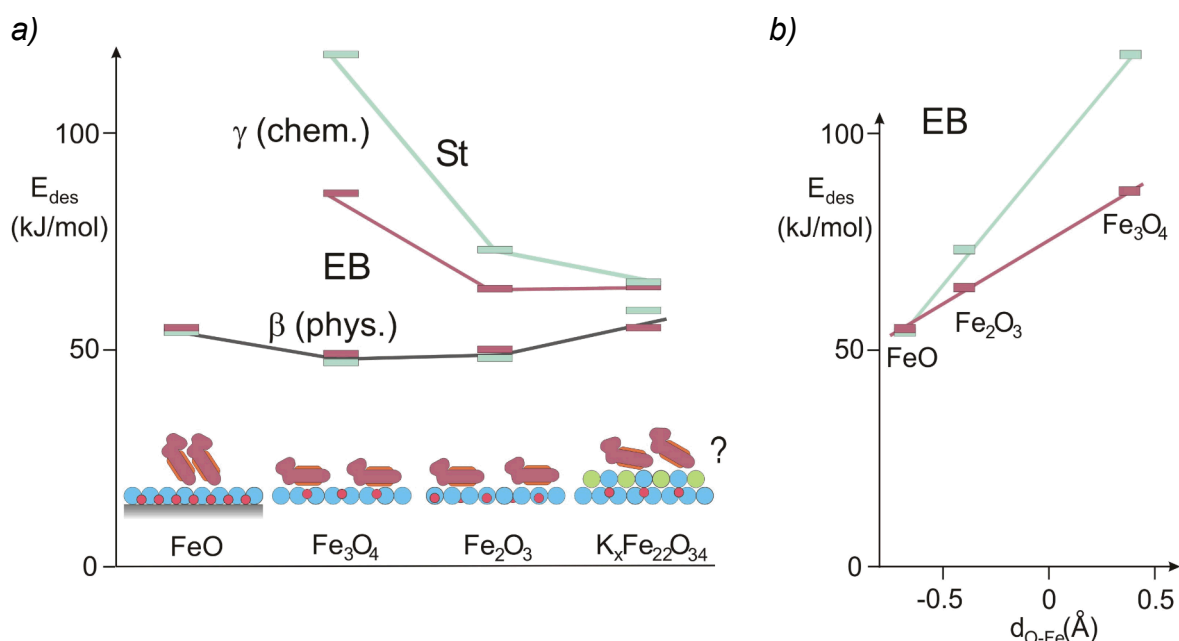


Fig. (2.6). Energetic and structural results for EB (filled symbols) and St (open symbols) adsorption on different substrate films. (a) Desorption energies from TDS [74] for chemisorbed (γ) and physisorbed (β) species and adsorbate arrangement at low coverages of the initially adsorbing species (β on FeO, γ on the others). Shown is adsorbed EB, the arrangement for St is similar. Adsorbate structure for Fe_xO_y from NEXAFS measurements [74]. The arrangement on K_xFe₂₂O₃₄ is hypothetical. (b) Dependence of the desorption energy for the initially adsorbing species on the position of the first iron layer relative to the first oxygen layer.

The FeO film is O-terminated. The first Fe layer is relatively deep below the O-layer (-0.068 nm [83] or 0.062 nm [84]). Also Fe₂O₃ is O-terminated but according to the best-fit structure [59], the first Fe layer is only 0.046 nm below the surface O-layer. In contrast, Fe₃O₄ is Fe-terminated. The Fe atoms are +0.038 nm above the first O-layer. This has a decisive influence on adsorbate structure and interaction. UPS shows all adsorbate states of EB and St at room temperature and below are molecular. NEXAFS shows that for FeO that EB and St adsorb strongly tilted from the beginning. The only

adsorbate state is a weakly bound physisorbed state. Although there is no direct evidence for island formation of the adsorbate, It is likely that the adsorbate-substrate interaction is so weak that adsorbate-adsorbate interaction dominates. As characteristic for condensed aromatics, this interaction probably occurs via the π -orbitals of the benzene ring so that the molecules get tilted. In contrast, both EB and St adsorb almost flat on Fe_3O_4 and Fe_2O_3 , at least for low coverages. Near saturation, tilting increases due to increasing adsorbate-adsorbate interaction. Flat adsorption correlates with the existence of chemisorbed γ -states which saturate before a second, physisorbed layer forms. Chemisorption is much stronger on Fe_3O_4 than on Fe_2O_3 , and it is stronger for St which has a conjugated π -system extending also over the ethyl group, at least if it adsorbs in a planar configuration.

UPS measurements for EB on Fe_3O_4 in adsorption-desorption equilibrium show that saturation of the chemisorbed γ -state corresponds to one EB molecule on two Fe surface sites. This corresponds to only about 83 % of a close-packed adsorption layer assuming a flat adsorbate configuration (Van-der-Waals area of EB $\sim 0.5 \text{ nm}^2$). The physisorbed first β -layer on FeO, however, saturates at a full monolayer which rules out a correlation of the adsorbate with the surface structure [80,81].

These results prove that chemisorption is dominated by the interaction between the strongly polarizable π -system of the adsorbate which represent a soft base [82] and the acidic Fe ions. This is highlighted by Fig. (2.6b) which gives the dependence of E_{des} for the initially adsorbing species (β for FeO, γ for Fe_2O_3 and Fe_3O_4) on the Fe-layer position with respect to the O-layer. On Fe_2O_3 , the Fe-layer is relatively deep below the O-layer but the molecules can obviously still “feel” it and arrange in a flat chemisorbed state. Although the Fe-layer is not much deeper on FeO, the interaction is too weak to compete with the Van-der-Waals interaction between the adsorbates.

For the $K_xFe_{22}O_{34}$ film, a structure analysis does not exist. The quantitative XPS results [73] are compatible with a termination by a Fe-K-O layer as in the bulk of $K_2Fe_{22}O_{34}$. In this case, the first Fe atoms are below the O atoms of the top layer and an interaction with the adsorbate would be weak. On the other hand, interaction may occur with surface K ions, but as long as a structure analysis is missing, any adsorption model is speculative. The existence of a chemisorbed state which proceeds physisorption and has similar binding energies as on Fe_2O_3 suggests that the binding situations on these two surfaces are similar. The difference of the bond strength for EB and St has almost disappeared.

2.3.4 Catalytic activity (Low and medium pressure reactivity measurements)

The first reactivity measurements were performed on unpromoted model catalysts using mass spectrometric analysis in the main UHV chamber by Zscherpel et.al. [85]. A mixture EB:H₂O=1:5 at a total pressure of 3.5×10^{-6} mbar was applied. It turned out that well ordered Fe_2O_3 hematite samples with sharp spots and low background in the LEED pattern were quite inactive while poorly ordered samples with broad spots and high background clearly showed conversion. Typical mass spectrometer traces are presented in Fig. (2.7) [85]. The sample was kept at 873 K, water was admitted at $t=0$, EB about 20 – 30 s later. On a poorly ordered active Fe_2O_3 film, deactivation was observed after several such cycles, going along with indications for reduction to Fe_3O_4 in the LEED pattern. Also carbonaceous deposits were detected by in-situ photoelectron emission microscopy (PEEM). Fe_3O_4 samples were inactive, irrespective of the surface order.

In a first attempt to bridge the pressure gap, medium pressure batch reactor experiments were performed. The high pressure chamber (Fig. (2.8)), at that time without reactor) was used as batch reactor cell. For mass spectrometric analysis, a bypass line with a dosing valve was mounted between the high pressure chamber and the UHV analysis chamber. The gas mixture (EB:H₂O=1:10, total pressure 0.6 mbar) was admitted and after about 10 min, sample heating was started. After a few minutes, the reaction temperature was reached. Fig. 8 shows that styrene and hydrogen evolution goes along with ethylbenzene consumption. Again, activity increases with the degree of disorder of the starting Fe₂O₃ film. The most active film was deactivated after about 30 min. PEEM showed coke deposits. In AES, carbon was visible and after its removal by a mild oxidation cycle, LEED showed a mixture of the patterns of Fe₂O₃ and Fe₃O₄, confirming catalyst reduction during the experiment. Corresponding experiments using Fe₃O₄ model catalysts again showed no measurable activity.

These experiments showed that meaningful conversion measurements can be performed over single crystal samples with a surface area of as little as 0.5 cm². They confirmed that Fe₂O₃ is clearly more active than Fe₃O₄. Deactivation of Fe₂O₃ goes along with reduction and coking and defects are necessary for high conversion.

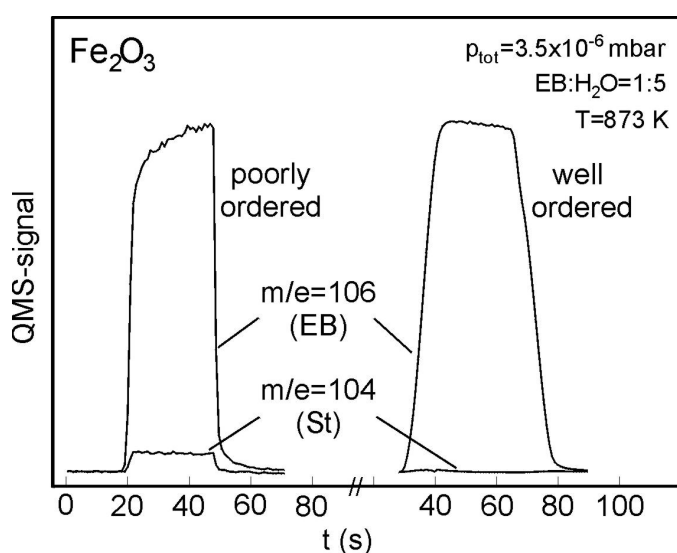


Fig. (2.7).

Mass spectrometer traces for EB and St under low pressure reaction conditions as indicated over poorly ordered and well ordered Fe₂O₃ samples. Water was admitted at t=0. The traces reflect the periods of EB admission.

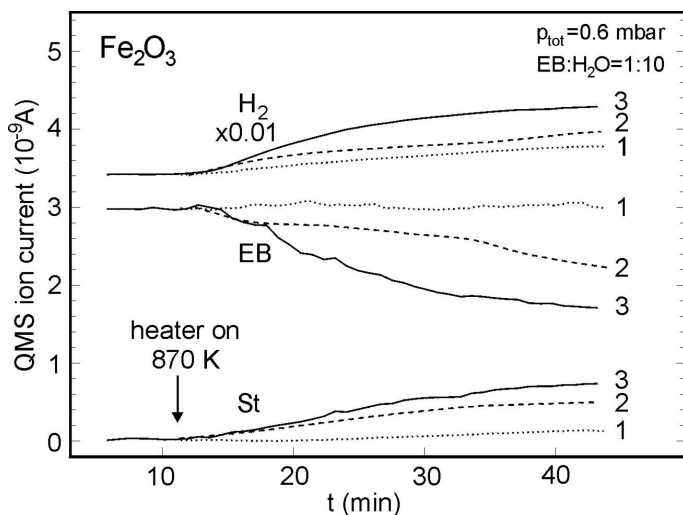


Fig. (2.8).

Mass spectrometric analysis of a batch reactor experiment at intermediate pressure conditions as indicated for three Fe_2O_3 model catalysts with differing surface quality. (1) well ordered, (2) intermediate order, (3) poorly ordered.

2.3 Aims and work strategy

Here, we apply the model catalysis approach to the investigation of the catalytic dehydrogenation of ethylbenzene (EB) to styrene (St) one of the 10 most important catalysed organic reactions, which industrially is performed over potassium-promoted iron oxide catalysts. The reaction is endothermic ($\Delta H = 125 \text{ kJ/mol}$) and is run at high temperature, typically 870 K and at 1 bar in the presence of excess overheated steam.

The aim of this work is based on studying the catalytic activity near to real catalysis conditions over the iron oxide model catalysts, which is the continuation of the work which has been done in our group, through which the growth and characterization of the unpromoted iron oxide phases (FeO , Fe_3O_4 and Fe_2O_3) and the potassium promoted iron oxides (KFe_xO_y) were studied extensively and the different phases were well identified. The adsorption properties and catalytic activity at low and medium pressures were also studied.

The basic idea as we apply it here is to prepare well defined model catalyst samples and to characterize their surface structure and composition under UHV condition

using mainly LEED and AES. Then the samples are transferred under vacuum into a reactor which allows to determine the catalytic properties (conversion, selectivity, deactivation behaviour) in-situ under realistic temperature and pressure conditions using a single crystal micro flow reactor. After that, the samples are transferred back into the main UHV chamber for post-reaction analysis.

Our aim is with the help of surface science techniques to

- Identify the phase and structure changes of the catalyst under the course of reaction. The effect and role of steam in the reaction.
- Understand of the main reasons for the deactivation process and how to prevent them.
- Understand the role of iron oxide, promoting effect of potassium and the effect of potassium loading on the activity and deactivation of the catalyst.

The micro flow reactor is designed in a stagnation point form, which allows also the simulation of the reactor and the reaction. This will be done in cooperation with A. Schüle and G. Kolios from the University of Stuttgart.

In addition, the reaction behaviour is studied over pressed powder samples in the micro flow reactor, under the same conditions like the model catalyst. Through comparing the results, information about the diffusion and transport diffusion limitations can be gained. In this way the pressure and material gaps are bridged.

Chapter-3

Experimental

3.1 Instrumentation setup

3.1.1 UHV analysis system

2 ultra high vacuum (UHV) chambers; TDS (1) and PEEM (2), were used in this study. They are connected by a gate valve and the sample could be transferred between them with the help of a magnetic transfer rod. Fig. (3.1) shows a schematic of mainly the TDS (1) and the load lock (reactor) (3) chambers, which were mainly used in this study. The base pressure was below 10^{-10} mbar. The TDS chamber was equipped with a gas inlet manifold, evaporators for iron and potassium, a sputter gun and fully rotatable manipulators with identical sample heating and cooling stations.

The TDS chamber is used for TDS experiments. A Balzers quadruple mass spectrometer (QMS) is mounted horizontally and the sample could be placed in 1 mm in front of a stainless steel tube with a 5 mm diameter, smaller than the sample diameter of 10 mm. This QMS was also used for the thermal programmed oxidation (TPO) experiments.

The TDS chamber (1) contains also a back-view LEED optics and a cylindrical mirror analyzer (CMA) for Auger electron spectroscopy (AES) measurements, an Ar^+ -sputter gun, and an ion gauge. The LEED and AES are used for pre- and post-reaction characterization of the model catalyst structure and chemical surface composition. The PEEM chamber (2) is equipped with an ion scattering spectroscopy (ISS) spectrometer and a photoelectron emission microscope (PEEM).

The load lock chamber (3) was used for high pressure oxidation and treatments. The single crystal flow reactor is located in the load lock chamber (3), was build by Khurs et. al. [62], who has run the first experiments using this system.

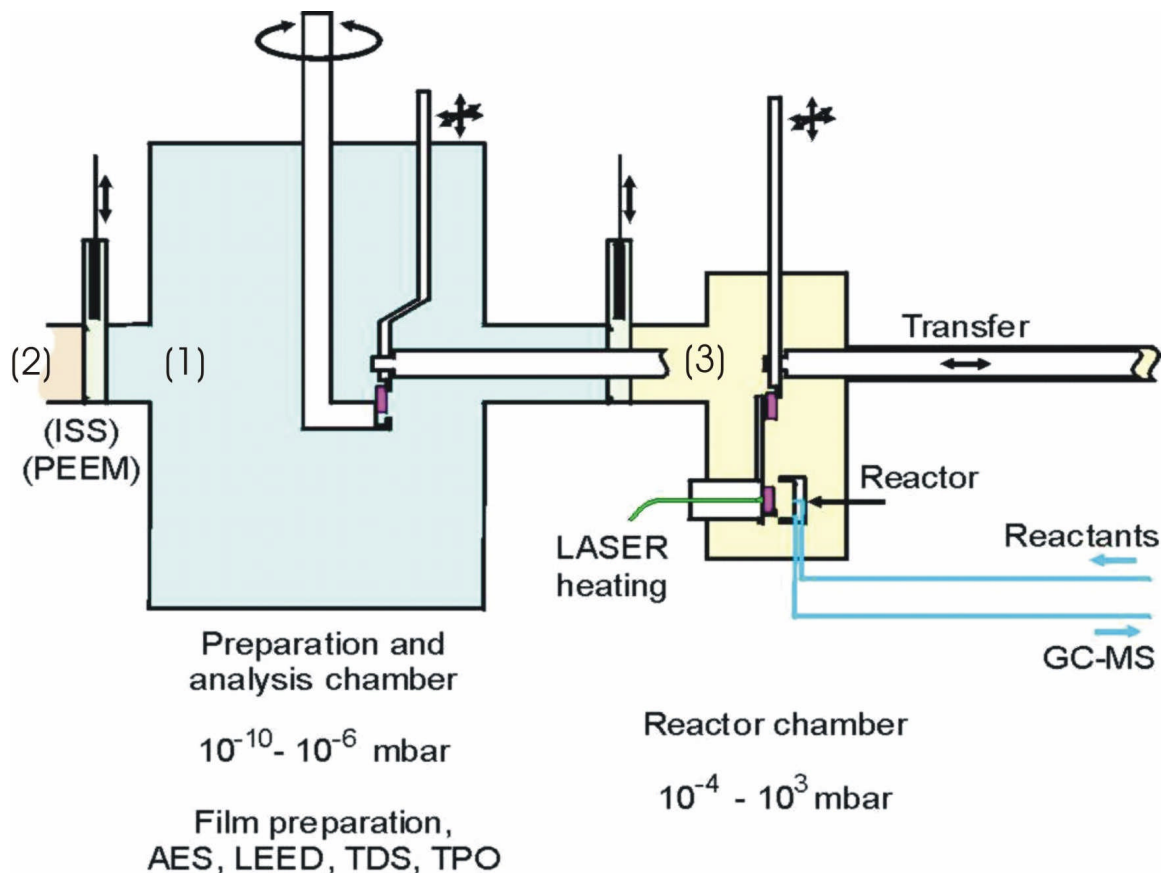


Fig. (3.1). Experimental setup, schematic, consisting of the preparation and analysis chamber (TDS) (1), PEEM (2) working at ultrahigh vacuum and the reactor chamber(3), working at pressures up to 1 bar. The sample on its support (Fig.(3.2)) is moved by a magnetically coupled transfer rod. The transfer between the rod and the manipulator or the reactor is accomplished by wobble sticks.

3.1.2 Sample transfer and heating

Fig. (3.2b) shows a front view photograph of the manipulator head with the sample heating-cooling station and the sample on its support, pushed half-way into the sample quiver [18]. Fig. (3.2a) is a schematic side view in the transfer position with the transfer rod and wobble stick. The magnetic rod is connected to the manipulator by the indicated centering bores which provide mechanical stability during transfer. Using the wobble stick, the sample support can be pulled to the transfer rod, where it is held by spring clamps, or it can be pushed from the transfer rod into the sample quiver on the manipulator. Afterwards, the wobble stick and the transfer rod are

retracted. Due to the mechanical connection between manipulator and transfer rod the transfer is safe and a sample loss is not possible.

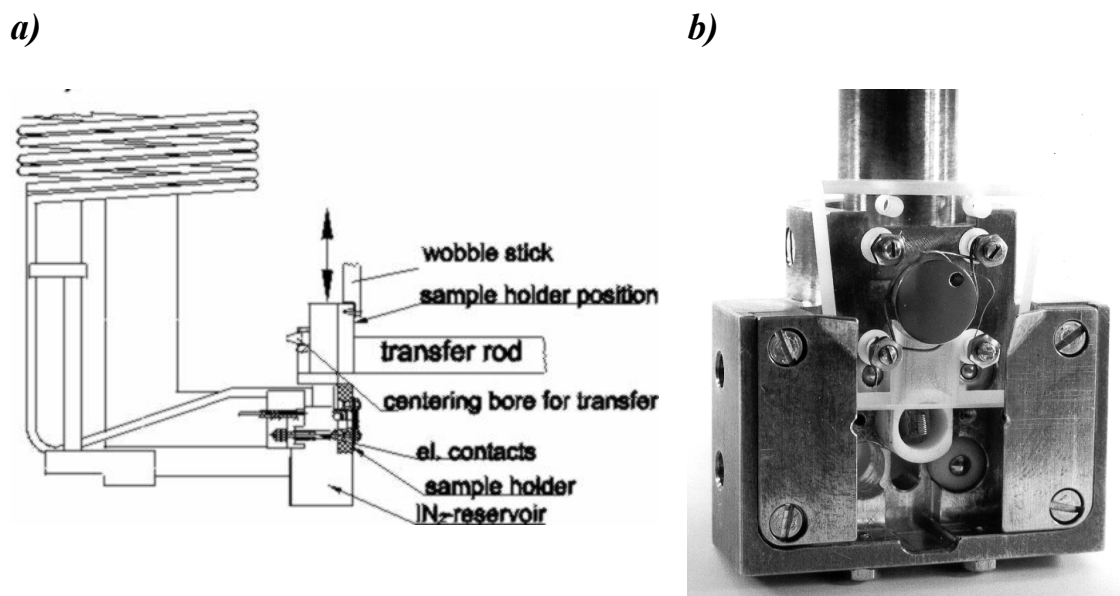


Fig. (3.2): a) Schematic side view of the magnetic transfer rod, the wobble stick, and the heating-cooling station in the transfer position. b) Front view photograph of the sample heating-cooling station on the manipulator.

The sample support is fabricated from a sapphire single crystal. Sapphire was chosen because it has a high thermal conductivity below room temperature allowing fast liquid nitrogen cooling, whereas its thermal conductivity is low at elevated temperatures thus lifting the thermal contact during annealing. Sapphire is mechanically stable and generates no trouble during sample transfer. It is chemically inert, which makes it suitable for prolonged oxidation treatments at elevated pressures and catalytic experiments in reactive atmospheres. Heating from 100 to 1300 K with 5 K/s does not damage the sapphire sample support if it was annealed at 2100 K before. In the front view photograph (Fig. (3.2b)) of the sample heating-cooling station the sample holder with a mounted platinum sample can be seen. Behind the sample, the

sapphire support has a 8 mm diameter hole, so that electron beam heating from behind is possible when the sample holder is placed into its final position on the manipulator. The filament of the electron beam heater is placed within a ceramic tube and can be seen in Fig. (3.2b). Sample temperatures up to 1500 K are reached with this heater. Four holes around the sample are used for screws that provide electrical contact with spring bolts on the manipulator station. Two screws provide electrical contact to a thermocouple spot-welded to the side of the sample. Two screws are used to fix the sample either by Pt clamps or by tungsten wires. The manipulator head contains a liquid nitrogen reservoir made from copper for sample cooling down to 100 K.

3.1.3 High pressure reaction cell

The high pressure cell (a side-view schematic with the reactor inside is shown in Fig. (3.3) consist of a 63 mm diameter double cross which is separated from the main chambers by a 63 mm gate valve. The sample is transferred in the same way from the magnetic rods into the sample stations of the high pressure cell as described in the previous section. The sample station is similar to that on the manipulator but since electron beam heating is not possible at high pressures oxidation and reactivity measurements conditions, a laser heating system with 100 W power (explained in more detail in Fig. 3.4) is used for oxidation treatments in oxygen pressures up to 1000 mbar [19].

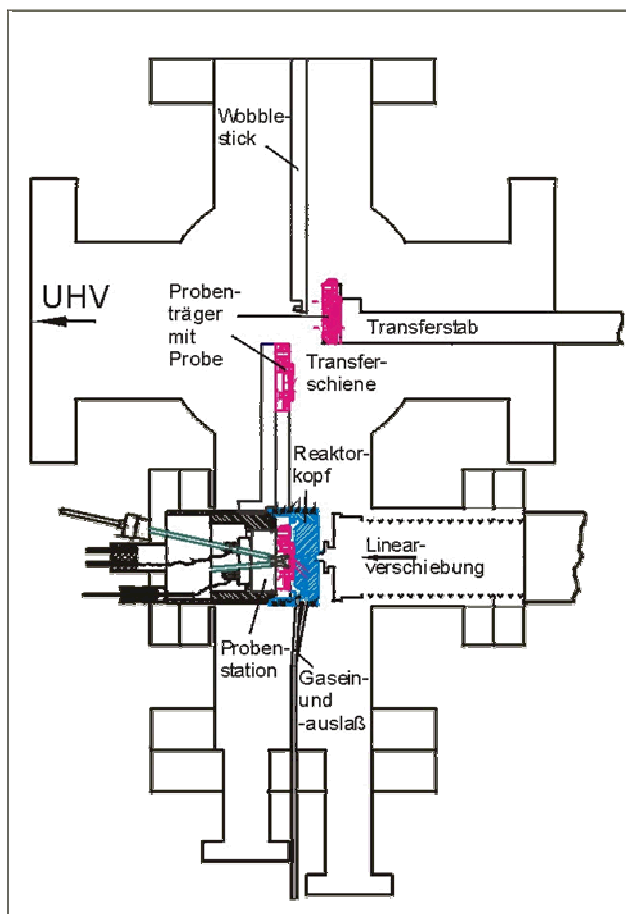


Fig. (3.3). A side view of the high pressure reaction cell with the flow reactor located inside. The sample is transferred from UHV chamber using magnetic transfer line. With the help of wobblestick the sample is transferred and placed inside the reactor down in the chamber.

3.1.4 The reactor

Fig. (3.3), displays a side view of the high pressure reaction cell with the flow reactor located inside. The reaction cell can be pumped down to 10^{-8} mbar to allow sample transfer from the UHV analysis chamber. From above, a wobble stick allows transferring the sample support from the magnetic transfer rod into the reactor below. For this purpose, the reactor cup has to be opened. It can be closed with a linear motion drive.

The high pressure reaction cell is separated from the UHV chamber by a 64 mm gate valve. After transfer, the reaction cell can be vented with nitrogen or helium.

Fig. (3.4) shows the reactor in more detail. The linear motion drive coming from the right (not shown here) ensures a tight connection of the reactor and the reactor cup

with a gold gasket between them. The space between reactor cup and sample support is the reaction volume of the reactor (approximately 4 ml). Since the continuous gas flow prevents back streaming, the effective reactor volume is only that between the sample and cap. The sample itself is only ~1 mm away from the reactor cap with the gas inlet. The gas flow enters this volume through a capillary of 0.2 mm in diameter and spreads onto the center of the sample surface. Gas outlet goes to the sides of the reactor cup. The reactor cap and the gas lines in the reaction cell can be heated resistively to prevent condensation of educts and product molecules. On the left, the feedthroughs for the laser fibers are visible. The outer parts are made of stainless steel. The design of the sample holder was described in detail in 3.1.2 [19].

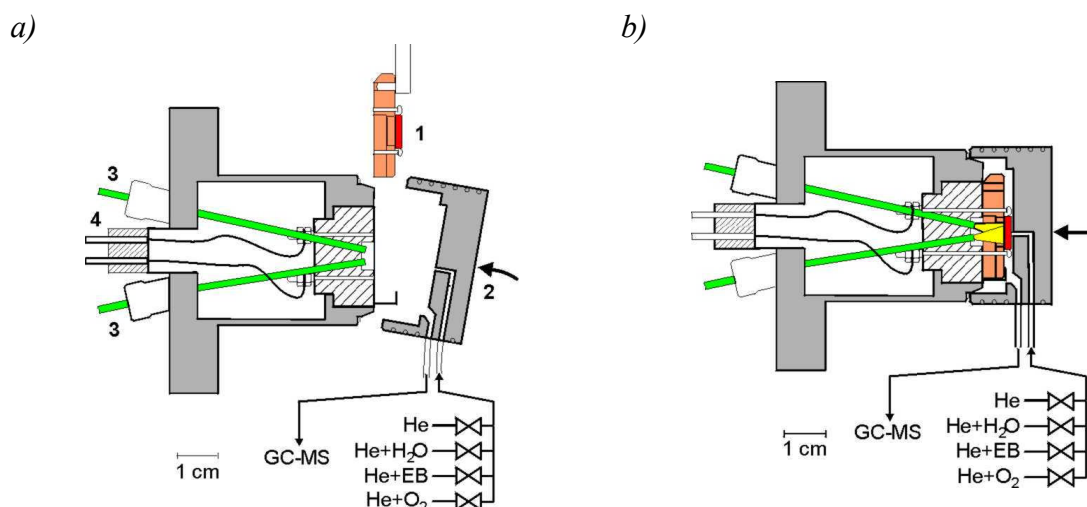


Figure (3.4). Stagnation point micro-flow reactor for model catalysis at high pressure. 1: sample on sapphire support; 2: reactor cap; 3: fiber rods for coupling in laser irradiation; 4: thermocouple feedthroughs. (a) during insertion of the sample on a wobble stick, reactor cap withdrawn. (b) reactor cap closed, gas admission and analysis lines schematically shown.

3.1.5 The laser heating system

Heating of the sample is performed by two high power fiber-coupled diode lasers (JENOPTIK Laser diode GmbH) with a total optical output power of 100 W. In this

way, the spot size (4 mm in diameter) is well defined on the back of the sample which guarantees that the sample is the warmest place in the reactor.

The lasers have a wavelength of 809 nm, the operating current for 50 W each is 40 A. A working temperature of 25 °C is achieved by water cooling. An external power supply is used (Delta Electronics). We use fibers of 1000 μm in diameter that are polished at the ends. Using a home made analog PID-controller, defined temperature ramps and hold temperatures are possible.

3.1.6 The gas supply system

Fig. (3.5) shows the gas supply system for the investigation of the St synthesis reaction carried out over iron oxide based catalysts in the presence of steam. All tubes are 1/16 inch in diameter. Helium (5.0) is used as carrier gas. The helium passes a 0.5 μm filter located directly in front of mass flow controllers (Bronkhorst). In order to get a molar ratio of the reaction educts water and ethylbenzene (EB) of 10:1, a flow of 5 ml/min helium passes through liquid ethylbenzene and a flow of 20 ml/min helium through liquid water both held constant at 30 °C. In order to achieve equilibrium, two reservoirs are passed sequentially. Small drops are separated by the empty reservoirs. The additional helium gas line (40 ml/min) as well as the outlet valves allow fast switching between educts gases without changing the total gas flow. In this case, it is possible to switch off the water and instead introduce 20 ml/min of helium together with the ethylbenzene instead to study the role of the water in this reaction.

The educts then pass a 0.5 μm filter before entering the reactor. A reactor bypass allows detection of the educts before reaction. All valves and filters are Swagelok products. All tubes, valves and filters located behind the ethylbenzene and water reservoirs are heated to prevent condensation.

Analysis is done by a GC/MS system. We use a Varian 3400 gas chromatograph with a VA 5 MS 30 m column (I.D. 0.25 mm, film 0.25 μ m (5% Phenyl)-methylpolysiloxane) and a 250 μ l sample loop. A Finnigan ITD 800 ion trap is connected to this gas chromatograph.

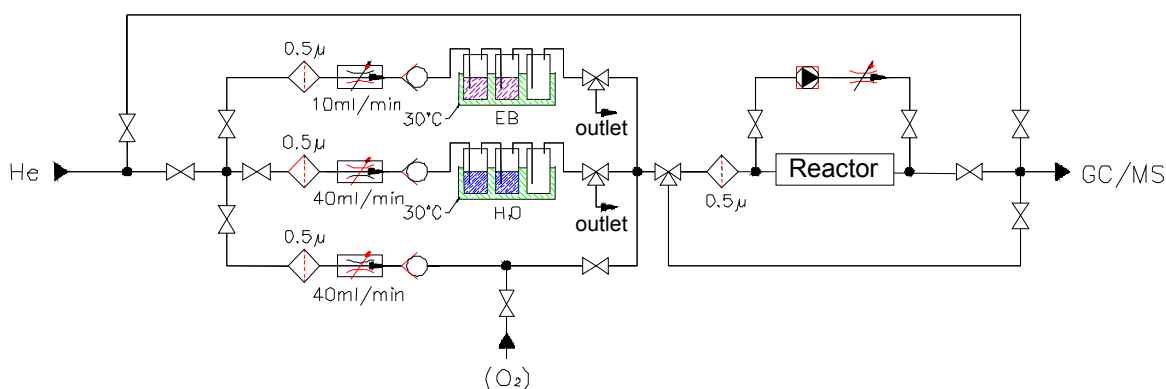


Fig. (3.5). The gas supply system used for the investigation of the styrene synthesis reaction carried out over iron oxide based catalysts in the presence of steam. All tubes are 1/16 inch in diameter. Helium (5.0) is used as carrier gas. The helium passes a 0.5 μ m filter located directly in front of mass flow controllers (Bronkhorst).

3.2 Spectroscopic and microscopic characterization methods

3.2.1 LEED, TPO and AES

The LEED measurements were performed using OMICRON optics at $T=320$ K. The diffraction patterns were recorded with a CCD camera from the LEED screen and stored via computer. AES measurements were done using an OMICRON spectrometer with a CMA as detector. The range was chosen from 100-800 eV where the characteristic peaks of K, C, O and Fe appear, the intensity of the peak ratios of O, C, K with respect to the Fe peak (i.e. I_C/I_{Fe} , ..etc.), were used for comparing the thin films compositions before and after reaction. For TPO experiments the heating rate was always 5 K/s, the maximum temperature 1000 K and the O_2 pressure 1×10^{-7}

⁶mbar. This has the advantage of partial removal of coke, partial reordering of the surface and no reoxidation of the substrate [79].

3.3 Preparation of epitaxial iron oxide films

Single crystalline iron oxide films were grown epitaxially on Pt(111) substrates. The Pt(111) surface was cleaned by cycles of argon ion bombardment (1 keV), annealing to 1300 K and by oxidation-annealing cycles until it exhibited a sharp LEED pattern and show no contamination signals in AES. The iron oxide films were prepared by iron deposition at room temperature and subsequent oxidation for at least 5 min at temperatures between 870 and 1000 K in 10^{-6} mbar oxygen partial pressure as shown in Fig. (3.6). In this way 1-2 monolayer thick FeO(111) films and 100 200 Å Fe₃O₄(111) multilayer films can be prepared. α -Fe₂O₃(0001) films were obtained by oxidizing Fe₃O₄ films in oxygen pressures between 10^{-4} and 1 mbar in the separate high pressure cell. After this oxidation, the samples were cooled down to room temperature in the high pressure oxygen atmosphere, then the oxygen was pumped off and the sample was transferred back into the analysis chamber [59].

Promoted iron oxide thin films (KFe_xO_y) are prepared by deposition of potassium from a getter source (SAES) on the Fe₃O₄ (111) or Fe₂O₃(0001) iron oxide thin films at room temperature and subsequent annealing up to 950 K in vacuum or in 1×10^{-6} mbar oxygen . In some preparations we used repeated deposition-annealing or (deposition-oxidation) cycles in order to get a high potassium coverage. Potassium coverage was monitored by AES. The LEED pattern of the promoted catalyst depends on the amount of potassium content as has been investigated [59,88].

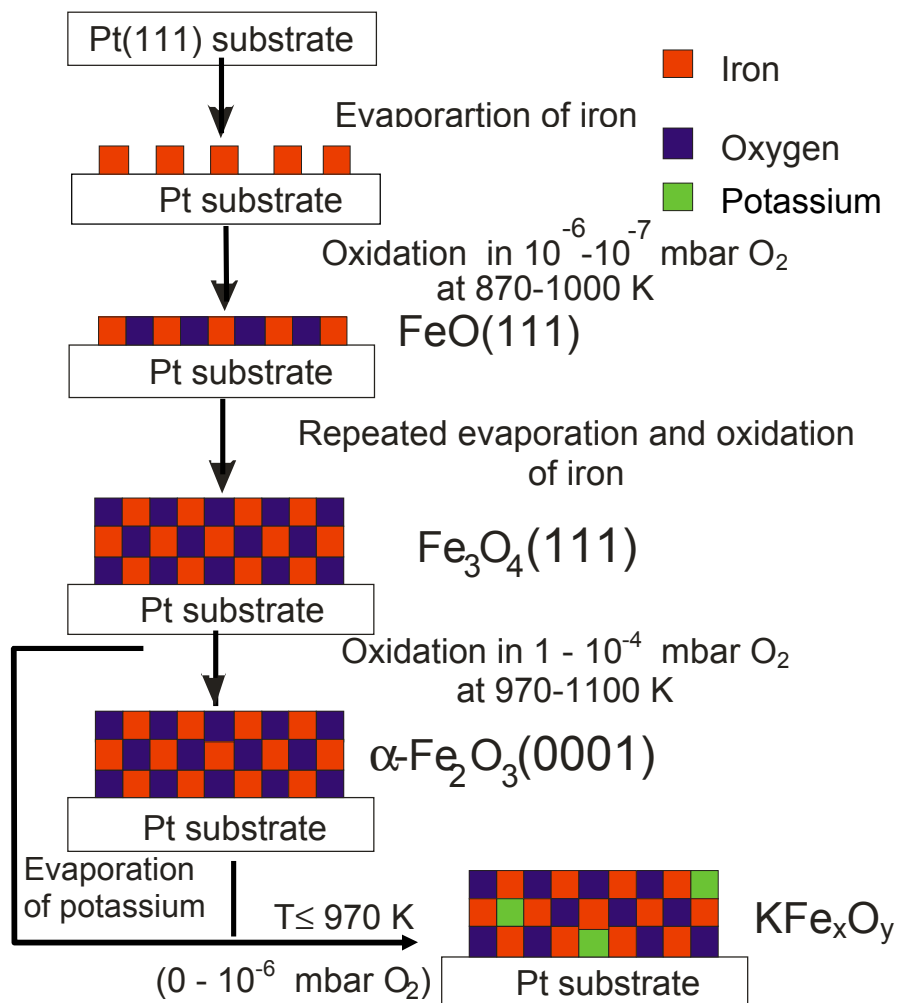


Fig. (3.6). Schematic representation of the preparation of epitaxial iron oxide films Fe_xO_y and KFe_xO_y on Pt(111), accomplished by repeated cycles of iron deposition and subsequent oxidation.

3.4 Pressed Unpromoted Fe₂O₃ powder samples.

3.4.1 Preparation of the pressed pellets

Polycrystalline catalyst samples with the same outer dimensions as the Pt(111) substrates for the model catalysts, were prepared from ordinary hematite powder, purity > 99% and the alkali metal content below the detection limit. The main idea was to obtain catalyst samples with sufficient mechanical stability and a well ordered geometry while maintaining the high purity of the material. Dry pressed powder pellets were prepared by drying them for 24 hours at ambient conditions, followed by a three step calcination procedure (3 hours at 100°C, then 2 hours at 300°C, and finally 2 hours at either 600, 700 or 800°C). The samples were prepared by A. Schüle from the ICVT institute in technical university of Stuttgart [84].

The pellet weight was about 100 mg. Sample clamps from pure platinum sheets with 0.2 mm in thickness were designed for holding and heating these pressed powder samples on the sapphire sample support. A thermocouple was spot-welded on the platinum sample clamps for temperature measurements. A picture of the sample (1) and the sample clamps (2) on the sapphire support is seen in the Fig.(3.7a and b).

The homogeneity of heating these pellets with this designed sample clamps was tested using the reactor head and the laser as a source for heating at air for visual inspection. The sample was heated with the laser from the back and the temperature of the sample was also measured using an external thermometer, the temperatures measured were compared and did not show a considerable difference. Fig(3.7c) shows the sample heated up to 890 K (the temperature distribution was homogenous from the visual inspection as seen in the picture).

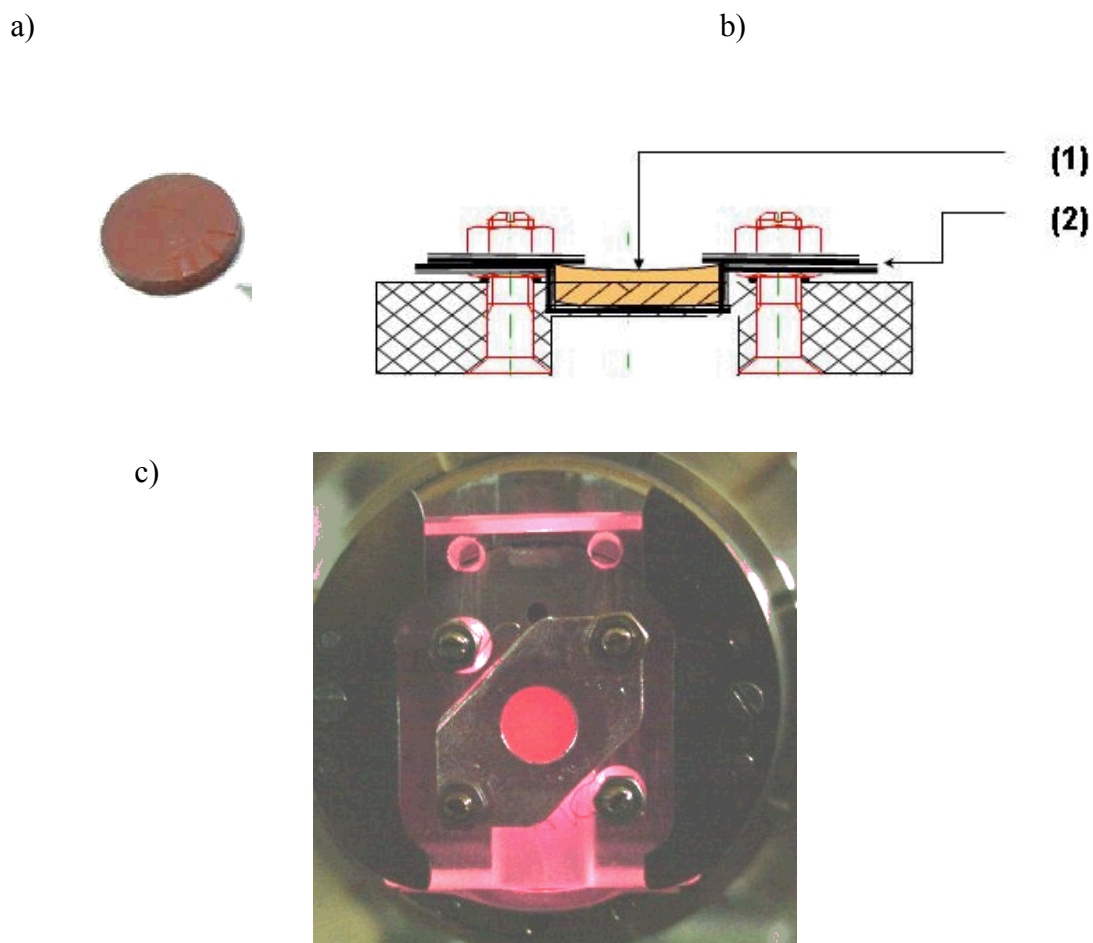


Fig. (3.7). a) The pressed (Fe_2O_3) powder samples in form of pellets. b) A side view of the pressed pellet (1) mounted on a sapphire sample support with the help of Pt clamps (2) designed for this purpose, the thermocouple is mounted on the Pt clamps. c) A heating homogeneity test in air at 890K, for the sample using the laser source.

3.4.2 Characterization of the powder samples (BET, XRD and SEM-EDX)

Since hematite (Fe_2O_3) is known as an insulator, characterization of the pressed sample with surface science techniques like AES was not possible due to charging. Ex-situ characterization methods like X-ray diffraction (XRD) for characterization of the phase of the iron oxide before and after reaction and Scanning electron microscopy (SEM) and Energy-Dispersive X-ray analysis (EDX) were used for determining the overall morphology, microstructure, composition and particle size of the fresh sample and used ones after reaction. A simple test we have used for testing

the reduction of the Fe_2O_3 to Fe_3O_4 is by using a permanent magnet to differentiate between the Fe_3O_4 which is magnetic and Fe_2O_3 which is not.

The surface area of the pressed powder samples ($2.8 \text{ m}^2/\text{g}$) was measured using a single point BET measurements, Nitrogen was used as the adsorbent gas.

3.4.3 Cleaning of the pressed powder samples.

The pressed powder samples were cleaned in the high pressure cell by heating them up to 1000 K in 1 mbar oxygen pressure for 30 minutes which corresponds to the oxidation treatment of the unpromoted model catalyst. The fresh samples without cleaning, show a very low activity ($< 1\%$ conversion) when used in the micro-flow reactor. During the reaction experiments the samples were heated in the presence of only water and oxygen in the feed for a bout 20 minutes before the EB was admitted and the experiment continued. The effect of sample cleaning on the particle size and shape was studied by characterizing the sample after the cleaning procedure with SEM and EDX.

3.4 Reaction experiments

A flow reactor designed for investigating the heterogeneous catalytic reactions on the model catalysts was used which was described in detail (in section 3.1.4). The space between the reactor cup and the sample holder is the dead volume. The gas flows and enters this volume through a capillary and spreads onto the center of the sample surface. Gas outlet goes to the sides of the reactor cup. A laser source was used for heating the sample from the back, up to reaction temperature. This heating period takes a bout 25 min is crucial, it was optimized to make sure that that changes to the catalyst during this period are minimized.

All the reactions were done under the same standard reaction conditions of a (25 ml/min) total flow rate, atmospheric pressure and 870 K reaction temperature. The feed composition (EB: water : oxygen molar ratios shown in Table 3.1) were varied for performing different reaction experiments. In case of reactions on the Fe₃O₄ no oxygen was introduced in the feed during the heating period, in case of reactions without water 20 ml/min of He alone were introduced to keep the same total flow. In case of promoted catalysts the sample was heated up to the reaction temperature in presence of 20ml/min He alone and then the mixture of EB and H₂O in He was introduced.

Table 3.1. Partial pressures and molar ratios of reactive gases in the gas feed for the used standard reaction conditions. The rest to the working pressure of 1 bar is He. The standard reaction temperature is 870 K, the standard total flow 25 ml min⁻¹.

Reaction conditions	p (mbar)	Molar ratios
Normal	p(EB)=3.3 p(H ₂ O)=33	EB : H ₂ O 1 : 10
Reductive	p(EB)=3.3	--
Oxidative	p(EB)=3.3 p(H ₂ O)=33 p(O ₂)=1.7	EB : H ₂ O : O ₂ 1 : 10 : 0.5

The standard reaction experiment consists of the following steps:

1. Sample preparation in UHV, pre-reaction characterization by LEED and AES
2. Sample transfer under vacuum into the reactor
3. Preheating the reactor cap to 400 K and out-gassing in vacuum
4. Backfilling the reactor chamber with N₂ (p=1 bar)
5. Sample heating during flow of He, if wanted with admixture of H₂O and/or O₂,
6. After reaching the T_{reac}: H₂O and/or O₂ are stopped (if wanted), EB is admitted, GC-MS is started,

7. Reactivity measurement,
8. Stop of EB, H₂O, O₂,
9. Cooling in He to T<500 K,
10. Evacuation and back-transfer to UHV,
11. Post-reaction characterization by AES, LEED; if necessary removal of coke by TPO

cycle(s), followed by AES and LEED [82,83].

The primarily measured quantities are GC peak areas. Under typical reaction conditions, the sum of the peak areas of all aromatics (EB, St and traces of toluene, benzene) is ~95% of the EB peak area without reaction (e.g. at low temperature). The missing ~5% go thus into products which we cannot detect like C_xH_y, CO, CO₂, H₂. The highest observed conversions were ~10% so that the EB peak area corresponds in all cases to more than about 85% of the admitted EB. In view of the uncertainties of the EB-flux and the sample area which enter the determination of an absolute rate, we neglect the missing 15% and refer the conversion yield *y* in % to the main EB peak area as measured. The conversion rates presented below are then calculated from the yield according to

$$r \text{ (cm}^{-2} \text{ s}^{-1}\text{)} = [F \times y(\%) \times 10^2] / A = 6.54 \times 10^{14} y(\%),$$

with the EB-flux $F = 3.27 \times 10^{16}$ molecules s⁻¹ and the model catalyst area $A = 0.5$ cm².

Rates are always given in St molecules cm⁻² s⁻¹.

Chapter-4

Results

4. Results

4.1 Blank experiments

The blank activity of the micro-flow reactor was checked in two different experiments. The first experiment was done to test if there is any reaction on the reactor cap, since during reaction experiments the reactor cap temperature reaches ~ 670 K and also since the surface area of the reactor cap is much larger than the surface area of the single crystal sample. The reactor cap was heated up to ~ 730 K the reactants were admitted to the reactor and the activity was followed for more than 1 hour. No styrene conversion or other byproducts were detected.

A second blank experiment was done by measuring the styrene conversion rate on a sample incidentally contaminated by SiO_2 . The conversion rate was below $\sim 0.1 \times 10^{15}$ molecules $\text{cm}^{-2} \text{s}^{-1}$, which is the detection limit of our GC. This represents the upper limit of the blind activity of the micro-flow reactor.

4.2 Unpromoted model catalysts

4.2.1 Dehydrogenation reaction on $\alpha\text{-Fe}_2\text{O}_3$ (0001) and Fe_3O_4 (111) model catalysts in presence of steam (normal conditions).

As Fig. (4.1) shows the reaction on the clean unpromoted $\alpha\text{-Fe}_2\text{O}_3$ (0001) model catalyst starts with a high St conversion rate of $\sim 4 \times 10^{15}$ molecules $\text{s}^{-1}\text{cm}^{-2}$. This rate decreases with time on stream until it reaches a steady state after ~ 70 min with a rate of $\sim 0.5 \times 10^{15}$ molecules $\text{s}^{-1}\text{cm}^{-2}$. Post reaction characterization with AES showed that there is a significant amount of graphitic carbon deposits on the catalyst surface ($\mathbf{I}_C/\mathbf{I}_{Fe} \sim 3.4$). After removal by performing 3 TPO cycles, LEED showed that the surface exhibits the LEED pattern of Fe_3O_4 (C in table (4.1)).

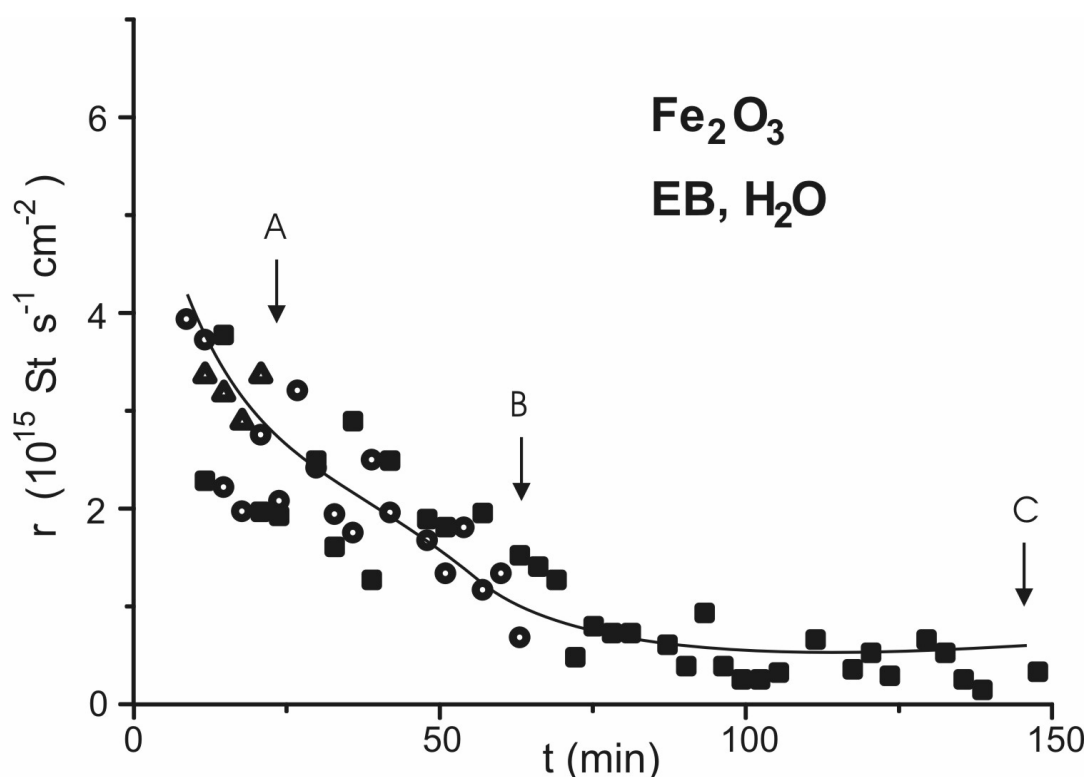
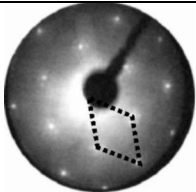
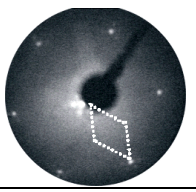
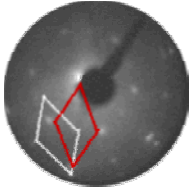
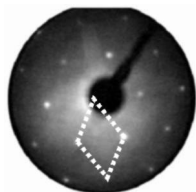


Fig. (4.1). Time dependence of the St conversion rate at 870 K, normal conditions, EB and H₂O in the feed, over α -Fe₂O₃ (0001). The labels A-C give the positions where sample characterization was performed (see table (4.1)).

A detailed investigation of this deactivation behavior on the catalyst was done by repeating and interrupting the reaction on freshly prepared samples after different times from starting the reaction Fig. (4.1). The results showed that in the high yield rate region at point **A** there is a small amount of carbon deposited, $I_C/I_{Fe} \sim 1$, and there is a small decrease in the I_O/I_{Fe} ratio. After 1 TPO cycle, LEED showed the film still consists of Fe₂O₃ and the LEED spots are more diffused indicating increased roughness. At point **B**, AES showed an increase in the amount of carbon deposits on the surface and the Fe₂O₃ is partially reduced to Fe₃O₄ as concluded from the superposition of the LEED patterns of both phases (table (4.1)).

Table 4.1. LEED patterns and intensity ratios of the main Auger peaks of carbon, oxygen and iron before and after reaction for the unpromoted Fe_2O_3 model catalysts.

Treatment	LEED pattern	Phase from LEED	Auger intensity ratios		Label in Fig. 4.1
			I_C/I_{Fe}	I_O/I_{Fe}	
Fe_2O_3 before reaction		Fe_2O_3	0	3.5	-
After reaction with EB + H_2O		after 1 TPO cycle: Fe_2O_3	1.1	3.2	A
		after 3 TPO cycles: Fe_2O_3 and Fe_3O_4	3.6	4.0	B
		after 3 TPO cycle: Fe_3O_4	3.4	3.8	C

After reaction, one Fe_2O_3 sample was also transferred ex-situ for characterization with STM. Comparing STM images in Fig. (4.2) of the catalyst surface before and after reaction confirms that there is an increase in the surface roughness after reaction. The surface is covered by carbon deposits as AES has showed, but it was not possible from STM measurements to see if the surface is completely covered by a closed layer of carbon deposits or if these carbon deposits are in form of islands on the surface.

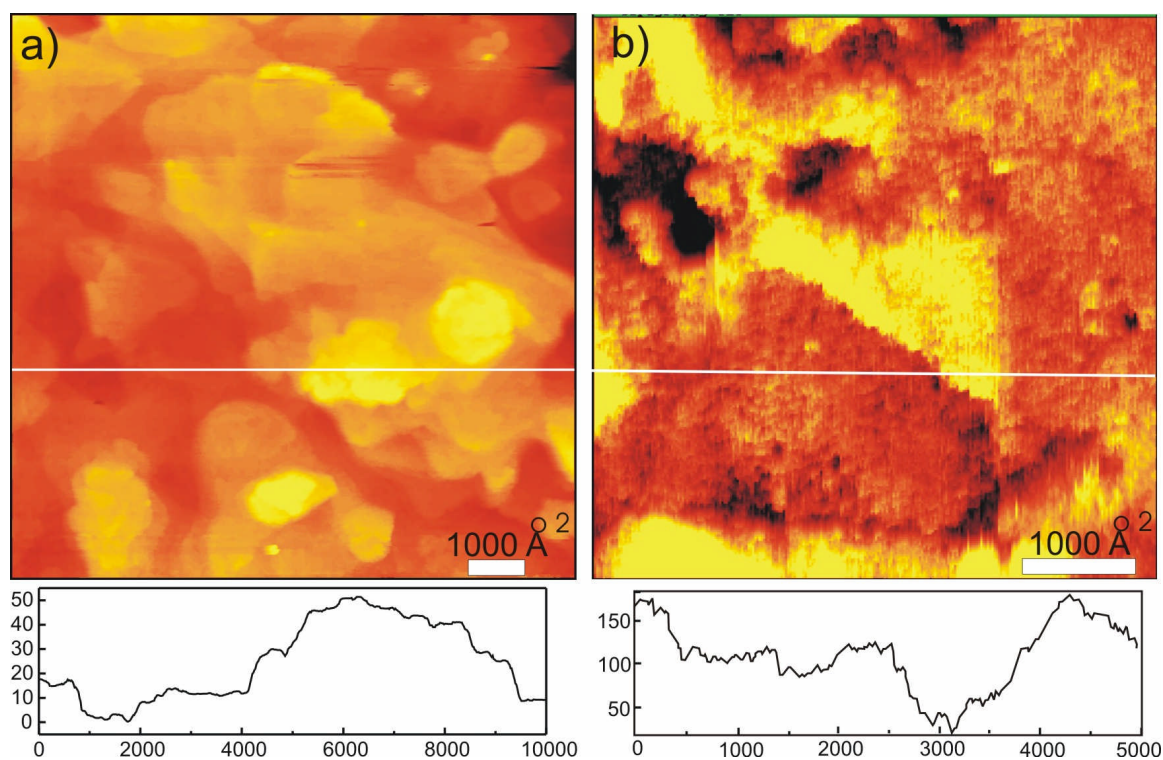


Fig. (4.2). STM images of an unpromoted Fe_2O_3 model catalyst surface a) before reaction, b) after 3 hours reaction at normal conditions, with the height profile along the indicated lines of each image is shown below.

The deactivated Fe_2O_3 sample after reaction (C in Fig. (4.1)) was brought back to the reactor after characterization with AES in the TDS chamber (without TPO cycles) and the reaction was continued. The sample showed the final activity of $\sim 0.5 \times 10^{15}$ molecules $\text{cm}^{-2} \text{s}^{-1}$, which was observed on the deactivated sample before.

For comparison with Fe_2O_3 , the reaction was done on clean Fe_3O_4 (Fig (4.3)). It showed a lower starting St conversion rate of $\sim 2 \times 10^{15}$ molecules $\text{s}^{-1}\text{cm}^{-2}$ and deactivates within ~ 45 min to the same steady state rate as seen on Fe_2O_3 . Post reaction characterization with AES showed that the surface was covered by carbon deposits ($I_C/I_{\text{Fe}} \sim 5.0$). After 4 TPO cycles the surface still exhibits the Fe_3O_4 (111) LEED pattern but the spots are wider and the background has increased which indicates an increase in surface roughness during reaction (E in table (4.2)).

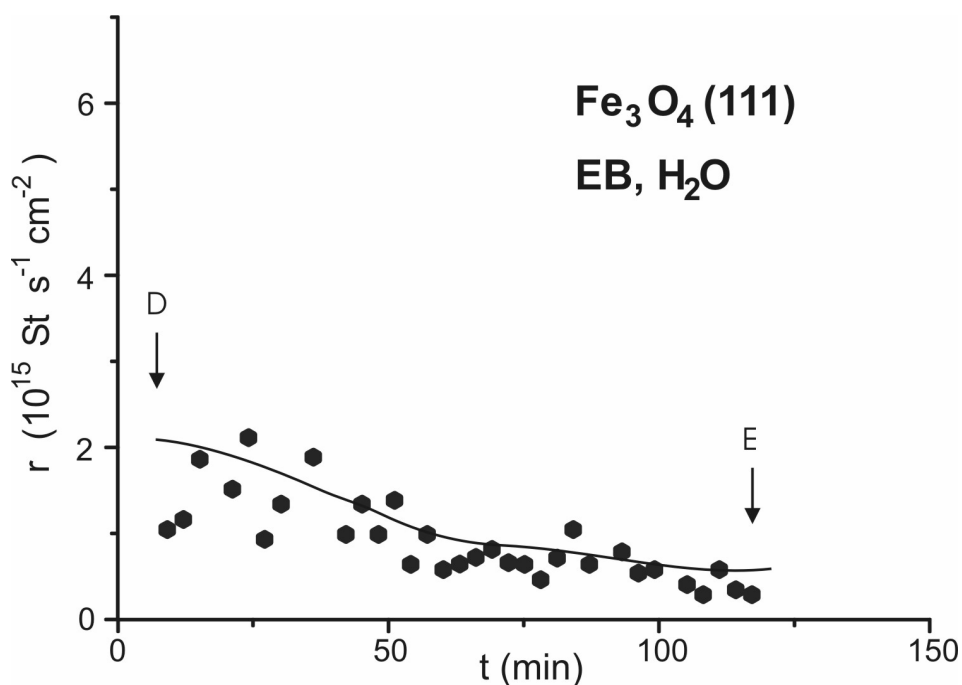
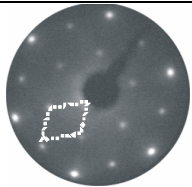
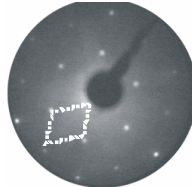


Fig. (4.3). Time dependence of the St conversion rate at 870 K, normal conditions, EB and H₂O in the feed, over Fe₃O₄. The labels **D** and **E** give the position where sample characterization was performed (see table (4.2)).

Table 4.2. LEED patterns and intensity ratios of the main Auger peaks of carbon, oxygen and iron before and after reaction for the unpromoted Fe₃O₄ model catalysts.

Treatment	LEED pattern	Phase from LEED	Auger intensity ratios		Label Fig. 4.3
			I _C /I _{Fe}	I _O /I _{Fe}	
Fe ₃ O ₄ Before reaction		Fe ₃ O ₄	0.0	2.9	D
Fe ₃ O ₄ After reaction with EB and H ₂ O		after 4 TPO cycle: Fe ₃ O ₄ , disordered	5.0	3.5	E

4.2.2 Dehydrogenation reaction on α -Fe₂O₃ (0001) model catalyst without steam (reductive conditions).

In order to study the role of water in the dehydrogenation reaction, reaction experiments were repeated on α -Fe₂O₃ (0001) model catalyst without steam by introducing 20 ml of He alone with the EB in order to maintain the total flow constant (reductive conditions). Fig. (4.4) shows that the St conversion exhibits a very similar, high starting conversion rate of $\sim 5 \times 10^{15}$ molecules s⁻¹ cm⁻², as in the reaction with steam. It also deactivates to the same steady state conversion rate as with steam. AES measurements after reaction (**G** in table (4.3)) showed that the surface was covered only with carbon deposits as shown in Fig. (4.5). The carbon layer was so thick that even after more than 10 cycles of TPO cycles only carbon is still seen on the surface and a signal from the Pt substrate start to appear. No LEED pattern of iron oxide could be seen, only LEED pattern of Pt(111) was visible. Since a closed α -Fe₂O₃ (0001) film reappeared after reoxidation, iron was obviously not lost but strongly reduced to Fe⁰ and formed metallic clusters or had alloyed with the Pt substrate.

The reaction was repeated and interrupted on a freshly prepared catalyst and interrupted after ~ 50 min (**F** in Fig. (4.4)). AES showed that the I_O/I_{Fe} ratio has decreased quite strongly to 2.0 and there is a big amount of carbon deposits (**F** in table (4.3)). After 5 TPO cycles again no LEED pattern of any of the iron oxide phases was visible which support the earlier result that the iron oxide was strongly reduced without the presence of water in the feed.

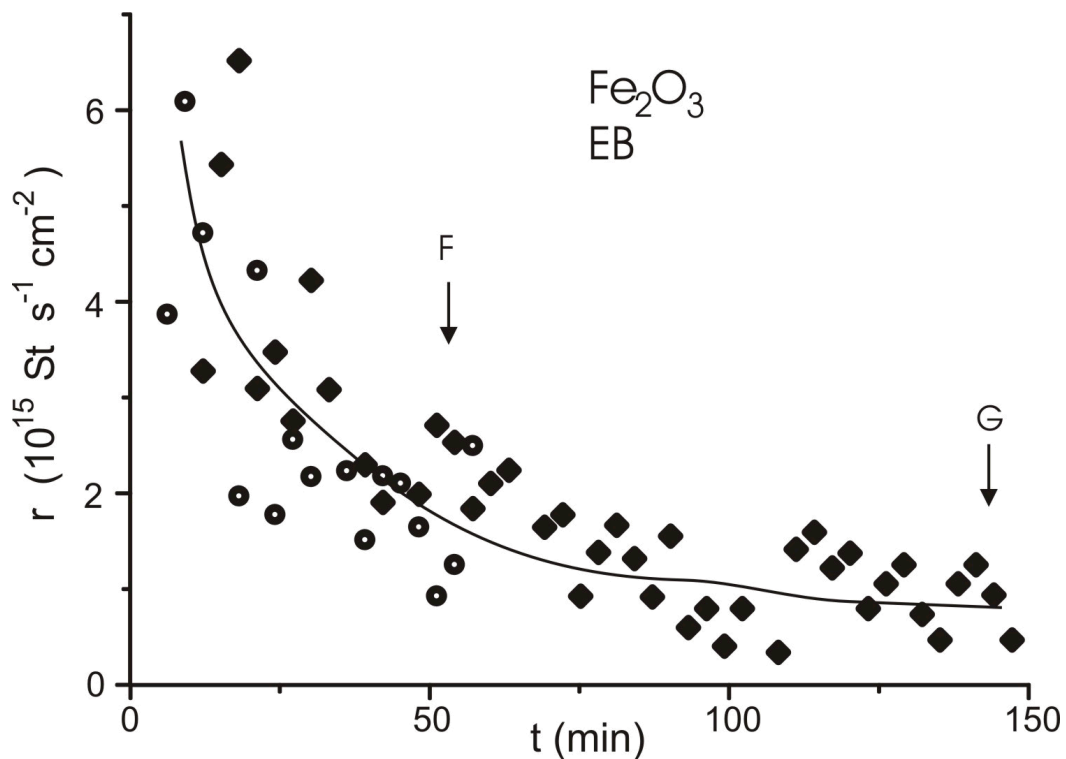
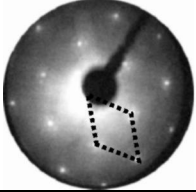


Fig. (4.4). Time dependence of the St conversion rate at 870 K, reductive conditions, EB and He in the feed, over Fe_2O_3 . The labels F and G give the position where sample characterization was performed (see table (4.3)).

Table 4.3. LEED patterns and intensity ratios of the main Auger peaks of carbon, oxygen and iron before and after reaction (reductive conditions) on unpromoted Fe_2O_3 model catalysts.

Treatment	LEED pattern	Phase from LEED	Auger intensity ratios		Label in Fig. 4.4
			I_C/I_{Fe}	I_O/I_{Fe}	
Fe_2O_3 before reaction		Fe_2O_3	0	3.5	-
After reaction with EB	no pattern		5.3	2.0	F
			∞	-	G

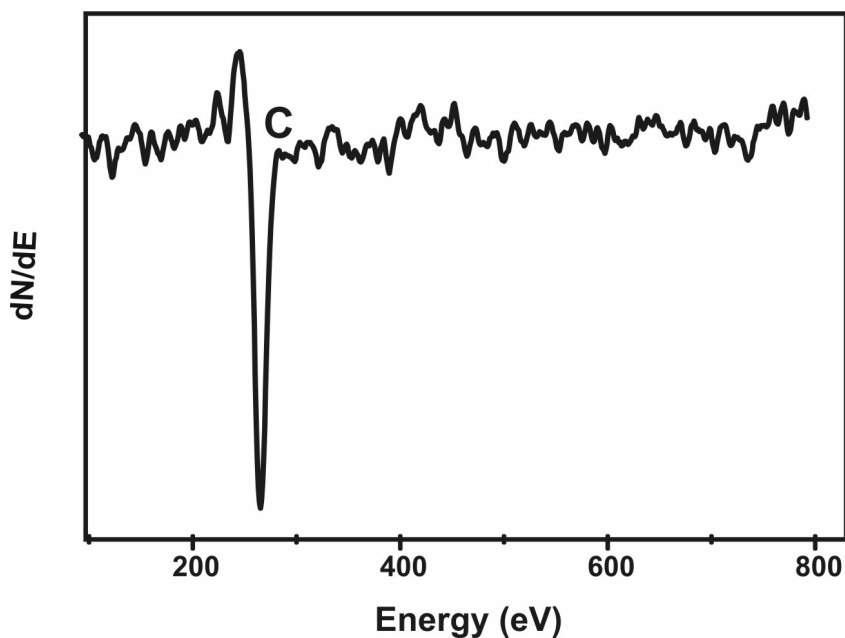


Fig. (4.5). AES spectrum of Fe_2O_3 model catalyst after reaction at 870 K (reductive conditions), EB and He in the feed. Position **G** in Fig. (4.4).

4.2.3 Dehydrogenation reaction on $\alpha\text{-Fe}_2\text{O}_3$ (0001) model catalyst in presence of steam and oxygen (oxidative conditions).

The influence of dosing some oxygen to the feed on the reaction and deactivation behavior was studied. We have used a mixture of 20 % oxygen in helium for dosing oxygen. The standard ratio of EB to oxygen (O_2) was $\sim 2:1$ (oxidative conditions, table 3.1). Fig (4.6) shows that, the high initial St conversion rate $\sim 6 \times 10^{15}$ molecules $\text{s}^{-1} \text{cm}^{-2}$ decreases only slightly with time on stream, a constant level of $\sim 5 \times 10^{15}$ molecules $\text{s}^{-1} \text{cm}^{-2}$ is maintained. AES measurement after the experiment (at **H**) showed that the carbon content is low $I_{\text{C}}/I_{\text{Fe}} \sim 0.8$, and that the $I_{\text{O}}/I_{\text{Fe}}$ ratio is not changed. LEED after 1 TPO cycle showed that the film is still exhibits the $\alpha\text{-Fe}_2\text{O}_3$ (0001) pattern but the surface is rougher since the background is higher and the spots are broadened (**H** in table (4.4)).

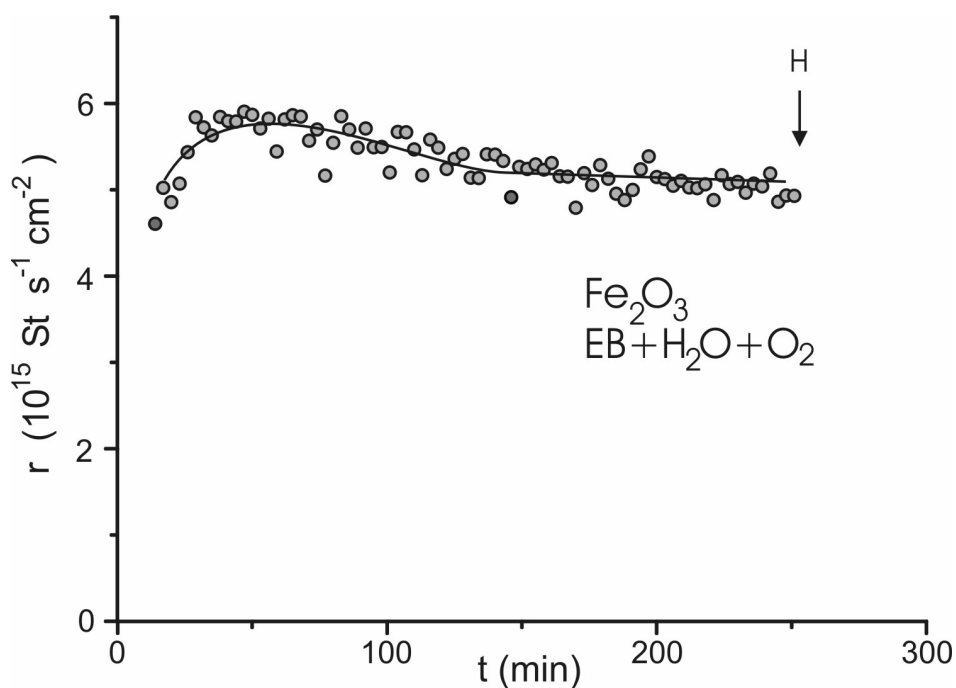
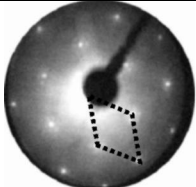
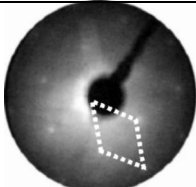


Fig. (4.6). Time dependence of the St conversion rate at 870 K, oxidative conditions, EB, H₂O and O₂ in the feed, over Fe₂O₃. The label **H** gives the position where sample characterization was performed (see table (4.4)).

Table 4.4. LEED patterns and intensity ratios of the main Auger peaks of carbon, oxygen and iron for the unpromoted Fe₂O₃ model catalysts, before and after reaction with EB, water and oxygen in the feed (oxidative conditions).

Treatment	LEED pattern	Phase from LEED	Auger intensity ratios		Label Fig.4.6
			I _C /I _{Fe}	I _O /I _{Fe}	
Fe ₂ O ₃ before reaction		Fe ₂ O ₃	0	3.5	-
Reaction with EB+ H ₂ O+ O ₂		after 1 TPO cycle: Fe ₂ O ₃ , disordered	0.8	3.4	H

4.2.5 Dehydrogenation reaction on α -Fe₂O₃ (0001) model catalyst in presence of steam and oxygen, effect of oxygen concentration on the activity.

In order to determine the optimal concentration of oxygen needed to stabilize the high styrene conversion rate, the effect of decreasing the EB/O₂ molar ratio was studied. The oxygen ratio was decreased stepwise after reaction periods of ~ 50 minutes each.

Fig. (4.7) shows that decreasing the EB: O₂ ratio to 1:0.3 and to 1:0.13 leads to a partial deactivation and a decrease in the steady state St conversion rate. The conversion rate can be regained after increasing the EB: O₂ ratio again as shown in Fig. (4.7a) but not fully to the original starting values. This maybe due to this time (~ 50 min) was not enough for the full removal (i.e. burning) of the carbon deposits formed or the complete reoxidation of the surface to Fe₂O₃.

The relationship between the steady state rates taken from Fig. (4.7a) and EB:O₂ molar ratio for p(O₂) decreasing values is shown in Fig. (4.7b). The EB:O₂ ratio (1:0.5) turns to be the optimal value needed to maintain this high conversion rate. This agrees well with an estimation we have made which is presented in detail in the discussion in chapter 5.

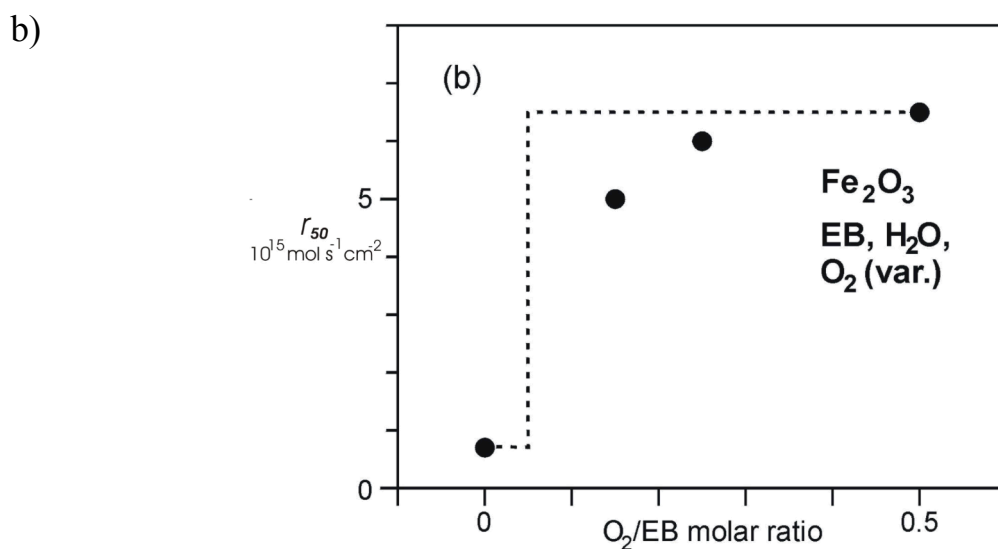
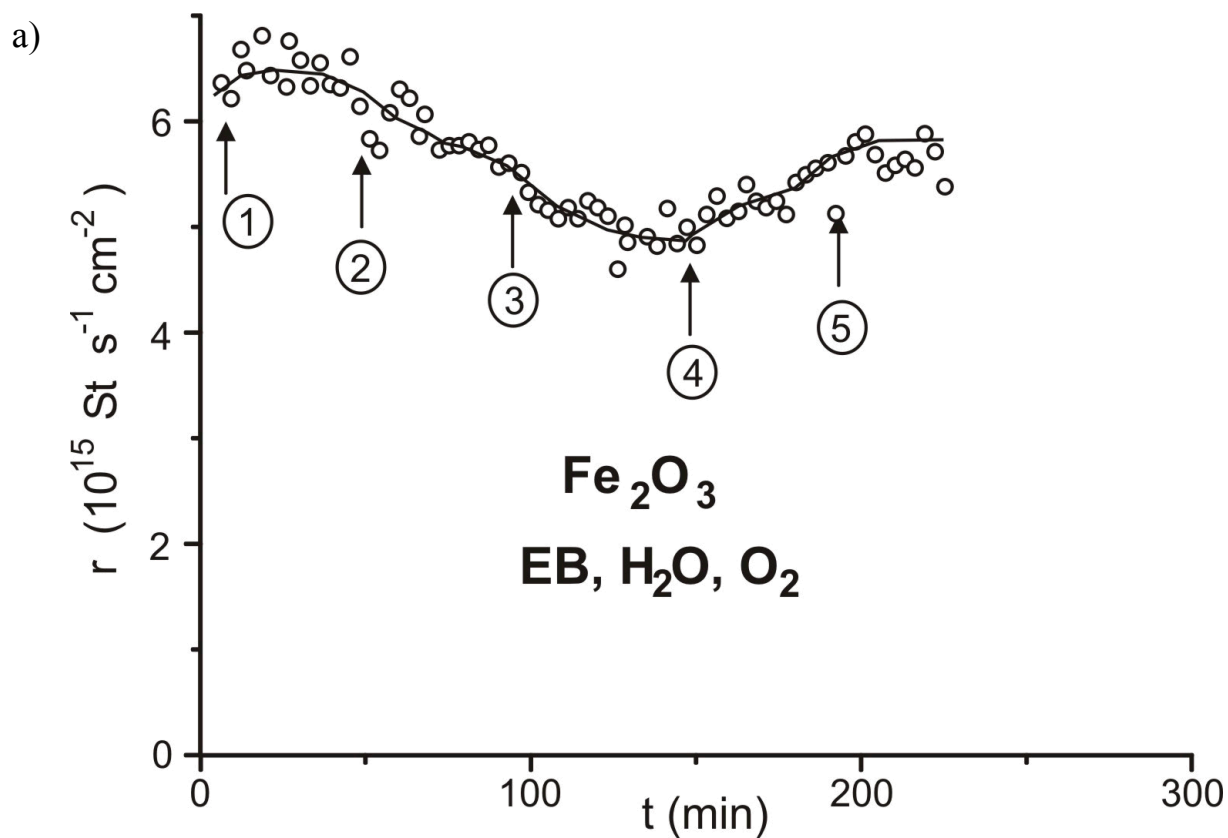


Fig. (4.7). a) Conversion dependence of the St conversion rate at 870 K, oxidative conditions, EB, H₂O and O₂ in the feed, over Fe₂O₃ on EB/O₂ molar ratio which is changed at the position labeled by numbers (1) 1:0.5, (2) 1:0.3, (3) 1:0.13, (4) 1:0.3 and (5) 1:0.5.

b) Dependence of the steady state rate after 50 min of reaction at constant EB:O₂ molar ratio (r_{50}). The dotted line is the estimated O₂/EB molar ratio which is theoretically needed to stabilize the high initial St conversion (see chapter 5).

4.2.4 Dehydrogenation reaction on α -Fe₂O₃ (0001) model catalyst in presence of steam and oxygen. Oxygen on and off experiments.

The response of the conversion rate on the oxygen content in the feed is studied in O₂ on-off experiments. Fig. (4.8a) shows that switching off the oxygen after 2 hrs results in a fast deactivation. In fact it is considerably faster than when starting with the clean surface without oxygen (Fig. 4.1). After 30 min the oxygen was switched on again. Within ~ 20 minutes the initial activity is regenerated. Post reaction characterization with AES showed that at point **I** in Fig.(4.8a) there is a small amount of carbon ($I_C/I_{Fe} \sim 1.1$) and almost no change in the ($I_O/I_{Fe}=3.2$). After 1 TPO cycle the film shows the typical LEED pattern of rough Fe₂O₃ (I in table (4.5)) but the spots are wider with weak intensity.

The reaction was repeated as shown in Fig. (4.8b). After ~ 4 hours reaction in the presence of oxygen in the feed, oxygen switch-off and -on were repeated twice. The deactivation and reactivation behavior of the catalyst is reproducible. 30 minutes after switching the oxygen off (**J** in Fig. (4.7b)), the reaction was interrupted and the sample transferred back to the UHV chamber for post-reaction characterization. AES shows that there are more carbon deposits on the surface ($I_C/I_{Fe}= 4.0$) and after 3 cycles of TPO, LEED shows mainly the Fe₃O₄ pattern with only weak contributions from the Fe₂O₃. The surface is rougher as concluded from the high background of the LEED image. The deactivation rate on a fresh Fe₂O₃ model catalyst (from Fig. (4.1)) without oxygen in the feed (inserted low curve in Fig (4.8a) for comparison) is much slower. The reason for the fast deactivation and reactivation, after hours on stream may be an increase of the roughness and disorder of the catalyst film as a result of local reduction-oxidation process, leading to an increase in the exchange between the solid and gas phase.

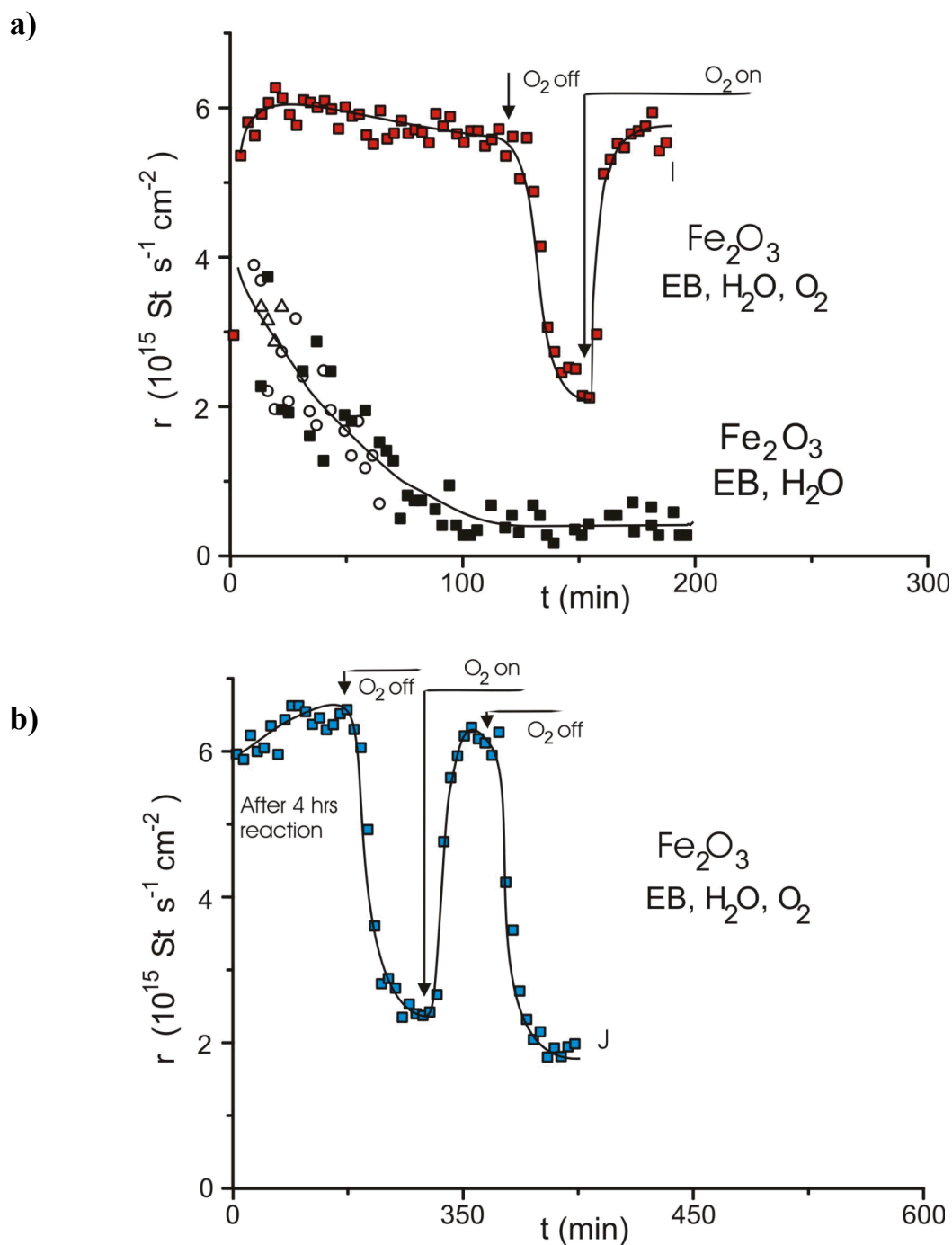
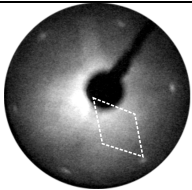
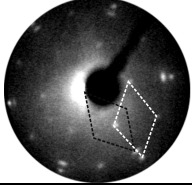


Fig. (4.8). Deactivation of the St conversion rate at 870 K, oxidative conditions, EB, H₂O and O₂ in the feed, over Fe₂O₃ after switching O₂ on and off. The label I and J give the position where sample characterization was performed (see table (4.5)). For comparison, the deactivation when starting with a well ordered Fe₂O₃ without O₂ in the feed (from Fig. (4.1)) is shown in (a).

Table 4.5. LEED patterns and intensity ratios of the main Auger peaks of carbon, oxygen and iron, for the unpromoted Fe_2O_3 model catalysts after oxygen on- off experiments. (Fig. (4.8a,b)).

Treatment	LEED pattern	Phase from LEED	Auger intensity ratios		Label in Fig.4.8
			I_C/I_{Fe}	I_O/I_{Fe}	
Reaction with EB, H ₂ O O ₂ on - off Fig. 4.8a		after 1 TPO cycle: Fe_2O_3 , disordered	0.7	3.4	I
Reaction with EB, H ₂ O O ₂ on - off Fig. 4.8b		after 3 TPO cycle: Fe_2O_3 + Fe_3O_4	4.0	3.3	J

4.2.6 Dehydrogenation reaction on α - Fe_2O_3 (0001) model catalyst in presence of steam and oxygen at different temperatures.

Fig. (4.9) shows the dependence of the St conversion rate over unpromoted Fe_2O_3 model catalyst under oxidative conditions on the reaction temperature. The conversion rate increases with reaction temperature reflecting the endothermicity of the reaction, this result agrees well with the literature [2]. Oxygen was added in these experiments in order to keep the catalyst surface clean and prevent deactivation during reaction, the activation energy of the clean active surface derived from this measurement using the Arrhenius equation is presented and discussed in chapter 5.

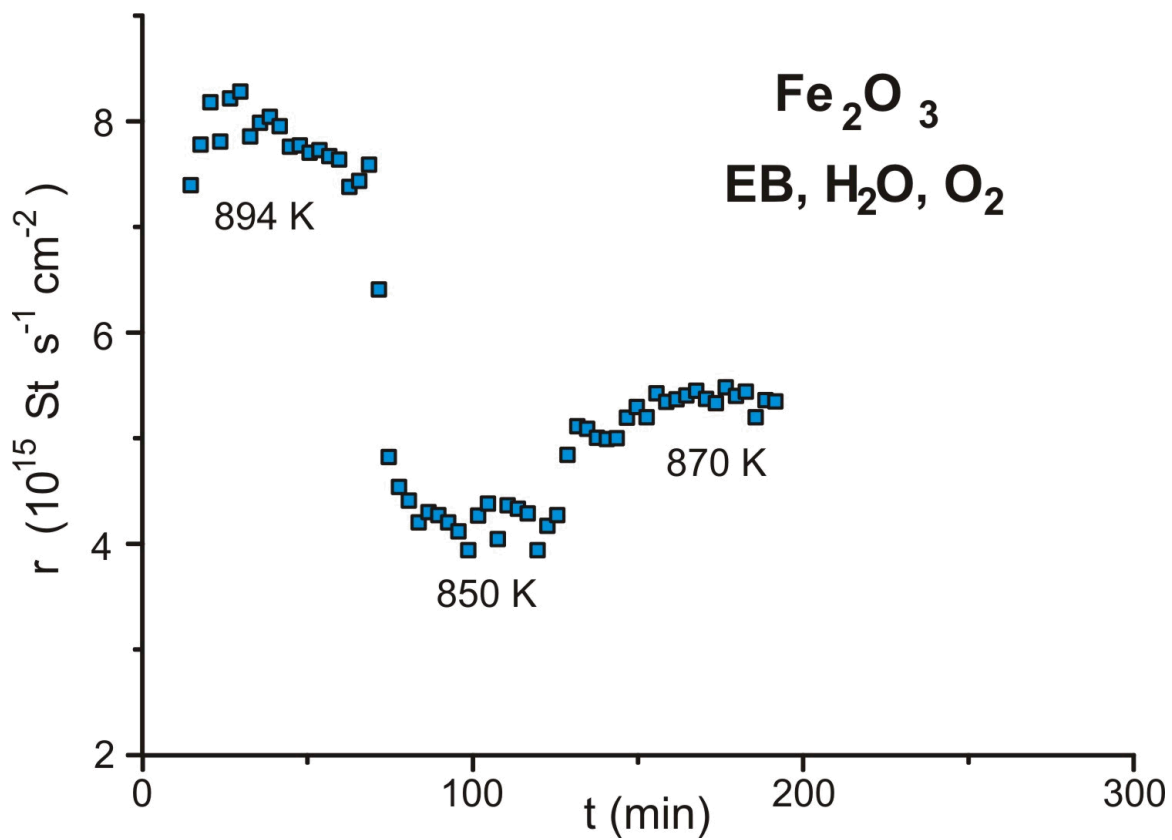


Fig. (4.9). The dependence of the St conversion rate under oxidative conditions, EB, H₂O and O₂ in the feed, over Fe₂O₃ on reaction temperature

4.3 Promoted iron oxide (KFe_xO_y) model catalysts

4.3.1 Dehydrogenation reaction on KFe_xO_y model catalyst in presence of steam

, (normal conditions), and the effect of potassium content.

Fig (4.10) compares the St conversion rate on a potassium promoted catalyst with intermediate potassium content ($I_{\text{K}}/I_{\text{Fe}} \sim 2.2$) with that of the unpromoted Fe_2O_3 film. The catalyst starts with a similarly high conversion rate of $\sim 4 \times 10^{15}$ molecules $\text{s}^{-1} \text{cm}^{-2}$ but deactivation of the promoted catalyst is much slower. After reaction there was an increase in the carbon deposits on the catalyst surface as AES showed ($I_{\text{C}}/I_{\text{Fe}} \sim 2.0$) which, however, is less than in case of the reaction on unpromoted catalyst. There is a moderate loss in the potassium content during the reaction (1 in table (4.6)).

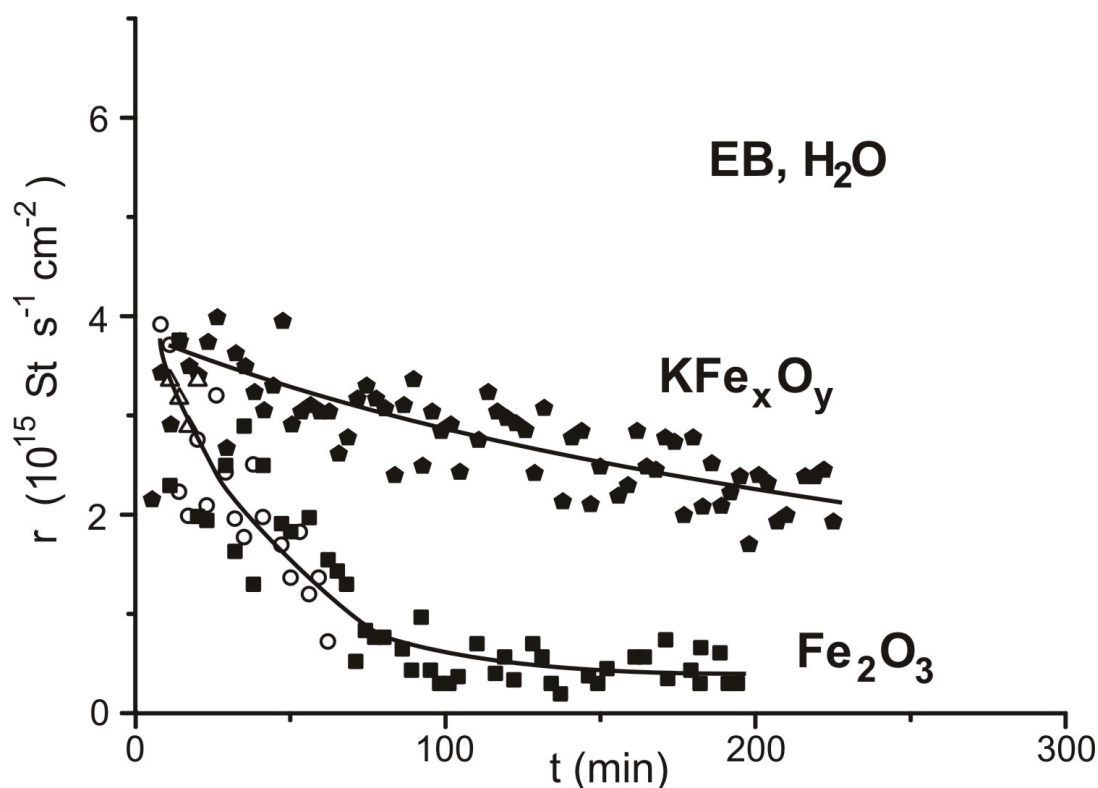


Figure 4.10. Time dependence of the St conversion rate at 870 K, normal conditions, EB and H_2O in the feed, over KFe_xO_y with a ($I_{\text{K}}/I_{\text{Fe}}=2.2$). The lower curve shows the St conversion rate over unpromoted Fe_2O_3 for comparison.

When the potassium content is lower ($I_K/I_{Fe} \sim 0.9$) Fig. (4.11a), the catalyst has a higher starting conversion rate of $\sim 5 \times 10^{15}$ molecules $s^{-1}cm^{-2}$, but a faster deactivation. Also here there is a moderate loss in the potassium content occurs during the reaction but the carbon deposition on the catalyst is higher ($I_C/I_{Fe} = 3.0$) compare cases 1 and 2 shown in table (4.6)).

The reaction was then done over a promoted catalyst with a higher potassium content ($I_K/I_{Fe} \sim 4.2$). In order to obtain this high potassium content the sample was only annealed in oxygen at 870 K after potassium deposition. Under these conditions a $KFeO_2$ thin film is present on the catalyst surface as explained in section 2.2.2. Fig. (4.11b) shows that it has a very low starting St conversion rate of $\sim 2 \times 10^{15}$ molecules $s^{-1}cm^{-2}$, but deactivation is considerably slower. Post-reaction characterization with AES shows a moderate loss of potassium but only little amount of carbon deposits ($I_C/I_{Fe} \sim 1.1$) (case 3 in table (4.6)). High potassium content thus leads to low initial activity and low rate of deactivation while a low potassium content results in a high initial activity but fast deactivation. This also shows clearly that $KFeO_2$ is not the active phase for this reaction.

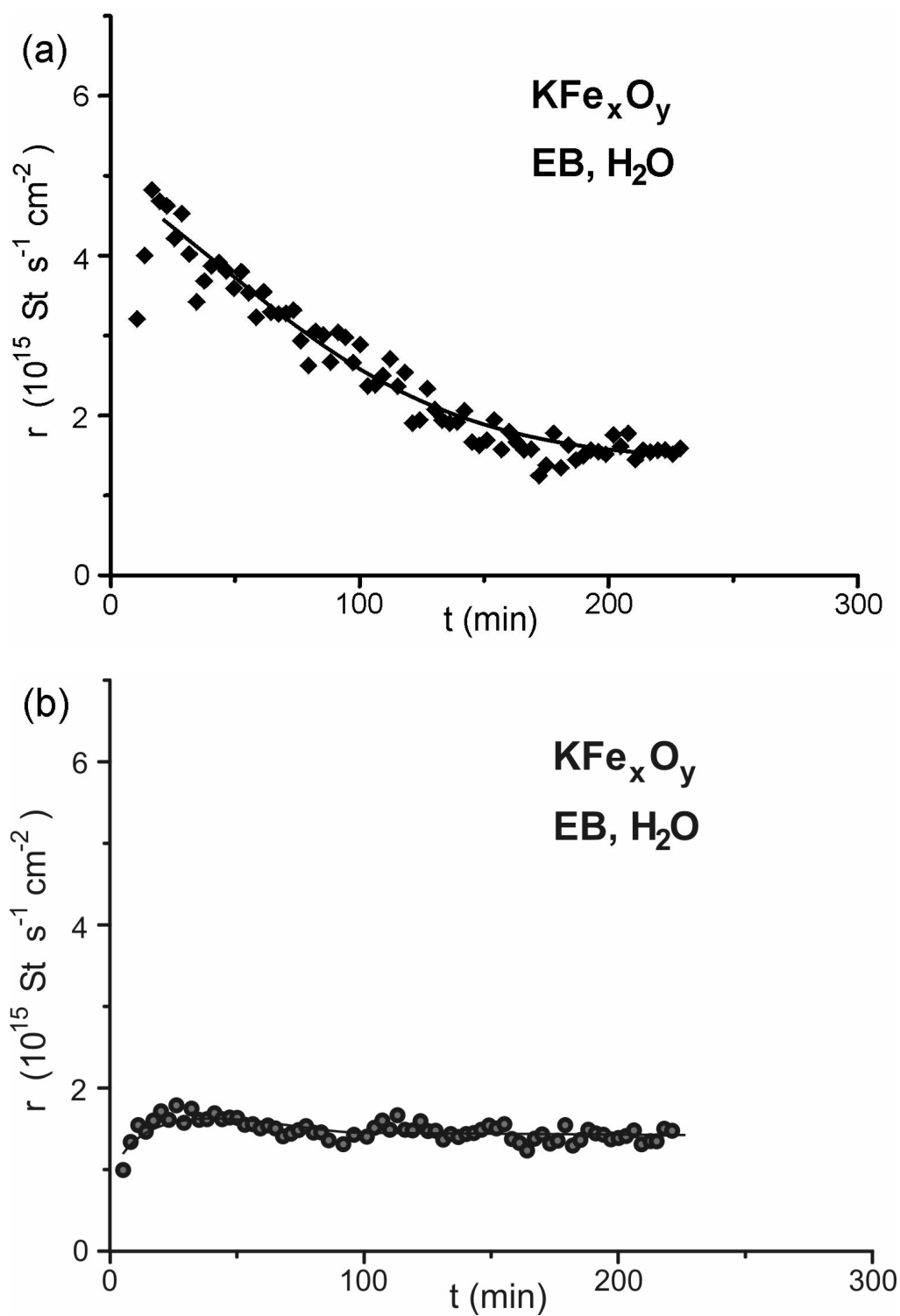


Fig. (4.11). Time dependence of the St conversion rate at 870 K, normal conditions, EB and H_2O in the feed, over KFe_xO_y with a) ($I_{\text{K}}/I_{\text{Fe}} \sim 0.9$), b) ($I_{\text{K}}/I_{\text{Fe}} \sim 4.2$).

Table 4.6. LEED patterns and intensity ratios of the main Auger peaks of carbon, oxygen, potassium and iron before and after reaction with EB and H₂O in the feed (normal conditions) for the promoted KFe_xO_y model catalysts with different K-loading.

KFe _x O _y catalyst treatment		Auger intensity ratios			LEED patterns	
		I _K /I _{Fe}	I _O /I _{Fe}	I _C /I _{Fe}	before	after
(1) EB+H ₂ O	before react.	2.2	3.0	0		
	after react.	1.9	2.8	2.0		
(2) EB+H ₂ O	before react.	0.9	2.3	0.0		
	after react.	0.7	2.7	3.0		
(3) EB+H ₂ O	before react.	4.2	2.8	0	No LEED	No LEED
	after react.	3.1	2.9	1.1		

4.3.2 Carbon formation from dehydrogenation reaction on potassium promoted KFe_xO_y and unpromoted Fe₂O₃ catalysts (normal conditions).

The buildup of carbon deposits was studied by performing the reaction on a promoted catalyst with an I_K/I_{Fe} = 2.2 and an unpromoted Fe₂O₃ catalyst under normal reaction conditions (table (3.1)). The reaction was interrupted after a few hrs from time on stream and the catalyst was characterized by AES, after that, the reaction was continued. Fig. (4.12) shows that the carbon deposits on unpromoted catalysts increases faster and reach a higher steady state level than on the promoted iron oxide (KFe_xO_y) catalyst.

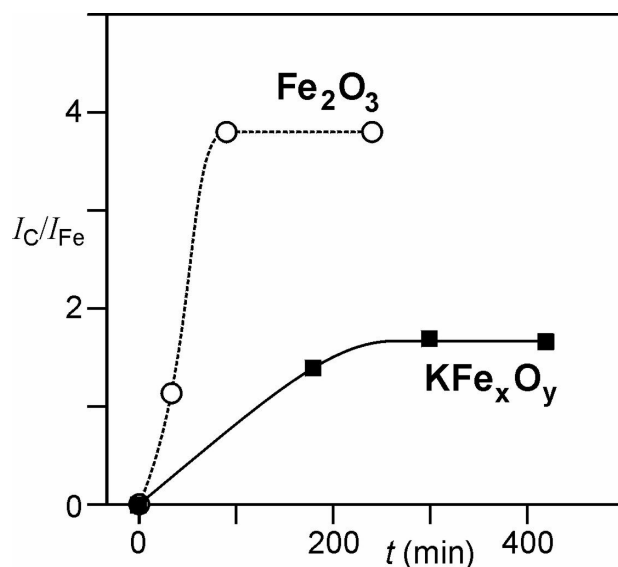


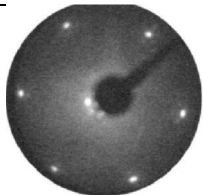
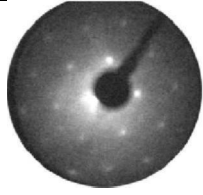
Figure (4.12). The build-up of carbon deposits over the unpromoted Fe_2O_3 and potassium promoted catalyst (KFe_xO_y) $I_C/I_{Fe} \sim 2.7$, expressed by the intensity ratios of the main Auger peaks of carbon to iron (I_C/I_{Fe}) with time on stream (normal conditions).

4.3.3 The effect of steam reactivation on the dehydrogenation reaction over potassium promoted (KFe_xO_y) model catalysts.

Reactivation in industry is done by “steaming”, i.e. by passing only steam over the catalyst. This was simulated in the following way. The reaction was first run for ~4 hrs on a KFe_xO_y model catalyst ($I_K/I_{Fe} \sim 2.3$), Fig (4.13a). The behavior is the same as in Fig (4.10). AES after reaction showed a similar small amount of carbon deposits ($I_C/I_{Fe} \sim 0.5$) and a moderate loss of potassium (1 in table (4.7)). The reaction was then continued on the catalyst after steaming for ~ 15 min (reactivation). The EB flow was switched on again and the reaction continued. Fig (4.13b) shows that the catalyst exhibits a higher starting conversion rate of $\sim 5 \times 10^{15}$ molecules $s^{-1} cm^{-2}$ but deactivation is faster now compared to the reaction before reactivation Fig (4.13.a). Characterization by AES after reaction shows a strong increase in the carbon deposits ($I_C/I_{Fe} \sim 4.4$) and a strong loss of potassium ($I_K/I_{Fe} \sim 0.6$), case 2 in table (4.7). The

LEED pattern after the reactivation and reaction, has changed to that of Fe₃O₄ which is consistent with the strong loss of potassium. The reactivation treatment was repeated on fresh promoted catalyst which this time was characterized before and after the reactivation (Table (4.8)). Here it is obvious that strong potassium loss occur during this reactivation period. In a further experiment, a promoted catalyst covered with carbon deposits was steamed. The treatment effectively removed the carbon deposits.

Table 4.7. LEED patterns and intensity ratios of the main Auger peaks of carbon, oxygen, potassium and iron before and after reaction with EB and H₂O in the feed for the promoted KFe_xO_y model catalysts and effect of reactivation with steam.

KFe _x O _y catalyst treatment		Auger intensity ratios			LEED patterns	
		I _K /I _{Fe}	I _O /I _{Fe}	I _C /I _{Fe}	before	after
(1) EB+H ₂ O	before react.	2.3	2.7	0		No LEED
	after react.	1.8	2.5	0.5		
(2) After react. and 15 min in H ₂ O EB+H ₂ O	before react.	**	**	**	No LEED	
	after react.	0.6	2.6	4.4		

- No AES measurement was done.

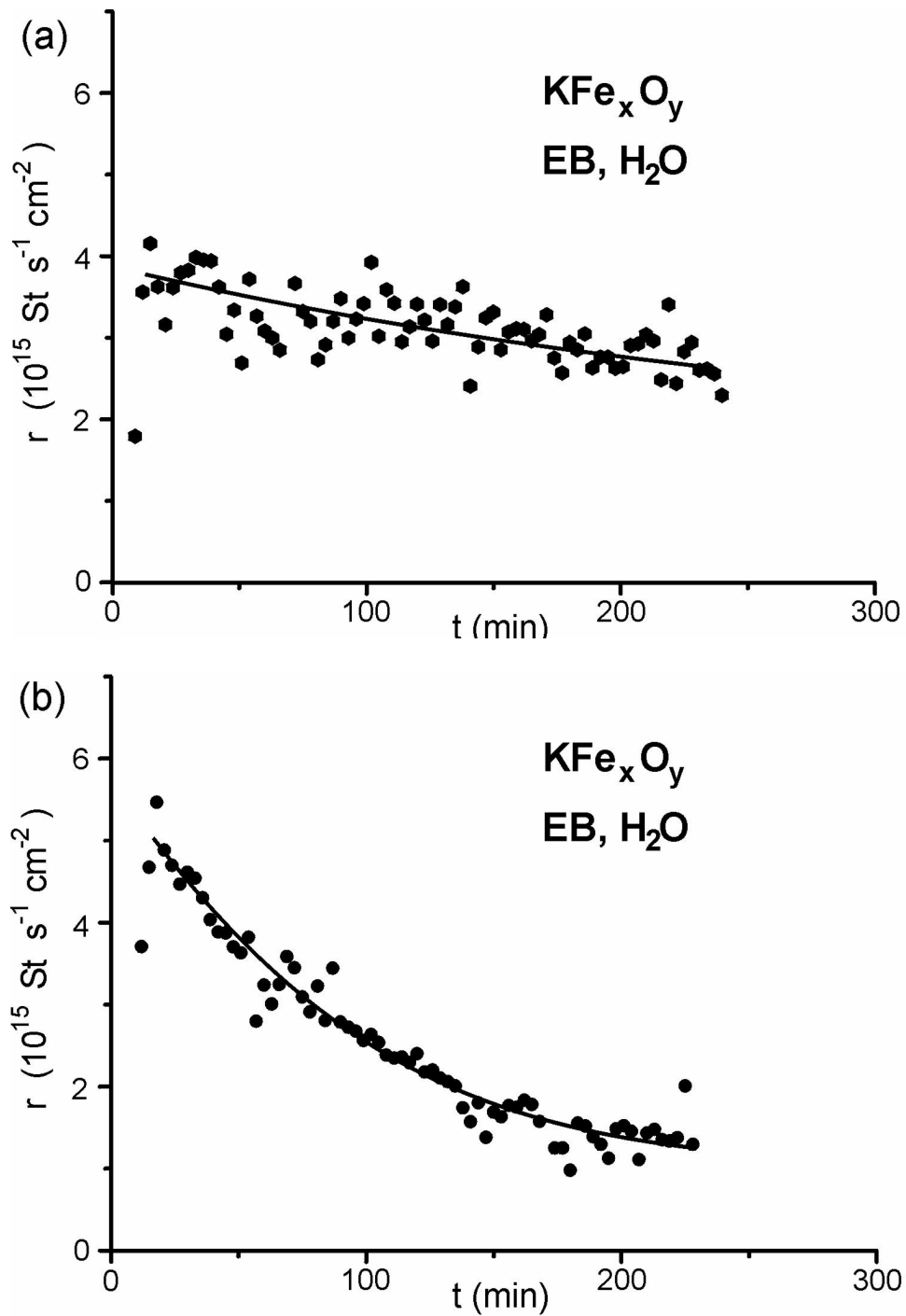
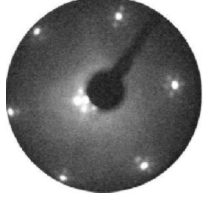


Fig. (4.13). Time dependence of the St conversion rate at 870 K, normal conditions, EB and H_2O in the feed, over a potassium promoted (KFe_xO_y) catalyst with ($I_K/I_{Fe} \sim 2.2$), a) before reactivation with water, b) after reactivation with water for 15 min.

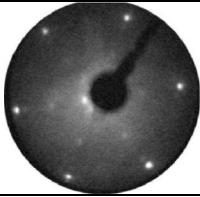
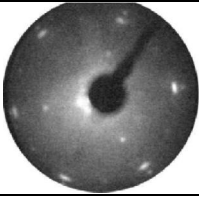
Table 4.8. LEED patterns and intensity ratios of the main Auger peaks of carbon, oxygen, potassium and iron before and after reaction with EB and H₂O in the feed (normal conditions), for a potassium promoted (KFe_xO_y) model catalysts with (I_K/I_{Fe}~2.8), before and after reactivation with water for 15 min.

KFe _x O _y catalyst treatment		Auger intensity ratios			LEED patterns	
		I _K /I _{Fe}	I _O /I _{Fe}	I _C /I _{Fe}	before	after
EB+H ₂ O	before H ₂ O treatment	2.8	2.7	0.0		No LEED
	after 15 min in H ₂ O	1.2	2.9	0.0		

4.3.4 Dehydrogenation reaction on a potassium promoted KFe_xO_y model catalyst in presence of steam and oxygen (oxidative conditions).

The influence of introducing some oxygen to the feed on the reaction rate and deactivation behavior was studied on a promoted catalyst (I_K/I_{Fe}=1.0) and compared to the unpromoted Fe₂O₃ catalyst. Fig. (4.13) shows that under (oxidative conditions (table (3.1))), a high conversion rate of $\sim 7 \times 10^{15}$ molecules s⁻¹cm⁻² is maintained and no significant deactivation is observed. The AES measurement after reaction (table (4.9)) shows that the carbon content is low (I_C/I_{Fe} = 0.6) and the I_O/I_{Fe} ratio is almost unchanged. Also the potassium content is almost unchanged, LEED after 1 TPO showed that the film still exhibits the same (1x1) pattern (i.e. no phase change) but the surface is rougher as concluded from the high background in the LEED image.

Table 4.9. LEED patterns and intensity ratios of the main Auger peaks of carbon, oxygen, potassium and iron before and after reaction with EB, H₂O and O₂ in the feed (oxidative conditions) for a potassium promoted KFe_xO_y model catalyst ($I_K/I_{Fe} \sim 1.0$).

KFe _x O _y catalyst treatment		Auger intensity ratios			LEED patterns	
		I_K/I_{Fe}	I_O/I_{Fe}	I_C/I_{Fe}	before	after
EB+H ₂ O +O ₂	before react.	1.0	2.0	0.0		
	after react.	0.9	1.9	0.6		

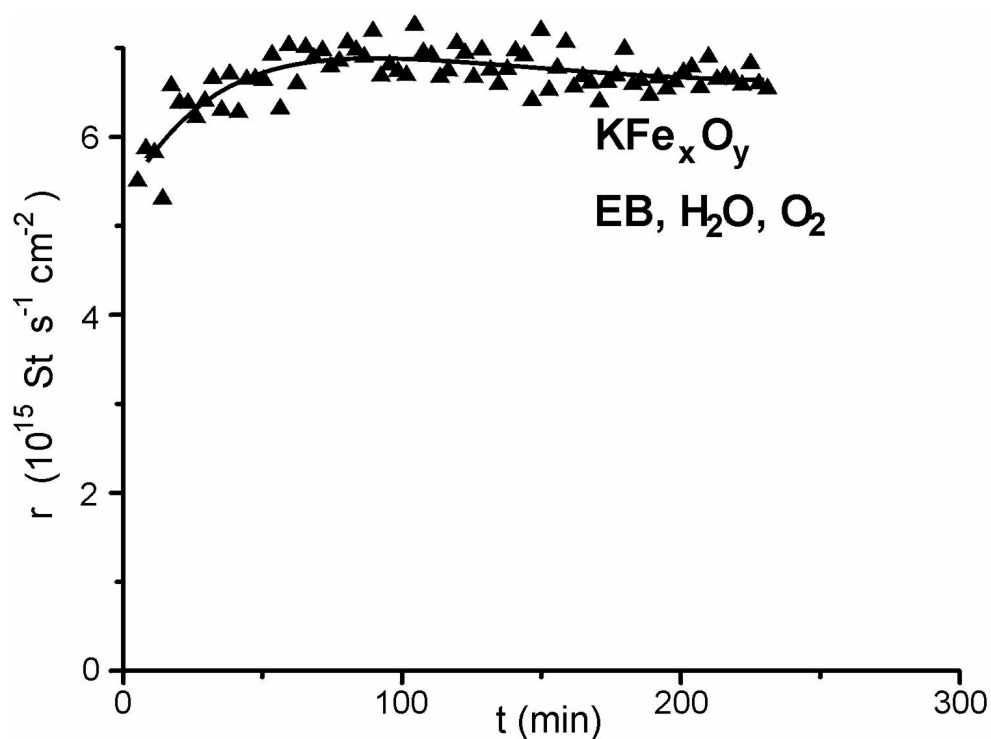


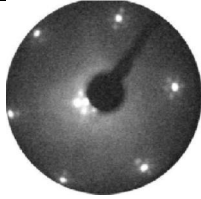
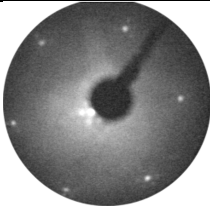
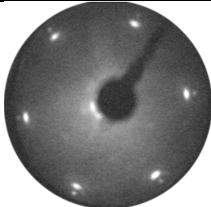
Fig. (4.14). Time dependence of the St conversion rate at 870 K, oxidative conditions, EB, H₂O and O₂ in the feed, over a potassium promoted (KFe_xO_y) model catalyst ($I_K/I_{Fe} = 1.0$).

4.3.5 Dehydrogenation reaction on KFe_xO_y model catalyst without steam, effect of potassium promotion on the reduction of the catalyst (reductive conditions).

Here the effect of promoting the iron oxide with potassium on the reduction of the catalyst and the role of water in the reaction are studied. The reaction was done on a promoted catalyst with a $\text{I}_\text{K}/\text{I}_\text{Fe} \sim 1.2$ and $\text{I}_\text{O}/\text{I}_\text{Fe} \sim 2.5$ in absence of steam (reductive conditions (table (3.1))). The reaction was interrupted after 45 min. Characterization with AES showed that the ratio $\text{I}_\text{O}/\text{I}_\text{Fe}$ is unchanged, case 1 in table (4.10). This indicates that there was no significant reduction of the catalyst, in contrast to the unpromoted catalyst which has showed a strong reduction in the absence of water (see **F** table (4.2)). This means that promotion with potassium stabilizes the catalyst against reduction.

Fig. (4.15) shows the St conversion rate over a KFe_xO_y catalyst with a ($\text{I}_\text{K}/\text{I}_\text{Fe} \sim 1.9$) with water and EB in the feed (normal conditions (table (3.1))). After ~ 2 hours the water was switched off and the reaction was run under reductive conditions (table (3.1)). There was no sudden decrease which indicates that water is not involved in the rate determining step (RDS) of the reaction. Post reaction characterization with AES showed an increase in the carbon deposits (case 2 in table (4.10)). The $\text{I}_\text{O}/\text{I}_\text{Fe}$ ratio before and after reaction was similar, which shows that there was no strong reduction.

Table(4.10). LEED patterns and intensity ratios of the main Auger peaks of carbon, oxygen, potassium and iron before and after reaction with EB and H₂O or He in the feed over the promoted KFe_xO_y model catalysts.

KFe _x O _y catalyst treatment		Auger intensity ratios			LEED patterns	
		I _K /I _{Fe}	I _O /I _{Fe}	I _C /I _{Fe}	before	after
(1) EB+He	before reaction	1.2	2.4	0.0		No LEED
	after 45 min reaction no	0.9	2.4	0.8		
(2) EB+H ₂ O	before reaction	1.9	2.2	0.0		
	After reaction	1.3	2.0	2.1		

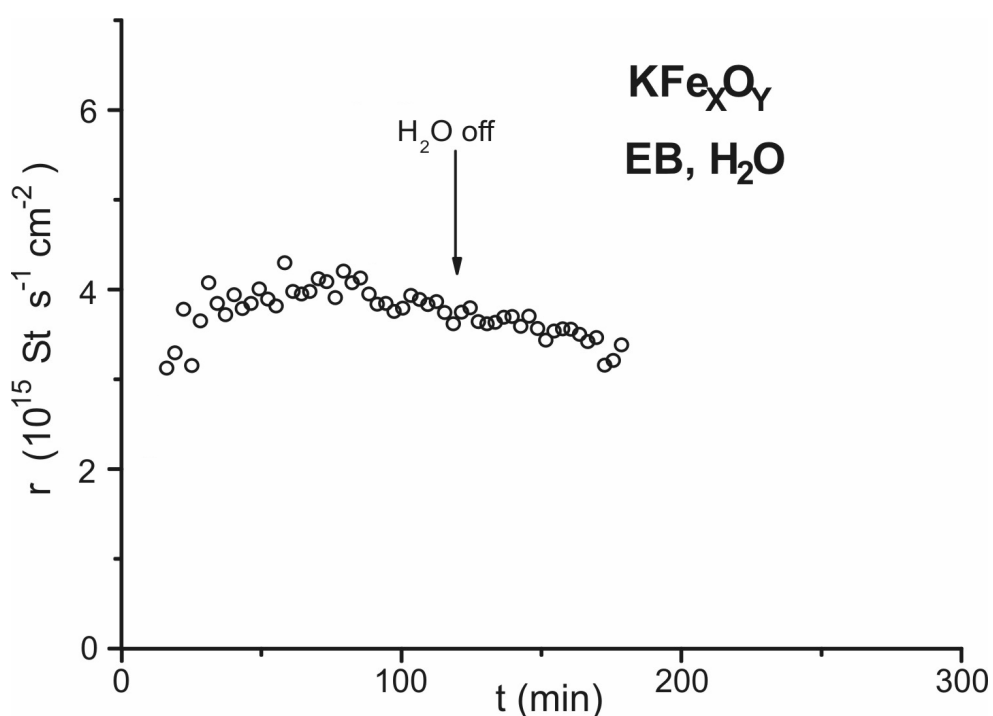


Fig. (4.15). Time dependence of the St conversion rate at 870 K, normal conditions, EB, and H₂O over KFe_xO_y with (I_K/I_{Fe}~ 1.9). After 2 hrs H₂O was switched off and the reaction is run under reductive conditions.

4.3.6 Dehydrogenation reaction on KFe_xO_y (0001) model catalyst in presence of

steam and oxygen. Oxygen on and off experiments.

The response of the conversion rate on the oxygen content in the feed was studied in on-off experiments. The switching off of oxygen after ~ 4 hours reaction on a KFe_xO_y ($\mathbf{I}_\text{K}/\mathbf{I}_\text{Fe} \sim 2.7$) Fig. (4.16a), under oxidative conditions (table 3.1), showed that the deactivation rate was very slow. It is slower than on the unpromoted catalyst Fig. (4.8a). After 30 min, oxygen was switched on again and within 20 minutes the initial conversion rate was regained. This supports that oxygen and promotion by potassium play a very similar role in the reaction.

4.3.7 Dehydrogenation reaction on KFe_xO_y (0001) model catalyst in presence of steam and oxygen. Effect of oxygen concentration.

The effect of decreasing the oxygen concentration added to the feed on the deactivation and St conversion rate for a promoted catalyst ($\mathbf{I}_\text{K}/\mathbf{I}_\text{Fe} \sim 2.7$) is shown in Fig. (4.16b). The oxygen concentration was decreased stepwise after 50 minutes each. Fig. (4.16b) shows that decreasing the EB: O_2 ratio to 1:0.3 and to 1: 0.13 does not result in a significant deactivation or decrease in the conversion rate, which is different to what was seen on the unpromoted catalyst (Fig. (4.7)). The initial rate can be regained after increasing the EB: O_2 ratio again. This shows that both oxygen and potassium play a very similar role in preventing the fast deactivation of the catalyst.

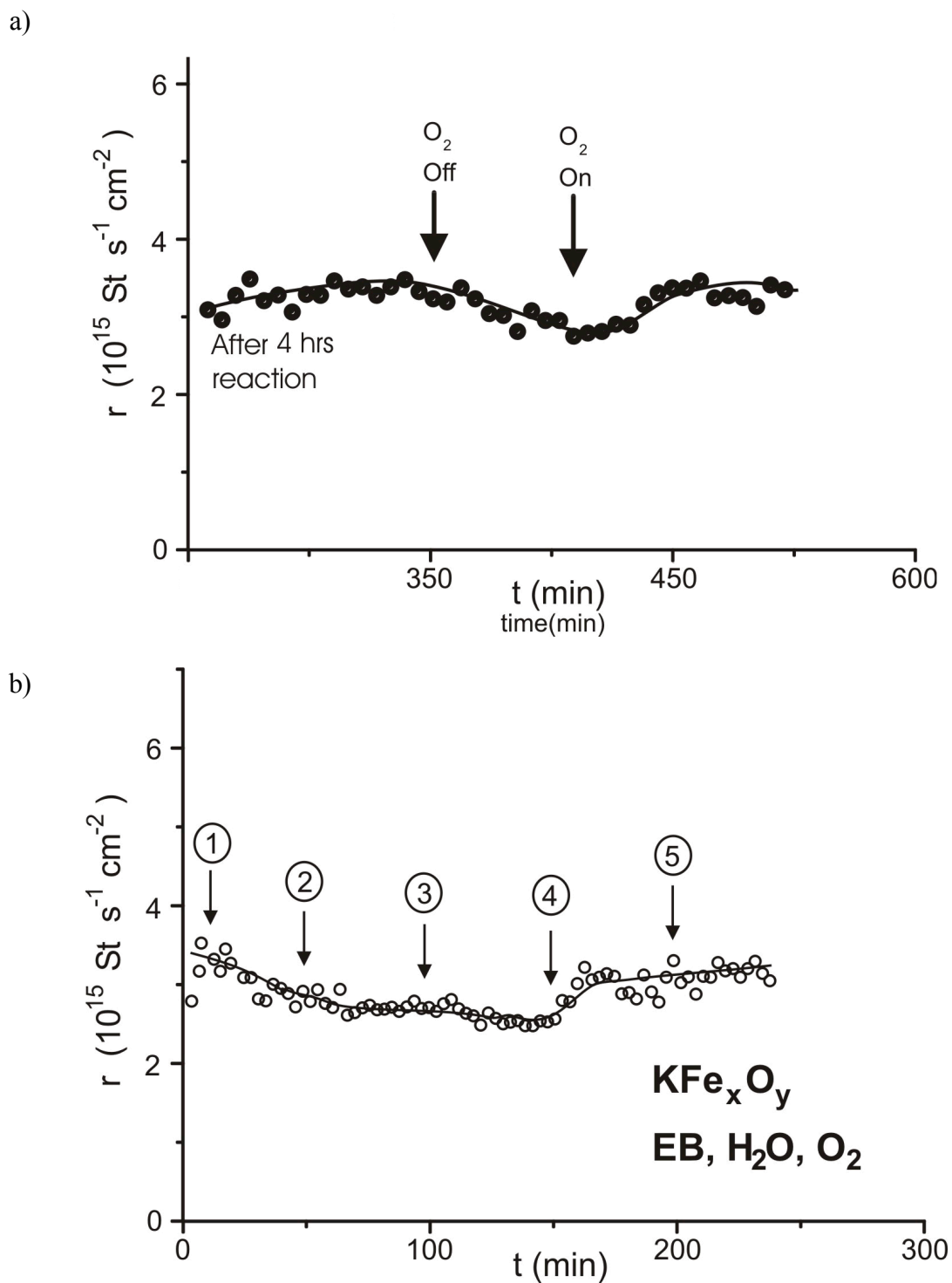


Fig. (4.16). a) Deactivation of the St conversion rate at 870 K, oxidative conditions, EB, H₂O and O₂ in the feed over a KFe_xO_y ($I_K/I_{Fe}=2.7$) after switching O₂ off and on. b) Conversion dependence of the St conversion rate at 870 K, oxidative conditions, EB, H₂O and O₂ in the feed, over KFe_xO_y ($I_K/I_{Fe}=2.7$), on EB/O₂ ratio, (1) 1:0.5, (2) 1:0.3, (3) 1:0.13 (4) 1:0.3 and (5) 1:0.5

4.3.8 Dehydrogenation reaction on α -Fe₂O₃ (0001) model catalyst in presence of

steam and oxygen at different temperature.

Fig.(4.17a) shows the St conversion rate over a promoted KFe_xO_y model catalyst with a ($I_K/I_{Fe} = 2.8$) under oxidative reaction conditions at different reaction temperatures. Oxygen was added in these experiments in order to keep the catalyst surface clean and prevent deactivation. The activation energy resulting from these measurements is presented in more detail in the discussion (chapter 5).

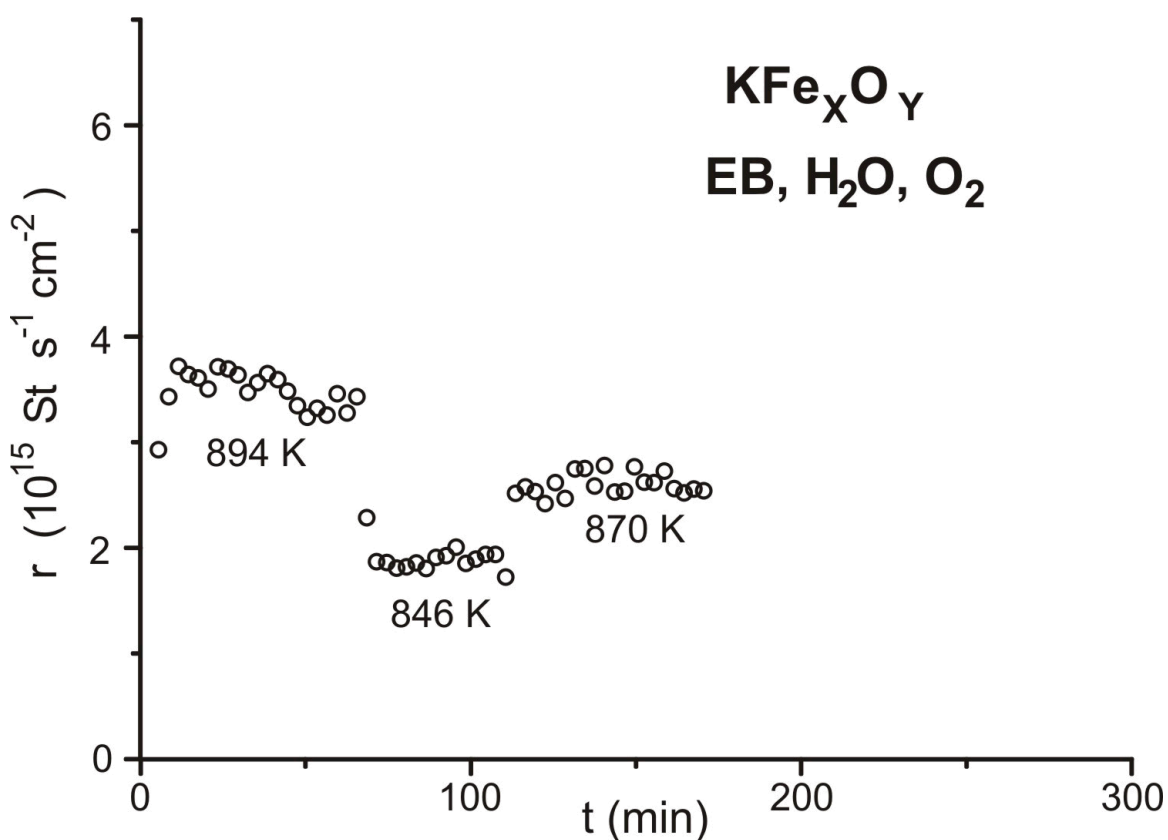


Fig. (4.17). The dependence of the St conversion rate at, oxidative conditions, EB, H_2O and O_2 in the feed, over a KFe_xO_y model catalyst ($I_K/I_{Fe}=2.8$) a) on reaction temperature.

4.4 Pressed hematite (Fe_2O_3) powder samples

4.4.1 Reaction on pressed powder pellets in fixed-bed reactor.

In cooperation with G. Kolios and A. Schüle, Institute für Chemische Verfahrenstechnik (ICVT), university of Stuttgart, a conversion measurement was performed over pressed pellets of hematite powder in a small fixed bed reactor under the reaction conditions of the technical process. The reaction was done with EB and water in the feed (Fig. (4.18) lower curve), and compared with a measurement where traces of oxygen were added to the feed (upper curve). In both cases the reaction rate drops initially, but in the presence of oxygen the rate stabilizes at a value about three times higher than without oxygen. A possible reason could be a stabilization of the hematite phase or burning of coke or both. Switching off the oxygen leads to a quick drop in the rate to the level of the experiment without oxygen. XRD analysis of the spent catalyst shows that it is completely reduced to magnetite, confirming the results observed on the model catalyst.

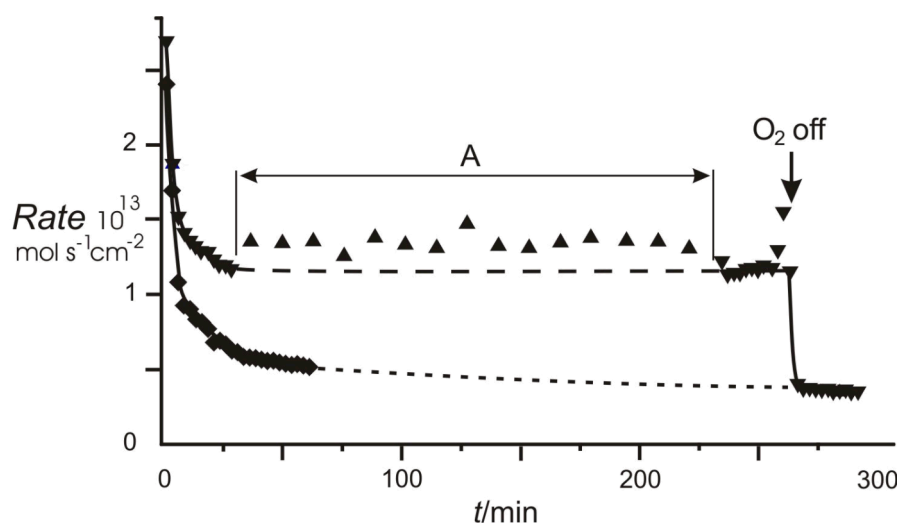


Fig. (4.18). Time dependence of the St rate production (molecules $s^{-1} cm^{-2}$ BET surface area) over pressed pellets of Fe_2O_3 powder in a fixed bed reactor. Reaction temperature 895 K, atmospheric pressure, 1) $EB/H_2O=1:6$ lower curve. 2) $EB/H_2O/O_2=1:6:0.4$ upper curve. In region A the GC was switched from fast FID analysis to the combined FID-TCD method, This caused a shift in the baseline.

4.4.2 Reactions on pressed powder pellets in the micro-flow reactor.

In addition to the reaction experiments performed on the model catalyst, here we have studied the reaction behavior over pressed hematite powder samples in the micro flow reactor under the same reaction conditions (Table (3.1)) used for the model catalysts. While the model catalysts consists of closed thin films of iron oxide without diffusion or mass and energy transport limitations. These influences are expected to play a major role on the powder samples. Comparing results from reactions on both type of catalysts will give an idea if the diffusion and transport limitations on the powder catalyst have an influence on the catalyst performance. This will help to bridge the pressure and material gaps. As on the model catalyst, the influence of addition of oxygen on the deactivation behavior will be investigated.

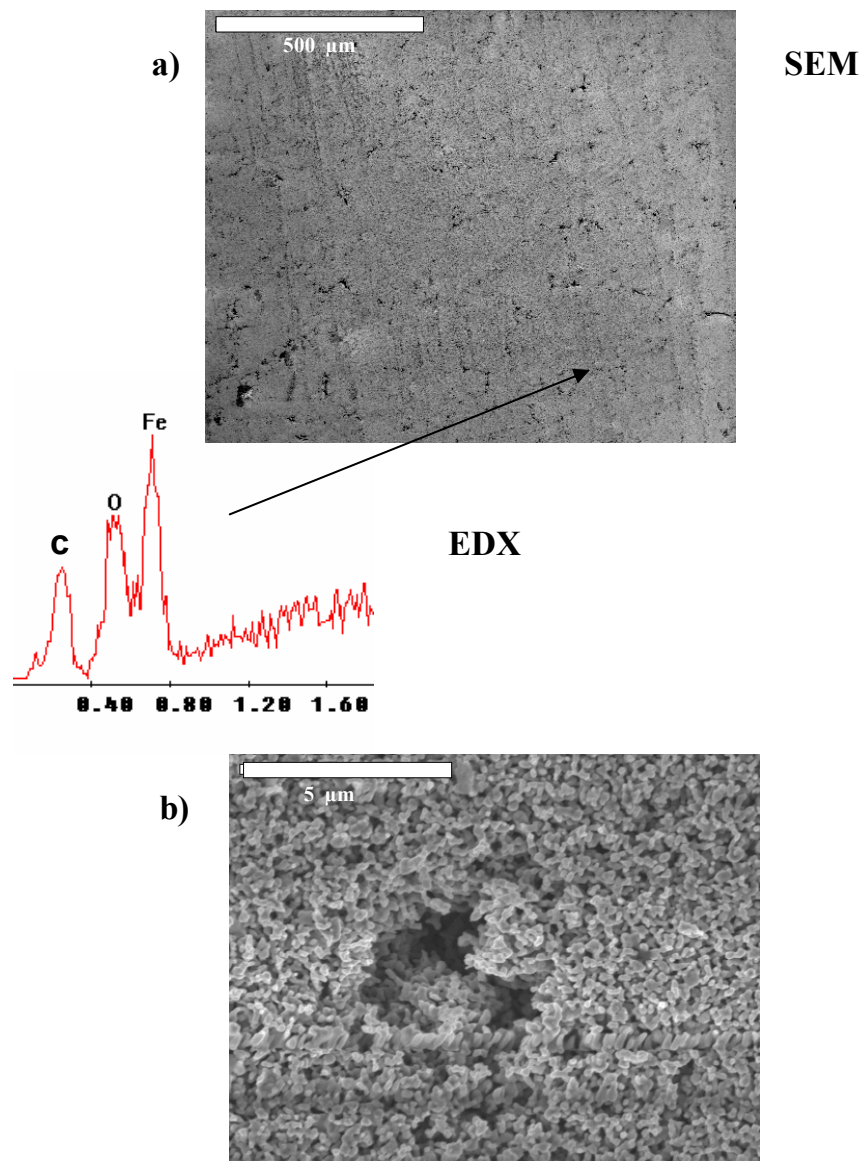
Since hematite is an electrical insulator, the characterization of the pressed powder samples by AES and LEED was not possible because of the charging. Ex-situ characterization by SEM-EDX was used for characterizing the chemical composition, particles shape and size of the samples before and after reaction.

Fig. (4.19a,b) shows SEM images of the fresh unused sample with different magnification. Fig. (4.19a) with a 500 μm magnification bar show that these samples contain only one type of round particles with size of a bout 0.3 μm . This type of round particles is a result of the grinding and pressing procedure of the powder sample. The SEM image of a higher magnification with a 5 μm bar (Fig. (4.19b) shows the particles more clearly. EDX shows mainly the signals from iron, oxygen and carbon which indicates that the particles consist of pure iron oxide, but they are not clean. Carbon is mainly concentrated in some areas as shown in Fig (4.19c,d).

The presence of these carbon materials could explain samples without pretreatment in our micro-flow reactor are almost inactive. After 2 cycles of cleaning, (heating for 20

min, in 10^{-1} mbar oxygen at 1000 K), the activity on these samples was considerably higher.

After the cleaning treatment, the SEM images show no significant change in the particle shape or size. EDX shows that the samples are almost free of carbon



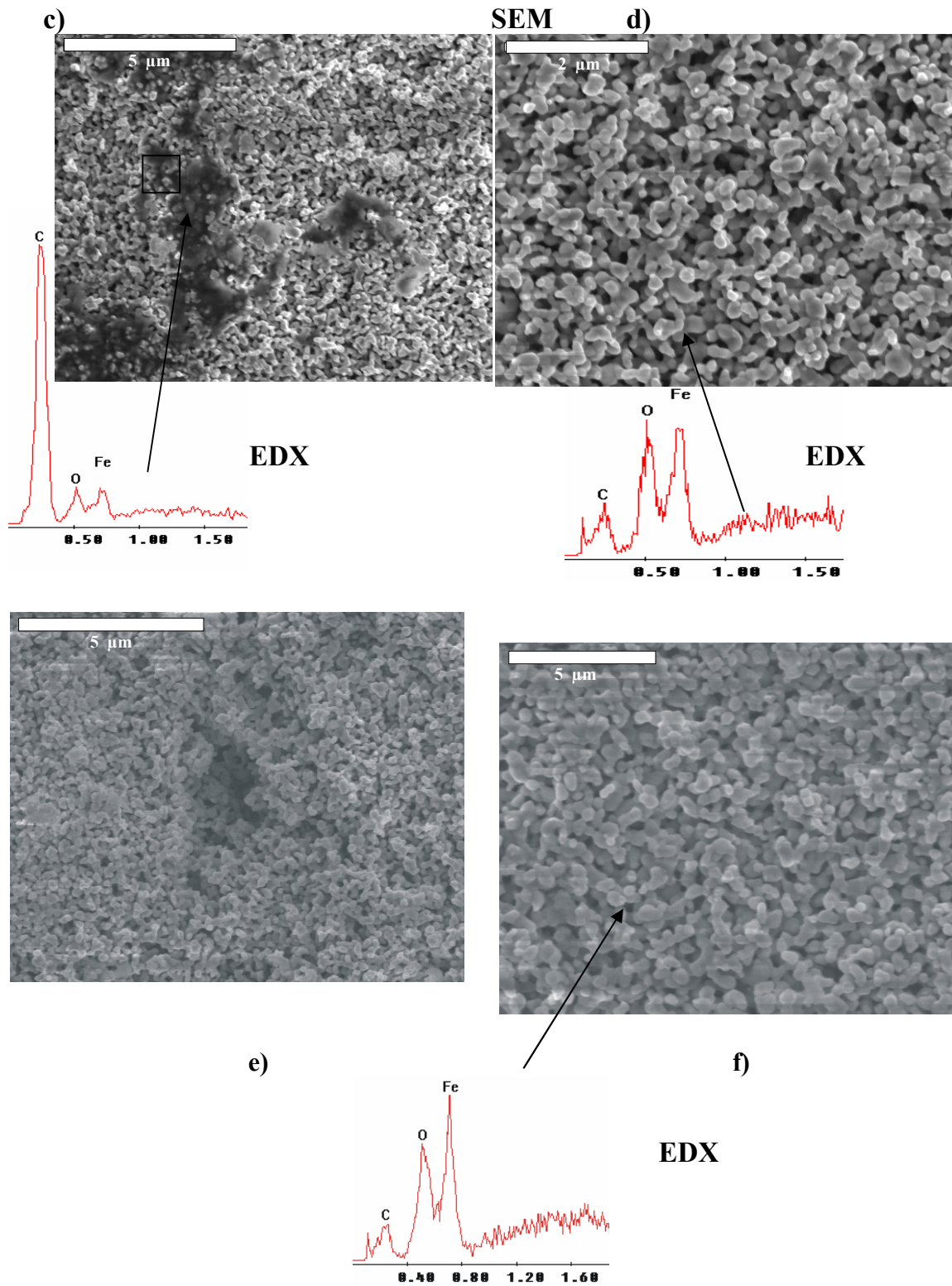


Fig. (4.19). SEM-EDX of the pressed hematite powder of unused samples (a) and (b). (c) and (d) carbon contaminated part. (e) and (f) after cleaning for 30 min in oxygen

4.4.2.1 Reaction in the presence of steam and EB in the feed (normal conditions).

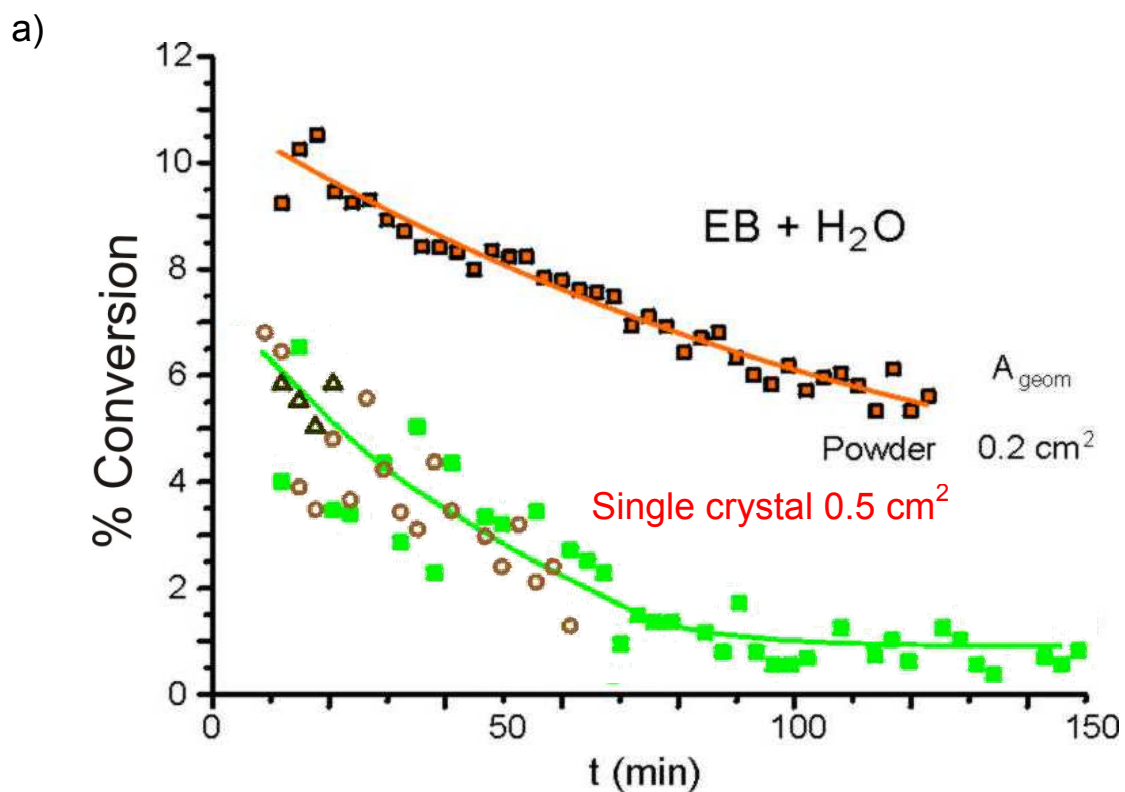
Fig. (4.20a) shows the St conversion over the pressed powder pellet used in the micro flow reactor after cleaning for 30 min at ~ 1000 K in 0.1 mbar oxygen. The reaction was done under normal conditions (Table (3.1)) as used for the model catalysts. Instead of the conversion rate, the conversion yield is given here since ordinate the conversion rate with respect to the BET surface area ($2.8 \text{ m}^2/\text{g}$) of the powder samples will not scale at all with the conversion rates on the model catalysts. The pressed powder samples show a high starting conversion, then deactivate relatively slowly with time on stream. The pressed powder samples show a 5 times higher conversion with respect to the accessible geometrical surface area (0.2 cm^2). Obviously, the accessible surface area on the powder samples is higher. However, since conversion does not scale with the BET area, this indicates that most of the inner surface is not accessible or shows only slow gas exchange. The deactivation rate is slower than on the model catalyst.

After reaction the sample was taken out of the reactor for post reaction characterization. The sample surface was red (i.e. still Fe_2O_3) and the back was black. The sample was broken into two halves, which showed that the sample is also black from inside and the red area was only a very thin layer on the surface. Part of the sample was ground for characterization with XRD, which showed that essentially the whole sample is reduced to magnetite (Fe_3O_4) as shown in Fig. (4.20b).

Characterization with SEM-EDX for the unground part of the sample showed that the red layer on the surface was very thin, and the rest of the sample was black. The composition difference between Fe_2O_3 and Fe_3O_4 is too small to be identified by SEM-EDX Fig. (4.21a,b). The SEM images Fig. (4.22a, b) showed also that the particle size distribution is changed in comparison to the fresh sample. In addition,

smaller particles $\sim 0.1 \mu\text{m}$ in size are formed, which maybe due to the breaking of the particles by the degradation process which occurred during reduction of the Fe_2O_3 to Fe_3O_4 under these reaction conditions. EDX showed that the particles are covered by some carbon deposits Fig. (4.22a, b).

There were also carbon deposits on the surface of these particles forming carbon cluster islands Fig. (4.23, 4.24). The sensitivity of the SEM can not tell if the particles between carbon clusters also are covered completely by a closed thin film of carbon or if carbon is restricted to the cluster islands.



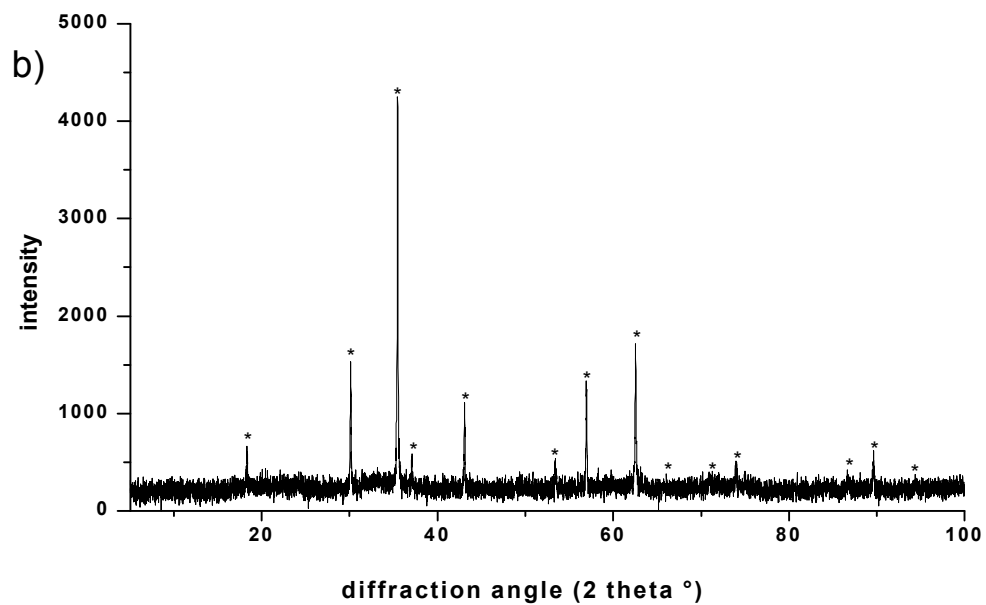


Fig. (4.20). a) St conversion over the pressed powder Fe₂O₃ pellets used in the micro-flow reactor at the same conditionconditions like the model catalyst of 870 K and EB and water in the feed. b) XRD spectrum of the powder sample after reaction. The asterisk mark the positions of Fe₃O₄ related diffraction peaks

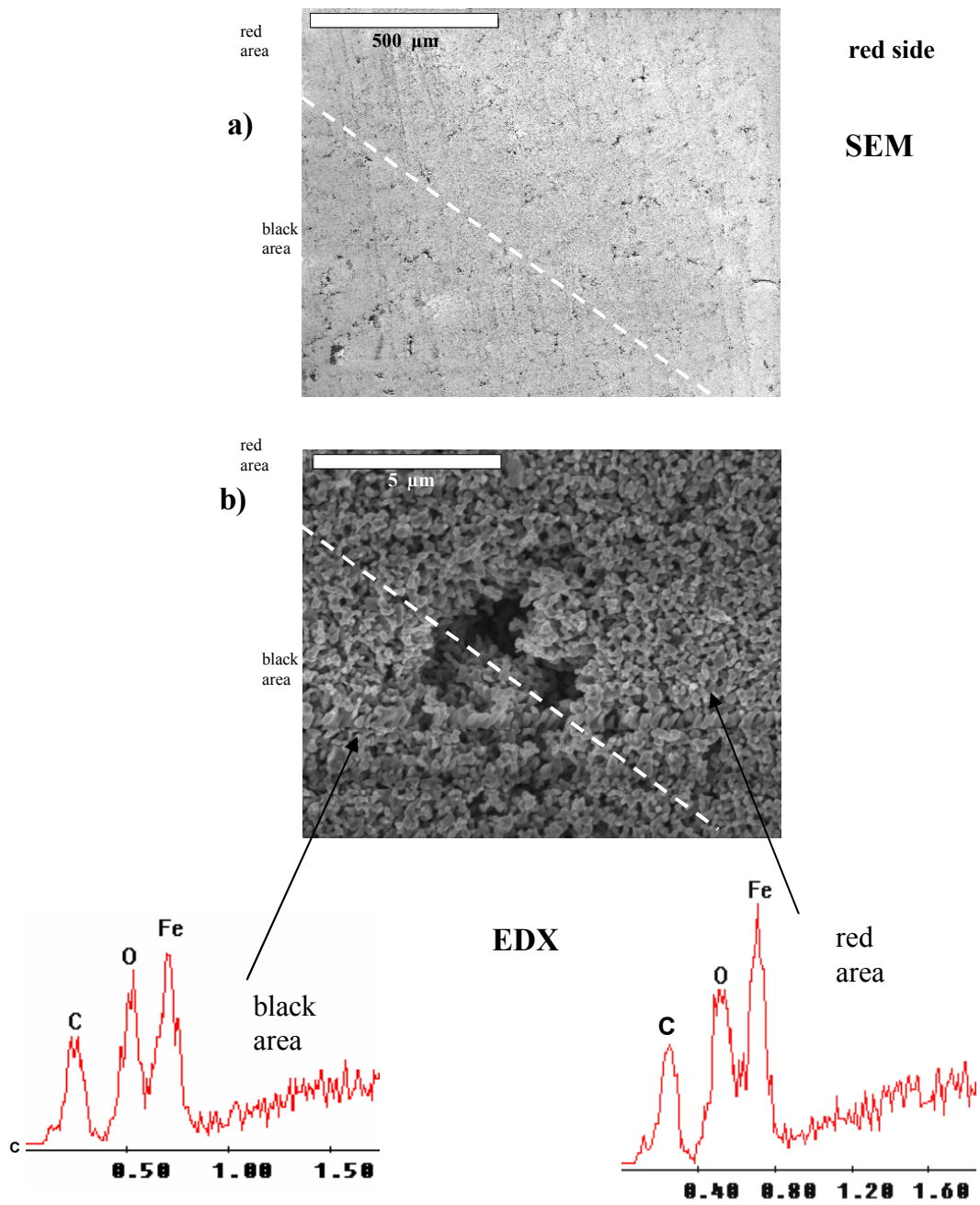


Fig. (4.21). SEM and EDX of the powder sample after reaction with EB and H₂O in the feed. The dashed line separates the red from the black parts of the sample.

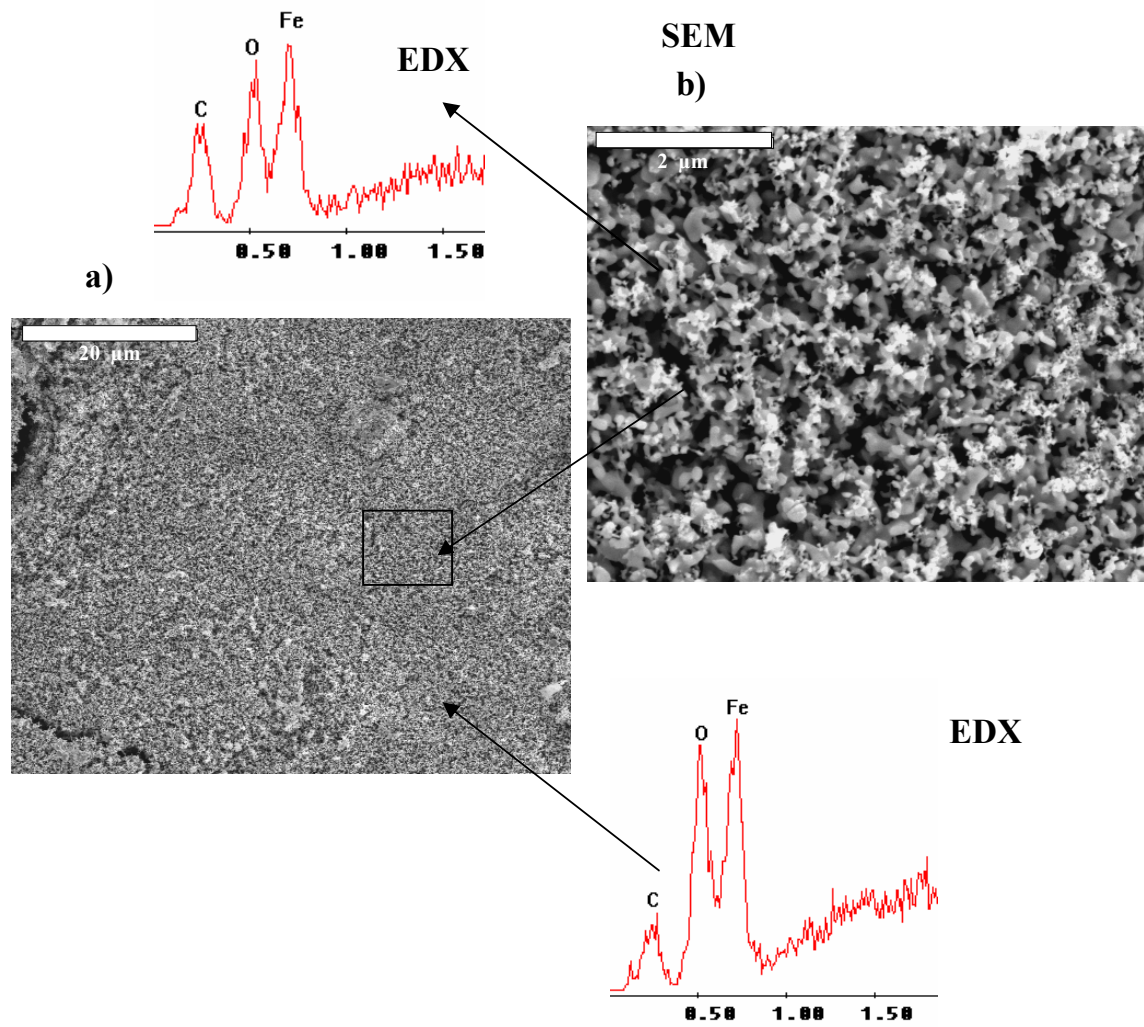


Fig. (4.22). SEM and EDX of the powder sample after reaction with EB and H₂O in the feed. The back was black (Fe₃O₄). The image (b) shows also small 0.1 μm particles.

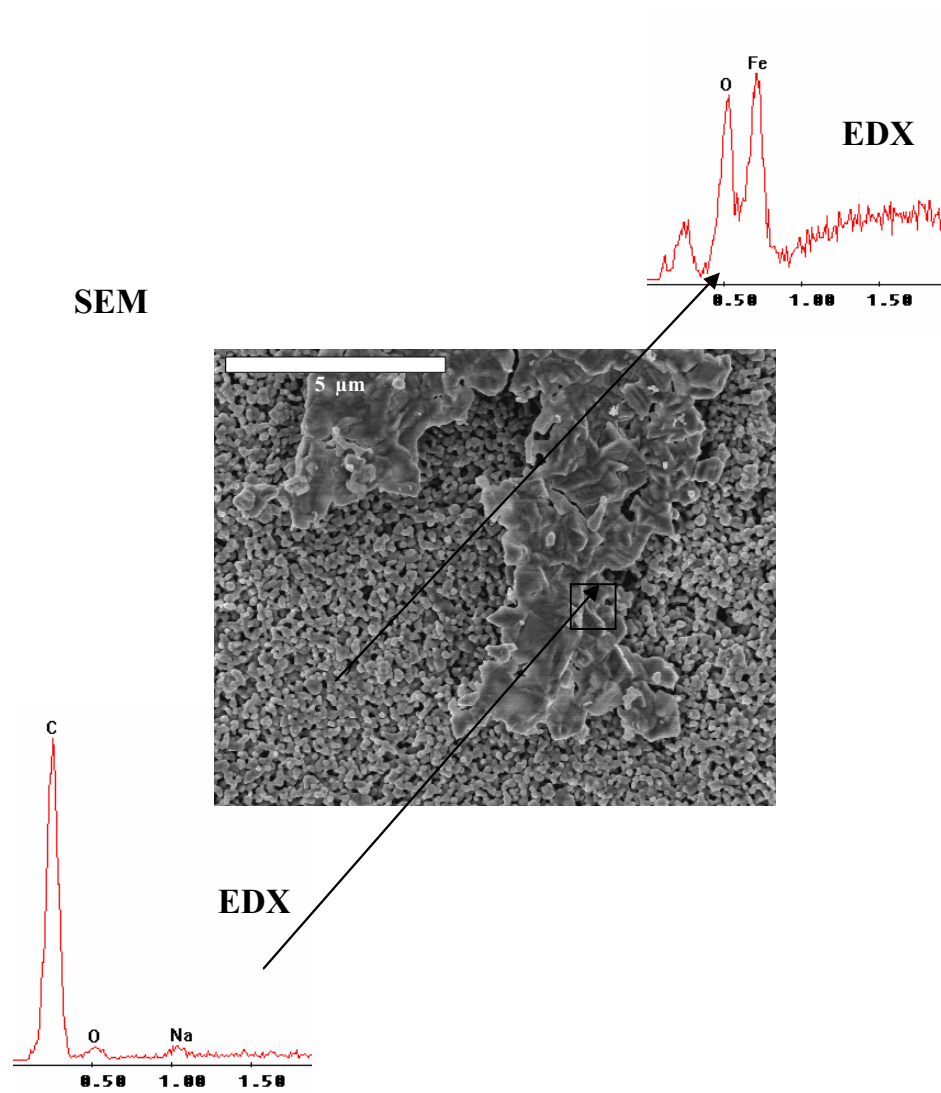


Fig. (4.23). SEM and EDX of the black part of the powder sample after reaction with EB and H₂O in the feed (normal conditions) showing clearly the carbon deposits after reaction.

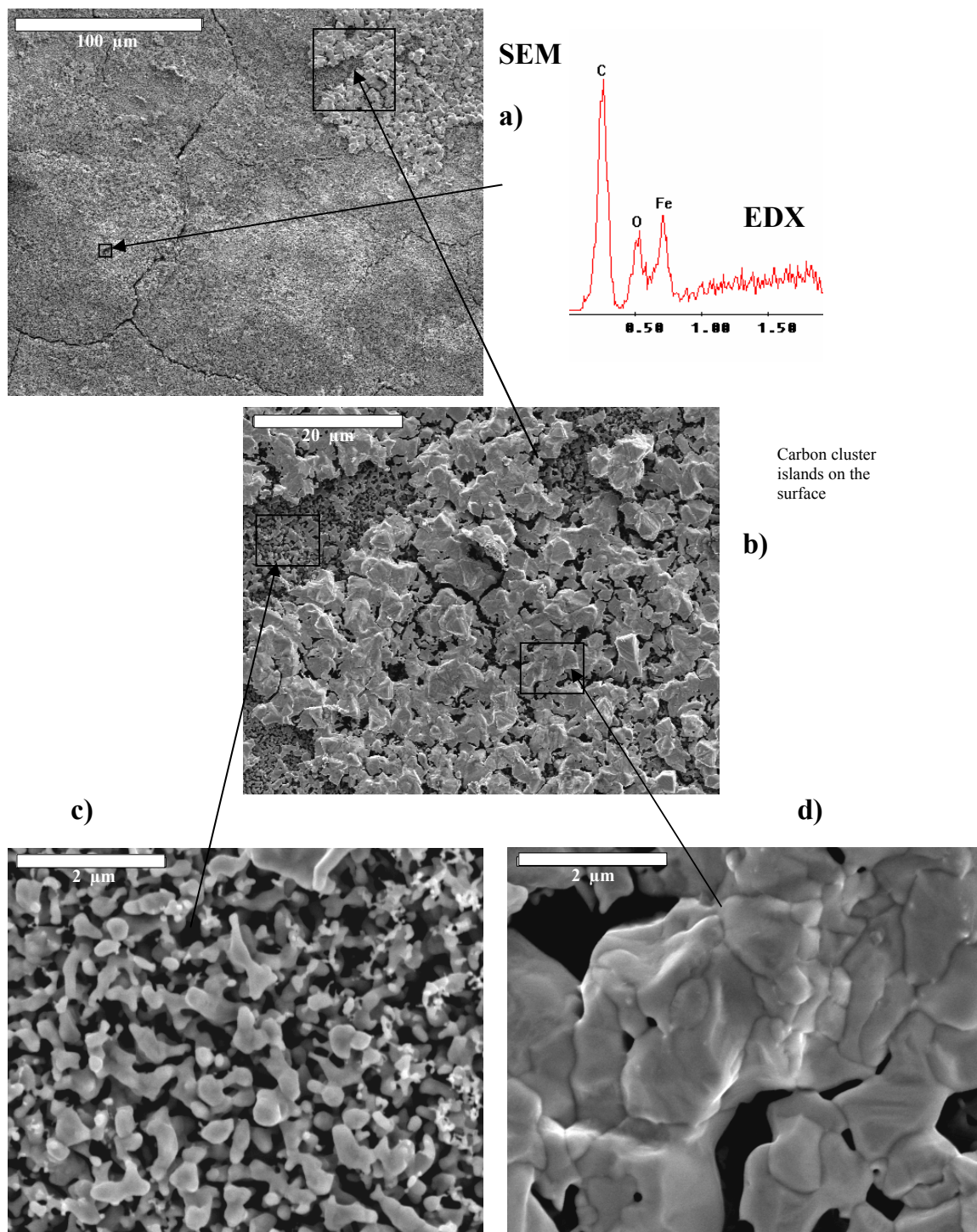


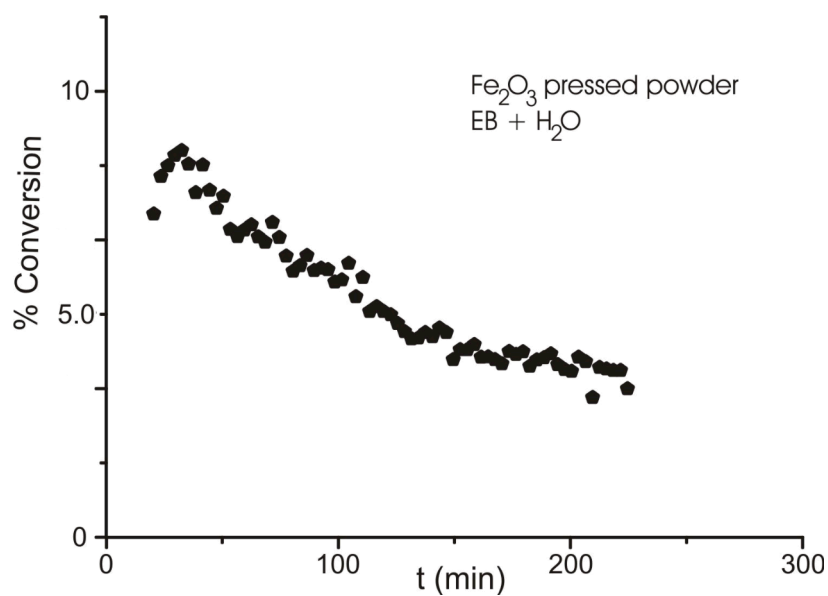
Fig. (4.24). SEM and EDX of the black part of the powder sample after reaction with EB and H₂O in the feed (normal conditions).

4.4.2.2 Reaction in the presence of EB, water and oxygen in the feed (oxidative conditions).

Fig. (4.25a) show the St conversion over the powder sample under normal conditions (Table (3.1)) on a new pressed powder sample. The activity is not high as with the sample in Fig. (4.20a) but the deactivation behavior is the same. After 4 hrs on stream, the reaction was stopped and the sample was taken out of the reactor. The sample was completely black and it was found to be magnetic (Fe_3O_4) using a rough test with a permanent magnet (explained in the experimental chapter). The sample was returned back to the reactor and was reoxidized using same conditions used in the cleaning procedure of the fresh samples. The reaction was continued on the sample but with the presence of oxygen in the feed (oxidative conditions (table (3.1))). Fig. (4.25b) shows that the St conversion is high and almost constant. So admitting oxygen led to the stabilization of a higher yield St conversion which is in a agreement to what was seen on the model catalyst. After reaction the sample was taken out from the reactor the sample was completely red with some grey-black spots at the back of the sample.

The sample was characterized using XRD and SEM-EDX. The XRD showed that the sample was still mainly hematite, As on the model catalyst the reduction to magnetite (Fe_3O_4) was prevented. The SEM images Figs. (4.26,4.27) show that there are tow types of particles, round ones like in the fresh sample Fig. (4.27b) and plane rectangular particles up to 1 μm in length and width. These particles are not only on the surface but they are also below the surface .The latter see to form also in cavities Fig. (4.27d). This morphology change may be due to recrystalization of the particles by the reduction and reoxidation during the reaction. At the back of the sample where the grey-black spots were seen tow types of particles are seen, one like on the fresh sample and other ones with a size up to 2 μm Fig. (4.28).

a)



b)

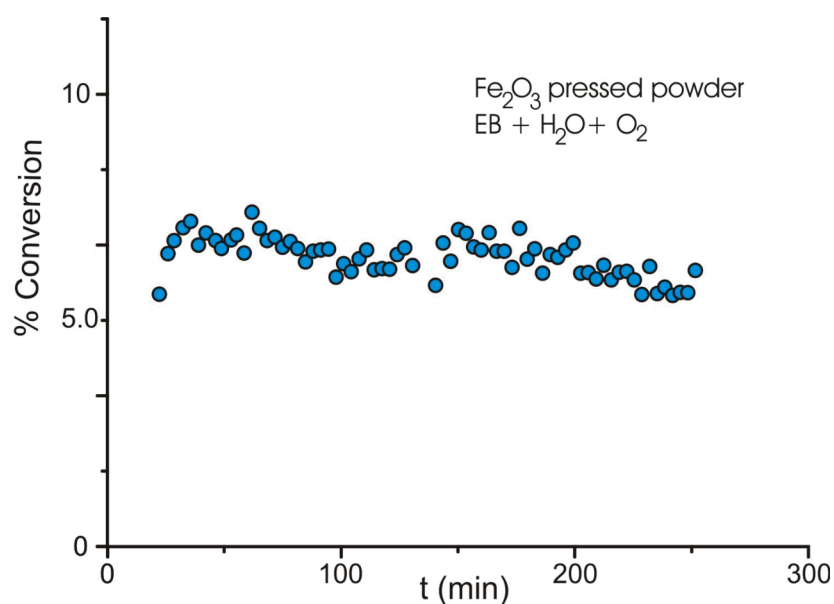


Fig. (4.25). a) St conversion over the pressed Fe₂O₃ powder samples used in the micro-flow reactor under the same conditions for the model catalyst 870 K and EB and water in the feed, normal conditions. b) In the presence of oxygen in the feed, oxidative conditions.

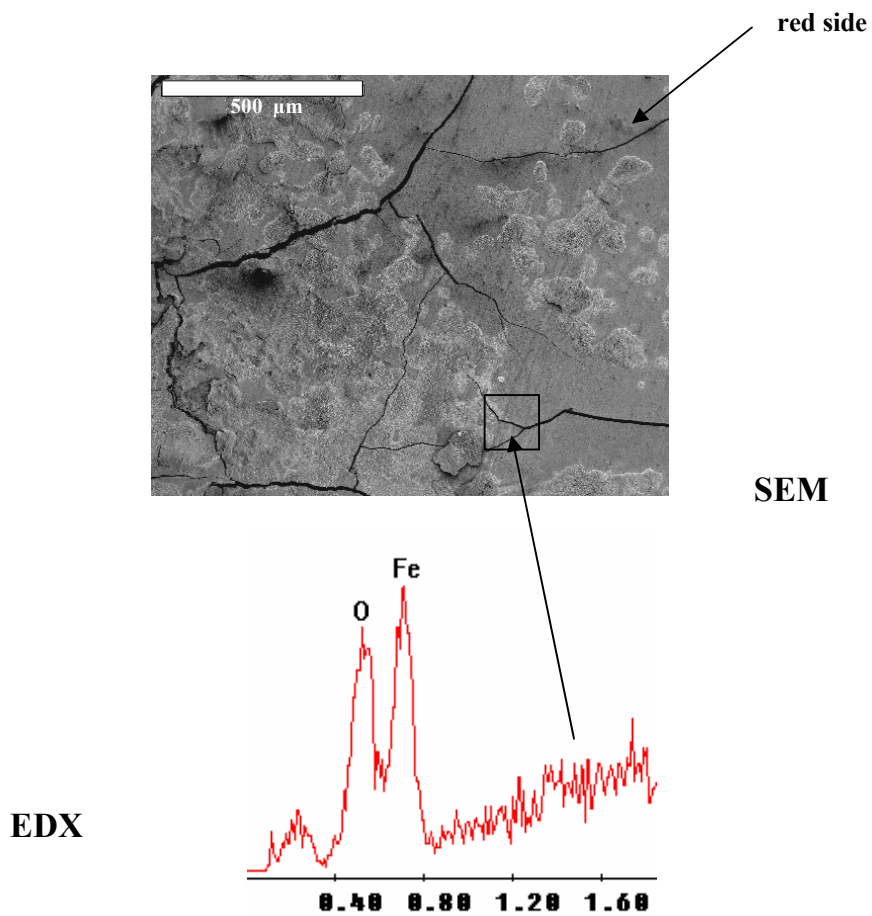


Fig. (4.26). SEM and EDX of the powder sample after reaction with EB, H₂O and O₂ in the feed (oxidative conditions). The sample was red (Fe₂O₃) and the EDX spectra shows that the surface is almost clean from the carbon deposits.

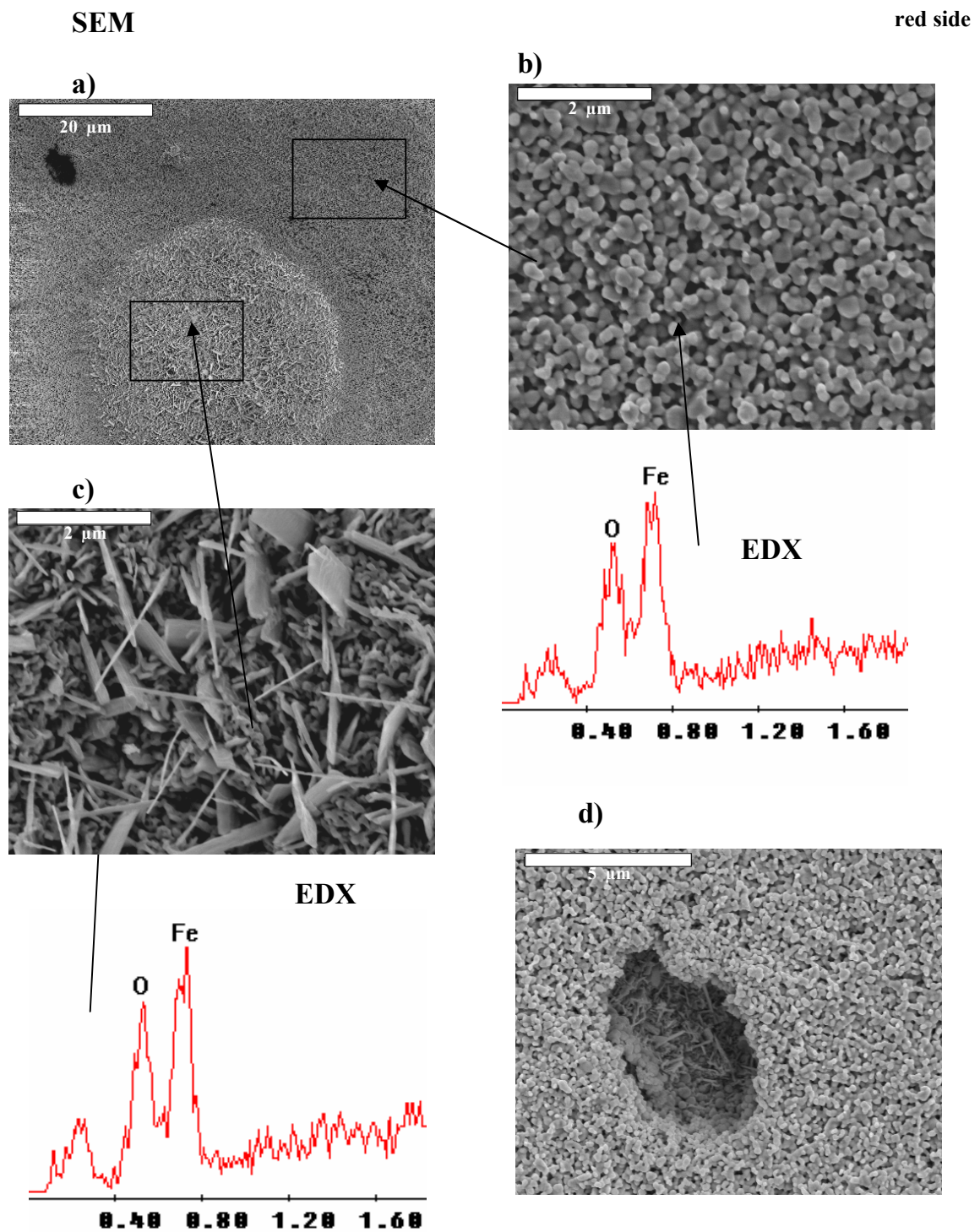


Fig. (4.27). SEM and EDX of the powder sample after reaction with EB, H₂O and O₂ in the feed (oxidative conditions).

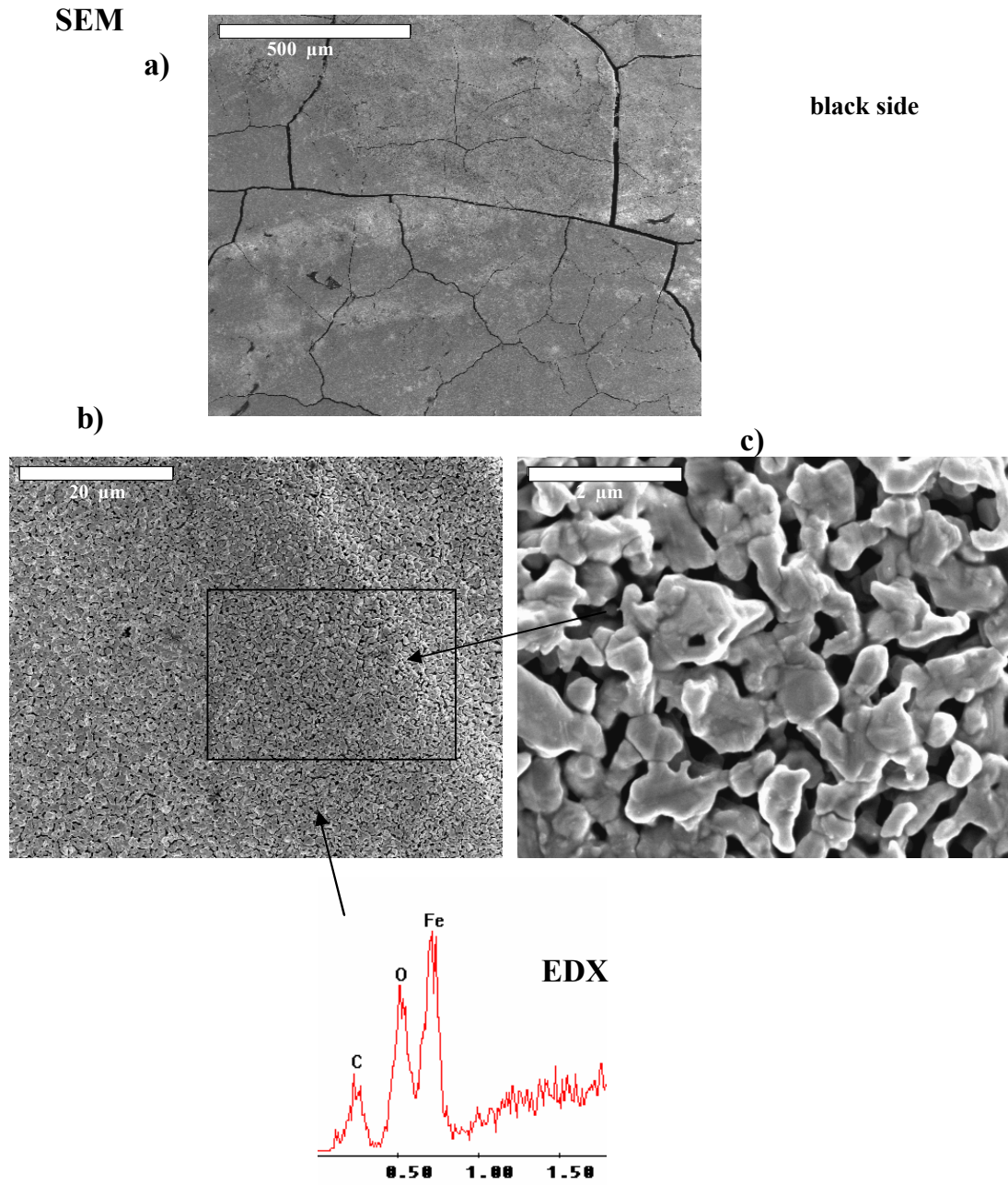


Fig. (4.28). SEM and EDX of the powder sample after reaction with EB and H₂O in the feed. oxidative conditions.

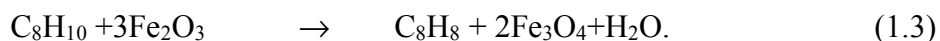
Chapter-5

Discussion

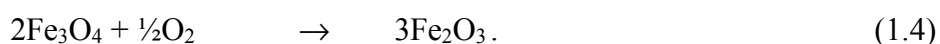
5. Discussion

5.1 Unpromoted model catalysts

The reactivity measurements in connection with pre- and post-reaction characterization on the unpromoted Fe₂O₃ catalyst showed that the clean catalyst initial conversion rate is high and that deactivation is due mainly to reduction of Fe₂O₃ to Fe₃O₄ and to coking. The high initial activity observed is related to the clean Fe₂O₃ surface while the activity of clean Fe₃O₄ is lower. Especially since the addition of oxygen stabilizes the high initial activity, it is important to check if it is the oxygen liberated during substrate reduction (i.e. Fe₂O₃ to Fe₃O₄) which is responsible for the high starting rate on Fe₂O₃. The lattice oxygen could be consumed by the hydrogen produced from the EB dehydrogenation to form water according to the equation (1.3)



This would be a simple stoichiometric reaction which could be prevented by admission of O₂



Since our starting films are about 10-20 nm thick and a simple estimation yields the amount of O₂ liberated when the whole film is reduced to Fe₃O₄. Comparison with the amount of St formed (which equals the amount of formed H₂) within the high rate region in Fig. (4.1) (~15 min with rate of 4 x 10¹⁵ molecules s⁻¹ cm⁻²) shows that St production is at least by a factor of 700 higher. The dehydrogenation reaction of EB to St over clean Fe₂O₃ is thus essentially catalytic. This means that it could be a unimolecular reaction, where St is produced on the sites where EB dehydrogenates on. i.e. these sites are occupied by EB and St which agrees with what Hirano found

[10,11]. The stoichiometric reaction (reduction process (eq.1.3)) may be a side reaction.

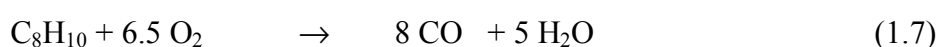
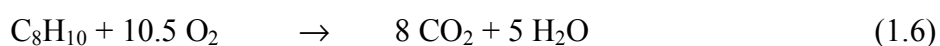
The equilibrium thermodynamics of the Fe-O₂-H₂-H₂O system has been investigated experimentally by Muan [61]. Calculations based on thermodynamic data confirm the results [89]. For the reaction temperature of 870 K, Fe₂O₃ is reduced in presence of H₂. Without H₂O, this proceeds to metallic Fe⁰ while the presence of H₂O limits reduction to Fe₃O₄. The hydrogen produced during EB dehydrogenation is thus responsible for the observed reduction effects. The role of H₂O is not only to balance coke formation by the coal gasification reaction but also to limit reduction beyond the magnetite (Fe₃O₄) phase [11]

The thermodynamic considerations showed also that hematite (Fe₂O₃) reduction can be prevented by addition of oxygen. The necessary minimum amount corresponds almost to that necessary for the stoichiometric water formation reaction

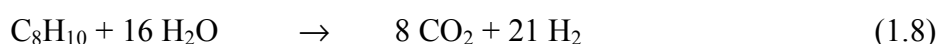


The high conversion rate observed with O₂ in the feed Fig. (4.6) corresponds to a conversion of about 10% of the introduced EB. The formed $p(\text{H}_2)$ would thus correspond to 10% of $p(\text{EB})$. The necessary oxygen for its oxidation would be 5% of $p(\text{EB})$ and a molar ratio above O₂:EB=0.05 should be sufficient to prevent Fe₂O₃ reduction. If thermodynamic equilibrium would be established, the dashed step curve in Fig. (4.7b) would be expected for the dependence of the steady state rate on the O₂:EB ratio. The measured steady state rates show a reduction with respect to the standard oxygen concentration O₂:EB=0.5 by about 10% for O₂:EB=0.25 and by 25% for O₂:EB=0.15.

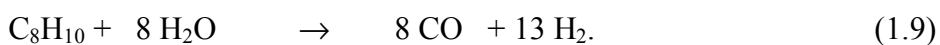
There may be two reasons for the rate decay before reaching the theoretical limit of $O_2:EB=0.05$: Thermodynamic equilibrium may not to be established within the reactor or a part of the oxygen may be consumed for the oxidation of coke. Each EB molecule which is converted into partially dehydrogenated species or graphitic coke and hydrogen, needs 10.5 or 6.5 O_2 molecules for oxidation of all formed products into H_2O and CO_2 or CO , respectively (total oxidation):



In the presented experiments, about 5% of the introduced EB did not show up as aromatics in the GC measurements. This represents the upper limit of EB consumed for coking and a flow ratio $O_2:EB=0.525$ [reaction (1.6)] or 0.325 [reaction (1.7)] would be necessary to oxidize it continuously. One might think that less oxygen may be necessary since the coke is also partially removed by the water in the feed by the coal gasification reaction. Including the hydrogen formed during dehydrogenation in the coking process, this leads to the sum reaction



or



In order to prevent catalyst reduction, it is necessary to oxidize all the produced H_2 . The necessary amounts of O_2 correspond to $O_2:EB=0.525$ and 0.325, respectively, for equations (1.8) and (1.9) and are, of course, the same as without influence of water. It turns thus out that oxidation of coke and of the hydrogen liberated during coking dominate the necessary amount of oxygen to be added. The estimation shows further

that the experimentally applied oxygen flow for maximum rate (EB:O₂=1:0.5) is near to the optimal level.

The observed reduction of the hematite to magnetite agrees with observations on technical catalysts [12,22,14,86]. However, the high initial rate associated with clean hematite was not observed before. Obviously it was hidden in the start-up and equilibration period, since in most studies found in literature the measurements were done after activating the catalyst under the educts stream for a few hours [10,12,15]. It is therefore likely that only the fully deactivated state was observed in the investigations on technical catalysts. An exception is a recent measurement (Stuttgart experiment) on pressed Fe₂O₃ powder pellets under technical conditions (1 bar, pure EB + H₂O atmosphere, EB:H₂O=1:6) Fig. (4.18), where the initial high conversion rate decreased within the first minutes on stream by a factor of ~8-10 [90]. Upon addition of oxygen (EB:H₂O:O₂=1:6:0.4), the steady state conversion did not rise to the initial value but could at least be enhanced by a factor of three. The concentration of O₂ was obviously not sufficient for full prevention of reduction and coking. The conversion rate (referred to the BET surface) on the powder catalyst was about two orders of magnitude lower than on the model catalyst which indicates that it is limited by mass and energy transport on the powder catalyst.

In low and medium pressure experiments $p(\text{EB})+p(\text{H}_2\text{O}) = 3.5 \times 10^{-6}$ [86] to 0.6 mbar [85] there was clear evidence that defective Fe₂O₃ surfaces are catalytically more active than well ordered ones. In the high pressure experiments presented here, [$p(\text{EB})+p(\text{H}_2\text{O}) = 36$ mbar], no indications for a defect dependent initial activity was observed but post-reaction analysis showed always that disorder had formed during reaction as seen in the STM image in Fig. (4.2) where the surface is quite rough after reaction and also as deduced from the high background and the diffuse spots in the

LEED patterns. Formation of disorder is plausible because of the observed reduction which implies out-diffusion of oxygen and nucleation of magnetite with its different crystal structure. While at low and medium pressures the formation of defects is slow enough so that the influence of initial surface disorder is clearly visible, the more violent reaction conditions at high pressure may accelerate defect formation so that it has happened within the first minutes and may at most influence the first GC data point after gas admission. The importance of defects for the mechanism of the catalytic reaction could thus only be deduced from low pressure experiments.

The final activity after deactivation is definitely not zero. There is strong evidence that it can be ascribed to carbonaceous deposits. It is well known that certain forms of carbon are active catalysts in oxidative dehydrogenation of EB (1.6 chapter 1) which has changed the idea that carbon deposits are always a deactivation source of the catalysts [49,50]. If no oxygen is added and after reduction of the substrate, the only source of oxygen is the water which may supply oxygen according to the dissociation equilibrium at the reaction temperature, a necessary condition for coal gasification. Post-reaction Auger analysis also revealed oxygen at the surface in this case which could indicate that quinoline (C=O) groups on carbon could act as the active sites in the deactivated state, as presented in oxidative dehydrogenation on carbon [51]. When no water is added, even this source of oxygen is lacking. Consequently, no oxygen was visible in AES. However, the final activity in Figs. (4.1, 4.3 and 4.4) was almost the same $\sim 0.5 \times 10^{15}$ molecules $s^{-1} cm^{-2}$, independent of the presence or absence of water. The mechanism over the deactivated catalyst is thus not yet clear.

Model catalyst film structure changes under reaction conditions changes and it is not any more like the starting surface. The post reaction characterization and the oxygen on-off experiments Fig. (4.8a and b), show that the surface becomes rougher. This is

probably the reason why deactivation after the oxygen is switched off is faster than when starting with the clean Fe_2O_3 without oxygen from the beginning. The roughness results from the re-crystallization caused by dynamic reduction-oxidation process in the film and increases the surface area which improves the solid gas-phase exchange. This may also explain the fast deactivation observed, after switching off the oxygen in the experiments done over the pressed powder pellets in the fixed bed reactor Fig. (4.18). The interesting result in the fixed bed reactor experiment was that the τ_{de} was smaller under reaction in EB and H_2O , without oxygen (normal conditions) but larger after switching the oxygen off after reaction under oxidative condition. This direct drop of the rate after switching the oxygen off could be due to the increase in the roughness or morphology of the catalyst as the results on the model catalyst under the similar conditions showed.

5.2 K-promoted model catalysts

Fig. (4.10). showed clearly that promoting the iron oxide with potassium, lead to a dramatic change in the deactivation behaviour of the catalyst. Also conversion measurements which were run over several model catalysts with different initial potassium content, show that the potassium content have an effect on the initial activity and deactivation rate. Fig. (5.1) summarizes the dependence of the initial conversion rates r_{in} and of the time constant of deactivation t_{de} (assuming an exponential decay of the rates) on the K-content in terms of $\mathbf{I}_K/\mathbf{I}_{Fe}$. Also the initial rates for the unpromoted samples (Fe_2O_3 , Fe_3O_4 , Fe_2O_3 with O_2 added to the feed) are included. The initial rate decreases and the time constant for deactivation increases with the K-content. A simple explanation of this behaviour would be that K prevents catalyst deactivation by reduction and coking but at the same time reduces or blocks

active surface sites. For $I_K/I_{Fe} > 2.7$, the surface is increasingly covered by $KFeO_2$ [59,73]. The further decrease of the rate in this range suggests that $KFeO_2$ is not the catalytically active phase. However, its presence may be responsible for slow deactivation. The optimal compromise between high rate and slow deactivation may be the composition corresponding to the $K_xFe_{22}O_{34}(0001)-(2 \times 2)$ surface.

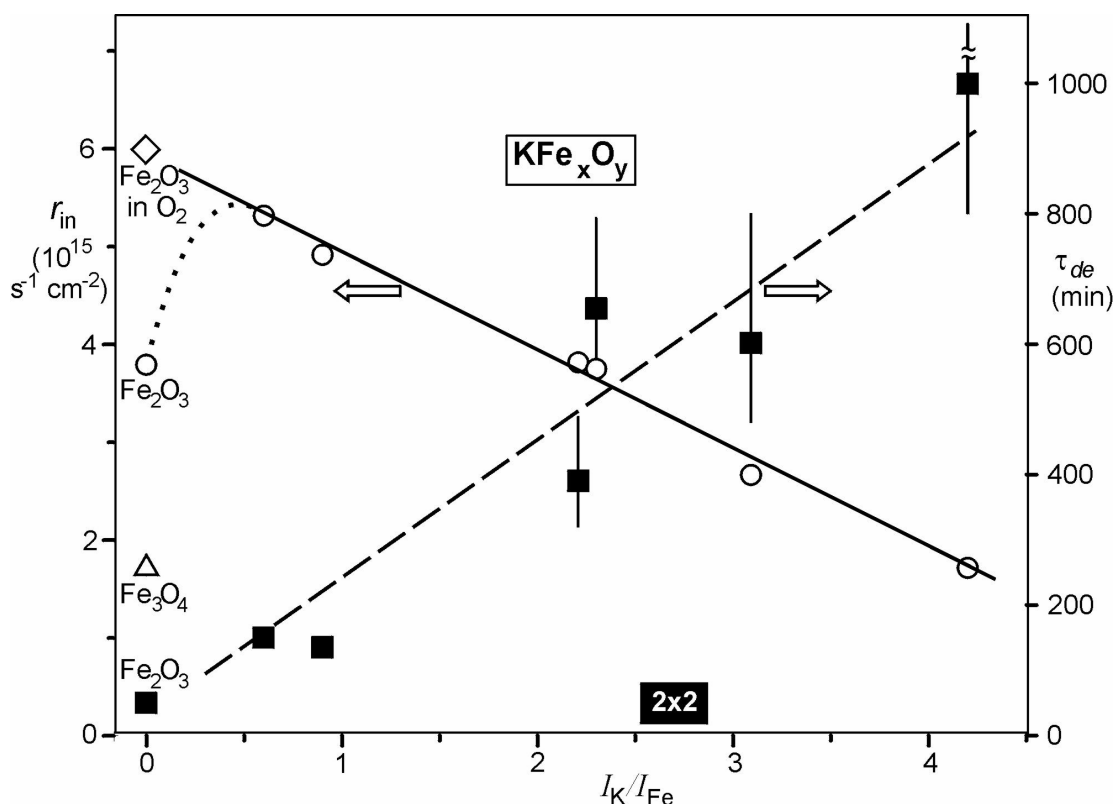


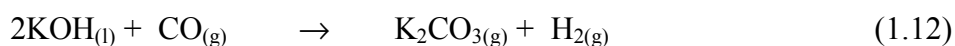
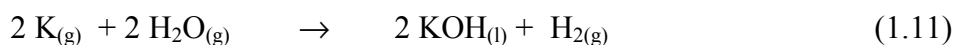
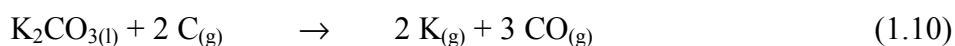
Fig. (5.1). Initial St conversion rate r_{in} and time constant for deactivation τ_{de} for samples with different initial K-content in terms of the Auger peak height ratio I_K/I_{Fe} . The composition where the ordered (2X2) structure is formed is indicated.

For low K-content, the initial rate in Fig. (4.11a) tends towards the rate of Fe_2O_3 with O_2 in the feed while the rate of Fe_2O_3 without O_2 is lower (dotted curve). We believe that this is caused by partial deactivation of Fe_2O_3 before the first data point of the rate curve (Fig. (4.1)) can be taken. It is plausible to assume that the topmost surface layer is partially reduced quite quickly so that the rate approaches that of Fe_3O_4 while addition of O_2 prevents this and preserves the clean unreduced surface.

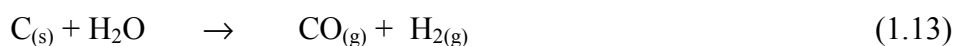
With oxygen in the feed, the reaction rate on the unpromoted Fig. (4.6) and on the promoted catalyst with low potassium content Fig. (4.14) are very similar concerning both magnitudes and the time dependence. It seems therefore feasible to use oxygen in the feed instead of promotion by potassium; this is confirmed by the weak dependence of the rate over the potassium promoted catalyst on the oxygen amount introduced.

The generally lower coke concentration on potassium promoted catalysts after reaction shows that, the potassium plays a role in catalyzing the removal of carbon deposits. In literature [20,21] K_2CO_3 is suggested to be the active sites for the coke gasification.

The gasification of coke goes through a series of sequence reactions which are.



The net equation from these reaction is the removal of carbon:



The formation of K_2CO_3 during reaction has another effect, which is preventing the fast depletion of potassium mainly as KOH, which has a high partial vapor pressure (~ 0.1 mbar) at reaction temperature (870 K), since potassium is involved in the cycle of carbon removal explained above. This could explain the moderate loss of potassium observed in our experiments under normal reaction conditions, and the strong loss of potassium under steaming conditions where equation (1.11) becomes the dominant process.

Another function of potassium is to prevent or to retard the reduction of the iron oxide partially by polarizing the Fe-O bond. It was found that in oxide catalysts the electron-donating effect of the alkali metal ions increases the reactivity of the oxygen in the M=O bond (M= transition metal ion in the catalyst) [93].

All results point towards the direction that potassium prevents coking and catalyst reduction but does not directly take part in the catalytic reaction. Since the initial activity on unpromoted Fe₂O₃ and on optimally promoted films (I_K/I_{Fe} between 2.2 and 3) is quite similar Fig. (5.1), it is suggestive to assume that the active sites and mechanisms are the same and are related to a stable Fe³⁺. This is supported by our activation energy value which has been calculated from the reaction experiments at different reaction temperature over both the unpromoted and promoted catalyst (Figs. (4.9, 4.17). The calculations were done by applying Arrhenius equation (1.14)

$$\ln(r) = \ln(A) - E_a/RT \quad (1.14)$$

where r is the rate coefficient, A is a constant, E_a is the activation energy, R is the universal gas constant (8.314 J mol⁻¹ K⁻¹) and K is temperature (in degrees Kelvin). Fig. (5.2) shows the plot ln(r) versus 1/T(K).. The activation energy was calculated from the linear slope of this plot and found to be ~ 92.1 and 88.7 KJ/mole for the unpromoted and potassium promoted catalyst respectively.

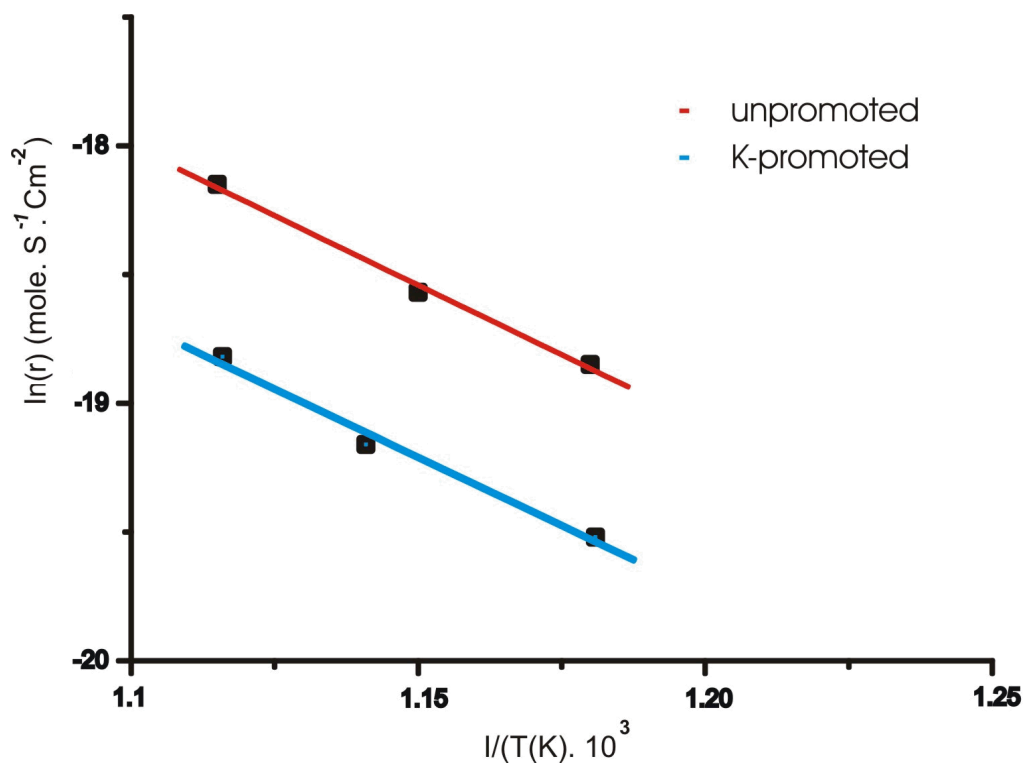


Fig. (5.2). Temperature dependence of the rate of styrene formation over the unpromoted (Fe_2O_3) and potassium promoted iron oxide (KFe_xO_y) model catalysts.

In literature, this was also been claimed to be found for technical and polycrystalline catalysts. The activation energy of the fresh catalyst was found to be lower than the used one [10,12,74]. But, in most cases (according to our knowledge now) the unpromoted catalyst was deactivated and thus not Fe_2O_3 and this could explain the wide range of activation energy (80-140 KJ/mole) found in literature [12,15,22]. Therefore our measurement is the only one which really proves that E_a on both catalysts are equal.

However, in the literature it is always mentioned that the activity of the unpromoted catalyst was an order of magnitude lower than for the promoted catalyst which has directed the development only towards the promoted catalyst. According to the model catalysis results reviewed here, this means that the unpromoted catalyst was most likely deactivated, i.e. reduced and coked [1,2].

Also the addition of oxygen does not change the initial activity dramatically. The mechanism of the main reaction path may therefore not either be influenced by the presence of oxygen. It is not oxidative in the sense that oxygen takes directly part in the catalytic reaction. It rather balances the effects of catalyst reduction by the hydrogen formed in the catalytic reaction and during coking, both being side reactions of the process and it oxidizes the deposited carbon.

The active site requires Fe^{3+} but the Fe^{3+} in Fe_3O_4 is obviously not equally active. It could be that a pure Fe^{3+} environment is necessary as present in Fe_2O_3 , KFeO_2 and formally also in $\text{K}_2\text{Fe}_{22}\text{O}_{34}$. An alternative explanation was discussed by Kuhrs et al. [88,64] on the basis of the binding energies of EB and St to the different model catalyst surfaces. Due to the existence of iron in the top layer of Fe_3O_4 , EB and even more St are bound strongly and may block the surface under reaction conditions while bonding to Fe_2O_3 and $\text{K}_x\text{Fe}_{22}\text{O}_{34}$ is much weaker and more similar for EB and St. In hematite, the first layer consists of oxygen, possibly hydroxylated [65] and in $\text{K-}\beta''$ -ferrite, it is most likely formed by K and O [59]. These layers separate the adsorbate from the Fe-layer below but the distance is small enough to let the adsorbate still feel the acidic character of the Fe^{3+} sites underneath. The interaction with Fe_2O_3 and $\text{K}_x\text{Fe}_{22}\text{O}_{34}$ is sufficient to bind the EB molecule long enough to the surface to enable dehydrogenation but neither EB nor St so strongly that they block the surface. This is an example for the old wisdom in catalysis that the bonding should be strong enough but not too strong.

Based on the observations that both the right adsorption strength and – at least on unpromoted Fe_2O_3 –defects are necessary for high conversion, a model for the catalytic cycle has been proposed [56] and is shown in Fig. (5.2). This model shows the role of defects in the reaction, but in case of reaction in presence of EB and water

without oxygen this model works on those parts of surface where are not reduced. Reduction does not occur in each step (4). It occurs in an independent side reaction which slowly decrease the concentration of active Fe_2O_3 , but if oxygen is in the feed the reoxidation could happen and the cycle is completed

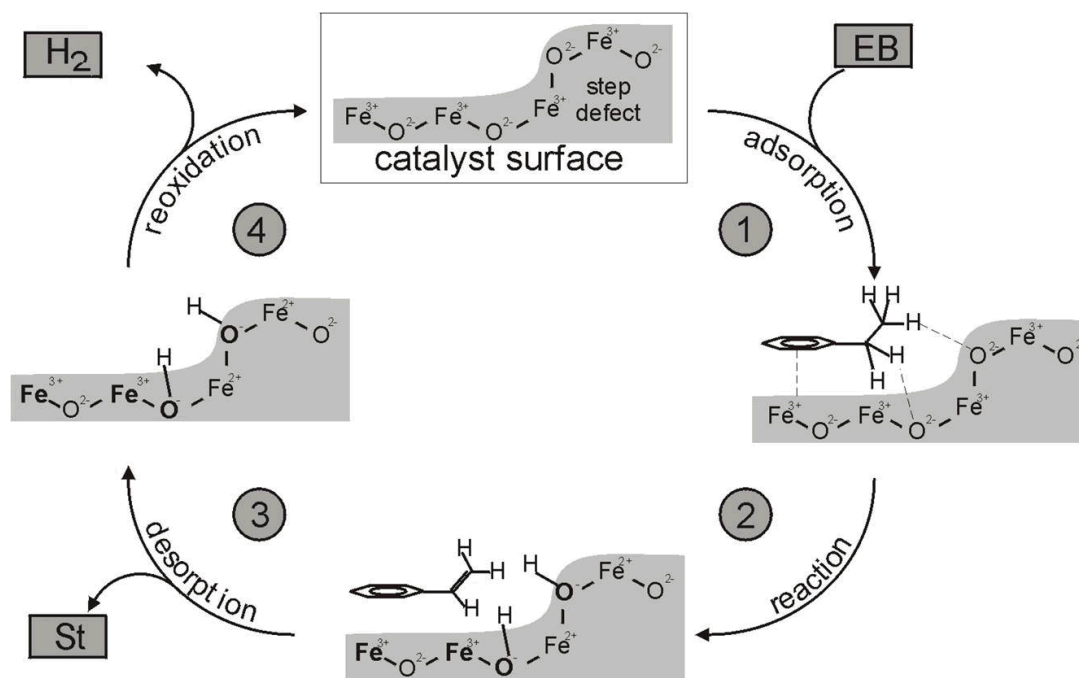


Fig. 5.3. EB dehydrogenation mechanism over the defects sites on the unpromoted (Fe_2O_3) [54]. Step 4 was found not to happen in case of reaction in presence of water alone. The reduction of the Fe_2O_3 to Fe_3O_4 was found to occur.

The adsorbate-substrate bond via the π -system of the benzene ring is responsible for holding the molecules long enough on the surface. Probably, they are mobile at the reaction temperature and move over the surface until they meet a defect site exposing basic oxygen which attracts the H atoms of the ethyl group and dehydrogenates it. Simultaneously, two Fe^{3+} ions in the vicinity are formally reduced to Fe^{2+} which explains why Fe^{3+} is necessary and why iron with its variable valency is essential. The formed styrene desorbs. The mechanism of H-removal from the catalyst and reoxidation of Fe^{2+} is speculative. However, the presented results show that a direct desorption in form of H_2 is possible. In the main reaction path, it is not removed as

H₂O by consuming substrate oxygen which later would have to be replaced by dissociation of water or by reaction with O₂ from the feed (Mars-Van Krevelen mechanism). Substrate oxygen is consumed but this is only a side reaction and leads to reduction of the substrate to Fe₃O₄ which is irreversible when only H₂O and no O₂ is added to the feed [90-92].

So far, nothing is known about the structure of the anticipated protection layer against K-removal on the promoted catalyst which possibly consists of K-carbonate, since the “protection” has to be effective for K only. At the reaction temperature the potassium hydroxide and carbonate mixture is molten, and under the conditions employed of 870 K and a high partial pressure of water vapour, KOH at these conditions is volatile, this was seen on the technical catalyst where the alkali is transported to towards the reactor exit. This loss is inhibited by the partial pressure of CO₂, which increases along the axis of the reactor (due to the gasification of coke). The major part of the alkali in the final section of the reactor is present in the form of relatively involatile potassium carbonate [1,2]. It could be that the local structure of the active sites consists of O above Fe³⁺, an arrangement similar to that on Fe₂O₃ as proposed by Muhler et. al. Fig. (5.3). Active sites for coke gasification could be surface K carrying a carbonate group, maybe by inclusion of surface O. Earlier results from infrared investigations [94] suggest that free potassium carbonate is not present, but that a complex is formed in which potassium and carbon are linked via an oxygen atom.

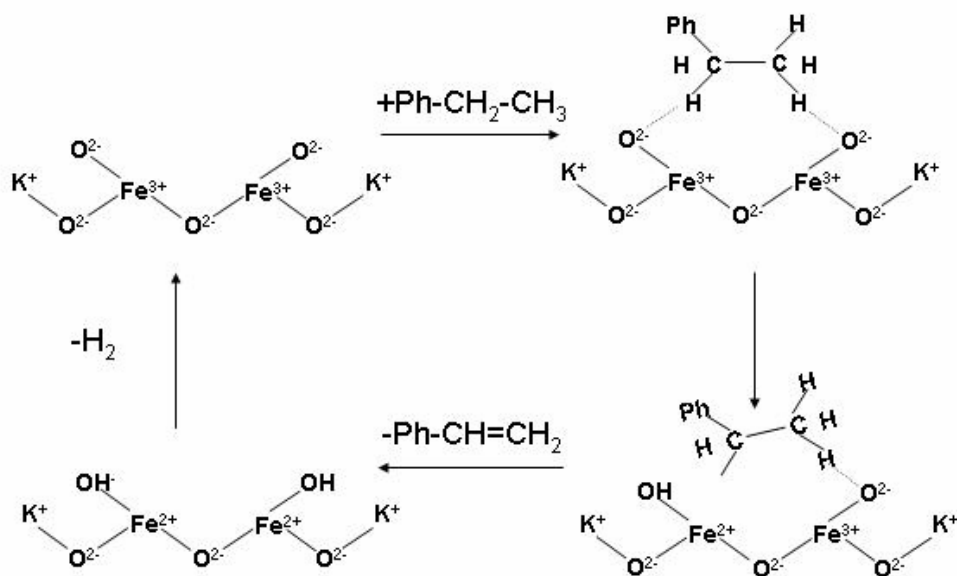


Fig. (5.4) Reaction mechanism proposed by Muhler et. al. [74] for the dehydrogenation of EB to ST over potassium promoted iron oxide catalysts.

Reactivation with water experiment on the promoted catalyst Fig. (4.13a,b) show that reactivation lead to regeneration of the high initial activity by gasification of the of coke deposits. On the other hand it leads to the acceleration of the potassium removal probably as KOH, which has a high vapour pressure at the reaction temperature. This correlates quite well with observations on the technical catalyst, where the results show that potassium at the inlet of the reactor is mainly converted to potassium hydroxide as a consequence of the high partial pressure of steam. This then accelerates the loss and redistribution of the potassium towards the outlet of the reactor or towards the center of the catalyst pellets as a consequence of the endothermicity of the reaction. This leads to a high concentration of the potassium at the outlet of the reactor and the in center of the pellets, and both (center of the pellets and outlet of the reactor) were found to show low or no activity which correlates to what was found on the model catalyst with high potassium contents [2]. The fast removal of the potassium by reactivation on the model catalyst, leads in turn to a

faster deactivation of the catalyst by the increase in the carbon deposits. Potassium removal or redistribution is thus the main reason for catalyst deactivation [95].

In the literature, it was proposed that KFeO_2 represents the catalytically active surface phase on promoted catalysts while $\text{K-}\beta''\text{-ferrite } \text{K}_2\text{Fe}_{22}\text{O}_{34}$ was supposed to be the bulk phase below, representing a K-reservoir for the reestablishment of KFeO_2 [7,8]. Previous studies on model catalyst preparation [20,21] indeed showed that KFeO_2 forms when a layer of K deposited on Fe_3O_4 is annealed at 700 K. Annealing to the reaction temperature 870 K results in a thin KFeO_2 layer or KFeO_2 islands on $\text{K-}\beta''\text{-ferrite}$ and at 970 K, no KFeO_2 is left. The surface is then most likely terminated by a full Fe-O-K layer forming an ordered 2×2 superstructure in LEED. Since surface and bulk composition are in equilibrium at temperatures above about 600 K [59], this surface layer can only be established when the bulk contains an amount of K which corresponds at least to sub-stoichiometric $\text{K}_x\text{Fe}_{22}\text{O}_{34}$ ($x \geq 0.67$). The K-promoted films in our study with $2 < \mathbf{I}_K/\mathbf{I}_{\text{Fe}} < 2.5$ surely consisted only of $\text{K-}\beta''\text{-ferrite}$ without any KFeO_2 on the surface. Nevertheless, they deactivate slowly and have a high conversion rate (Figs.(4.10, 4.13a, 5.1)). KFeO_2 which forms on the surface for $\mathbf{I}_K/\mathbf{I}_{\text{Fe}} > 2.7$ causes the initial rate to decrease further thus ruling out that it is the catalytically active phase. However, the deactivation proceeds even more slowly. It is thus likely that the role of active phase and reservoir phase is inverted, i.e. $\text{K-}\beta''\text{-ferrite}$ is the active phase and KFeO_2 represents the K reservoir. Intuitively this seems plausible. The coincidence of long-lasting high activity with the presence of the KFeO_2 phase does not necessarily mean that it is the active phase. It could be as well that the reservoir phase is necessary to guarantee at least the existence of a sub-stoichiometric of $\text{K-}\beta''\text{-ferrite}$ with Fe-O-K- termination while the stoichiometry and the surface K-content drops when the reservoir phase is consumed. The existence of

KFeO₂ would thus “buffer” the K-β”-ferrite phase against K-depletion by reaction with H₂O.

3- Pressed powder samples

Concerning the deactivation, phase transformation and its prevention by addition of oxygen, the results on the pressed powder samples agree well with the results on the model catalysts. The presented experiments show the validity of the model catalysis approach and the usefulness of surface science techniques in understanding complex catalyst and reaction mechanism. In so far the study represents a successful bridge over the material gap.

The results show that the clean pressed Fe_2O_3 powder catalyst has a high initial activity and it deactivates by reduction to Fe_3O_4 and by coke formation and by degradation of the catalyst as the SEM images, XRD and EDX characterization showed. Admitting some oxygen to the feed can help in maintaining higher conversions and prevents or decreases the rate of deactivation of the catalyst by preventing the reduction and decreasing the amount of carbon deposits. Fig. (5.5) compares the carbon peak on the powder samples after different treatments. The SEM images show that re-crystallization of the particles occurs and which was ascribed to reduction and reoxidation processes.

Quantitatively, the rates of St conversion on the pressed powder catalyst, it becomes clear that the rates on the powder catalyst is considerably lower if referred to its BET surface. Assuming equal rate, the accessible surface area of the powder catalyst is about five times the accessible geometric surface area. Due to mass transport limitations, not all pores are accessible. The results show that the catalyst is very active and there is no need to develop it, However an improvement may be expected from engineering and reactor design in order to allow the largest portion of the catalyst surface to be accessible to the reactants.

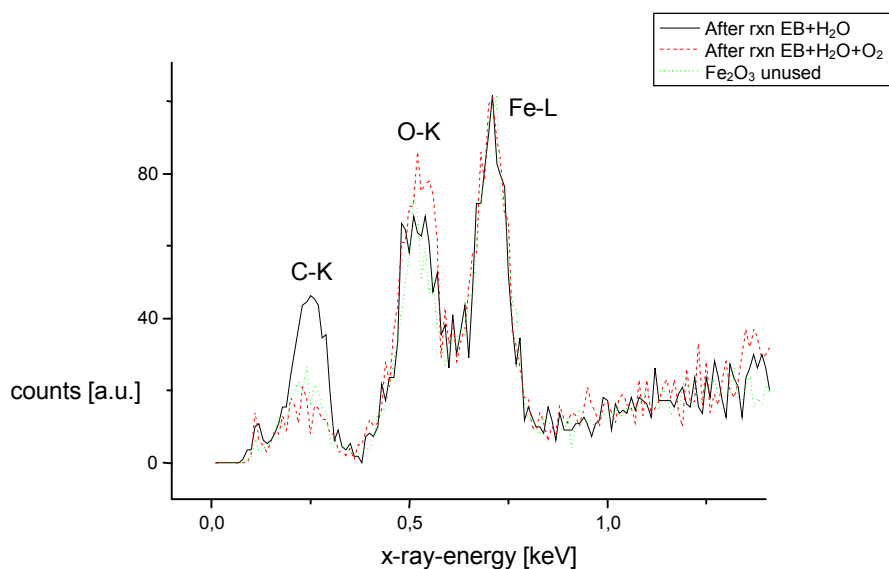


Fig. 5.5. Comparison of the EDX spectra for pressed powder samples after different treatments. The unused fresh pressed powder is also shown for comparison. The spectra are normalized to equal Fe-L intensity.

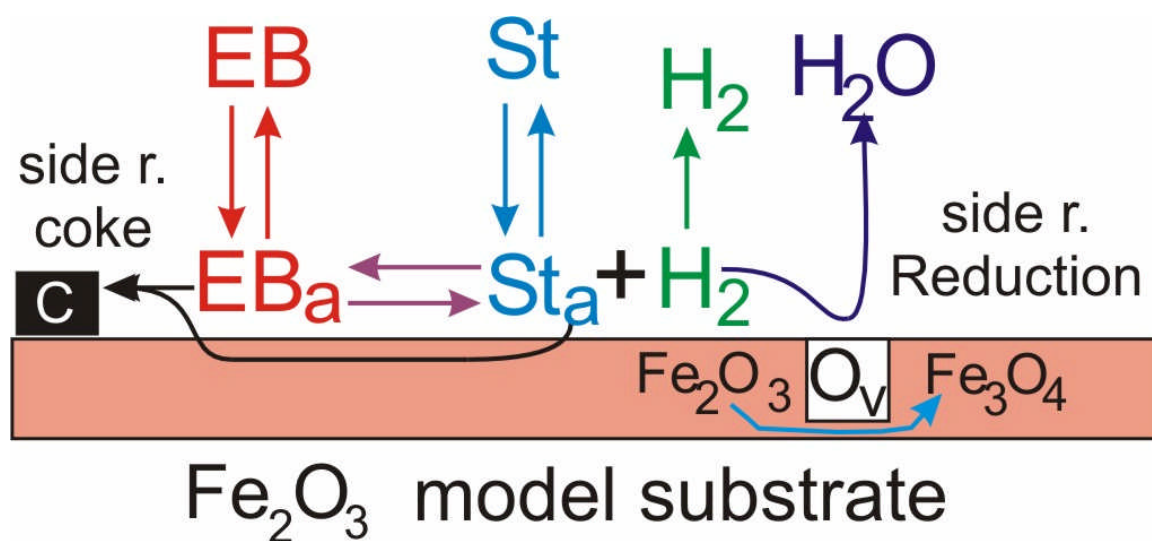
The low activity of the fresh powder samples shows that the catalyst needs to be activated by cleaning before use in order to obtain a high activity. This may explain why high initial activities have not been observed before on real catalysts.

The SEM images also show that the catalyst morphology changes under the reaction condition, the catalyst brittleness increases. This is in a good agreement with the results on the model catalyst where the roughness of the surface increases under reaction conditions.

5.4 Reaction formalism and catalyst model

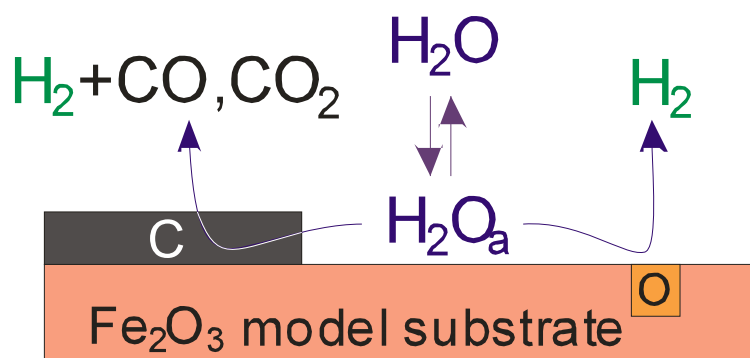
5.4.1 Unpromoted iron oxide model catalyst

From the presented results it was concluded that the reaction is catalytic and does not follow a Mars van Krevelen mechanism. It was also clear from the high activity observed that Fe^{+3} ions are essential for high catalytic activity. The deactivation of the unpromoted catalyst occurs by reduction to Fe_3O_4 and by accumulation of carbon deposits, scheme 4 illustrates the reaction mechanism.



Scheme 4. An illustrative scheme for the main and side reaction pathways of the dehydrogenation of EB over the unpromoted Fe_2O_3 model catalyst.

Water was found not to play a role in the rate determining step. It prevents the complete reduction of the iron oxide to metallic iron and limits reduction to Fe_3O_4 . Further it gasifies carbon deposits from the surface by the water gas shift reaction. The role of water is explained in scheme 5.

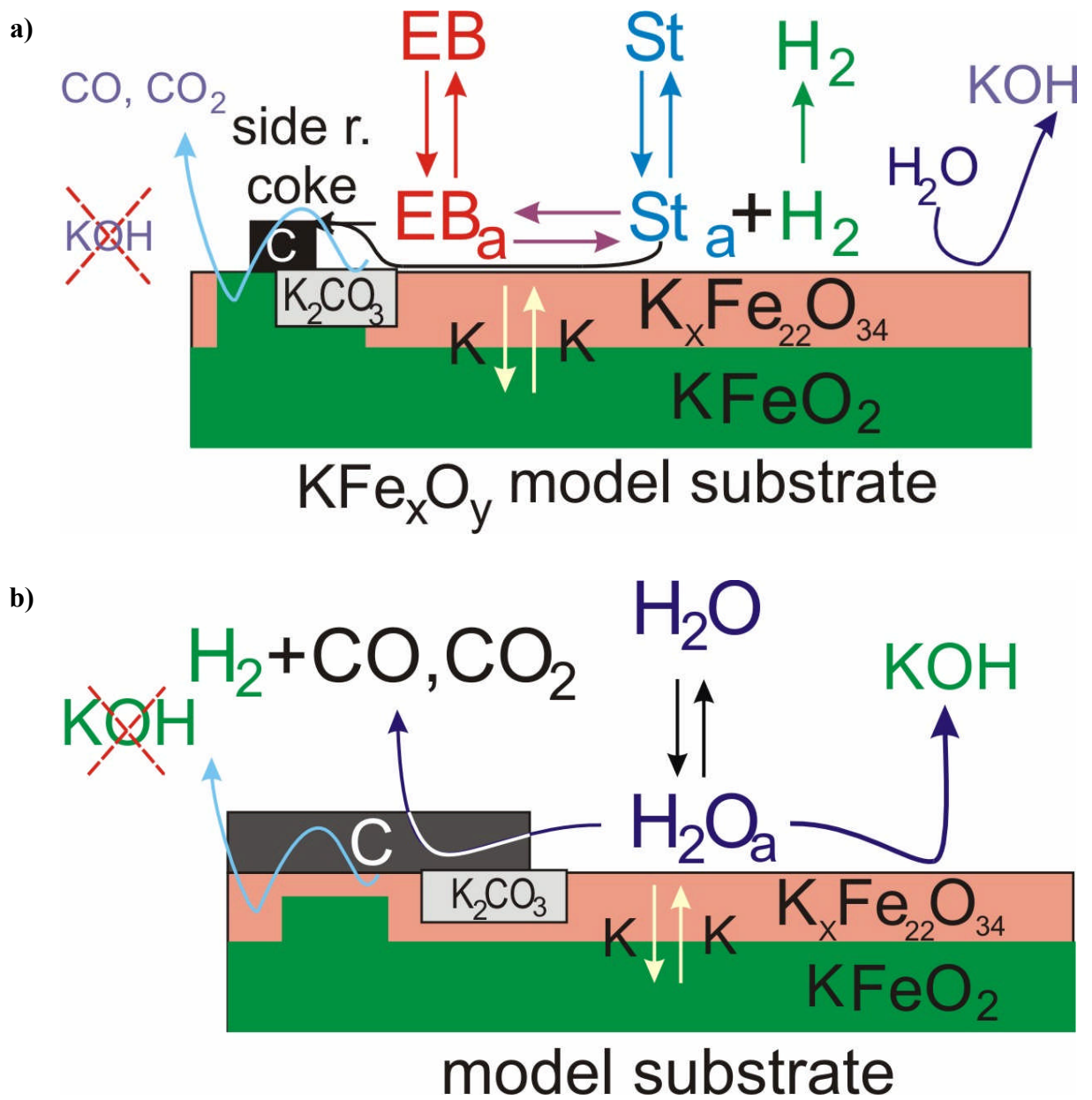


Scheme 5. An illustrative scheme explaining the role of water in preventing the complete reduction of the catalyst and the gasification of carbon deposits

5.4.1 Potassium promoted iron oxide model catalyst.

On the promoted catalyst the main reason for deactivation was found to be the continuous loss or redistribution of potassium from the catalyst. The potassium loss was found to be slower during reaction in the presence of EB than during reactivation with water alone. This could either be due to the presence of some kind of carbonaceous protection layer which seems unlikely or to the formation of a stable phase under the course of reaction like K_2CO_3 which is less volatile than KOH . Less carbon deposits are formed on the promoted catalyst K_2CO_3 is believed to be the active site for the coke gasification. Further, potassium was found also to play a role in preventing the reduction of the iron oxide phase.

The reaction mechanism and side reactions on the potassium promoted catalyst are shown and explained in scheme 6a, and b.



Scheme 6. a) The main and side reaction pathways over the potassium promoted iron oxide model catalyst. b) The role of water in the gasification of carbon deposits and the acceleration of potassium loss.

5.5 Conclusions

The pressure and material gap between reactivity studies in UHV and real catalysis can only be overcome by application of in-situ methods of catalyst characterization and activity measurements under realistic pressure and temperature conditions as has been done in this study. Well defined thin epitaxial films of the compositions $\text{Fe}_3\text{O}_4(111)$, $\alpha\text{-Fe}_2\text{O}_3(0001)$ and KFe_xO_y were prepared, transferred into a stagnation point micro flow-reactor for conversion measurements and afterwards transferred back for post-reaction surface characterization.

On unpromoted Fe_2O_3 , a high initial conversion was observed. Deactivation is caused both by reduction of Fe_2O_3 to Fe_3O_4 and by coking. Water added to the reactant is not involved in the main catalytic reaction. As proposed before, it is essential for gasification of carbon deposits thus limiting its amount. Further it limits reduction of the iron oxide to the oxidation state of Fe_3O_4 and prevents further reduction to metallic iron. The high initial conversion of Fe_2O_3 can be maintained by adding a small amount of oxygen to the feed. This prevents reduction and keeps carbon deposits at a low level. The main dehydrogenation path is a simple catalytic reaction and does not follow a Mars Van-Krevelen mechanism.

Potassium as promotor reduces the build-up of carbon deposits and prevents reduction of the oxide. The initial conversion rate decreases with increasing potassium loading, which is explainable by blocking of active sites by excess potassium. However, high potassium contents lead to slower deactivation by coking. KFeO_2 is not the active phase but serves as K-reservoir. Potassium is continuously removed during reaction, most likely in form of volatile KOH. The removal rate is considerably faster if the feed contains only water and no EB. It is suggested that EB, St or their decomposition

products react with potassium to form carbonate. “Steaming” the catalyst should thus be avoided. Oxidation in O₂ could be an alternative. Also on the promoted catalyst, it was possible to maintain a high activity by addition of oxygen.

Evidence is given that the existence of Fe³⁺ is not sufficient for high activity. The adsorption strength for EB and St is essential as well. The lower conversion on Fe₃O₄ relates with its higher adsorption strength which may lead to site blocking.

The use of pressed powder sample in the micro-flow reactor was successful and confirmed the results obtained on the model catalysts.

References

- [1] G. R. Meima and P. G. Menon, *Applied Catalysis A* 212 (2001) 239.
- [2] E. H. Lee, *Catalysis Review* 8 (1973) 285.
- [3] K. Kochloefl, in *Handbook of Heterogeneous Catalysis*, Edited by G. Ertl, J. Knözinger, and J. Weitkamp (VCH, Weinheim, 1997), Vol. 5, Chap. 4.3.2.
- [4] H. Ohlinger and S. Stadelmann, in *Ullmanns Enzyklopädie der technische Chemie*, Urban und Schwarzenberg, (Eds.), München-Berlin (1965), Vol. 16, p. 460.
- [5] Nova Chemicals Corp.,
www.novachem.com/investorrelations/reports/2000AnnualReport/FactBook2000.pdf
Supplemental Financial and Product Information 2000, 2000.
- [6] K.K. Kearby in *Catalysis*, P. Emmet, (Ed.), Vol.III, Rheinhold, New York (1955), p. 469.
- [7] F. Cavani and F. Trifiro, *Applied Catalysis A: General* 133 (1995) 219.
- [8] S. Carra and L. Forni; *Ind. Eng. Chem. Process Des. Dev.* 4 (1965) 281.
- [9] N.N. Lebedev, G.V. Odabashyan, et. al. *Kinet. Kata.* 18 (1977) 1177.
- [10] T. Hirano, *Applied Catalysis* 26 (1986) 65.
- [11] T. Hirano, *Applied Catalysis* 28 (1986) 119.
- [12] K. Coulter, D. W. Goodman, and R. G. Moore, *Catalysis Letters* 31 (1995) 1.
- [13] P. Tetenyi, Z. Paal, M. Dobrovolszk; *Z. Phys. Chemie* 102, 267 (1976).
- [14] W. P. Addiego, C. A. Estrada, D. W. Goodman, M. P. Rosynek, and R. G. Windham, *Journal of Catalysis* 146 (1994) 407.
- [15] M. Muhler, R. Schlögl, and G. Ertl, *Journal of Catalysis* 138 (1992) 413.
- [16] M.A. Gibson and J.W. Hightower, *J. Catal.* 41 (1976) 420.
- [17] I. Wang, J.-C. Wu and C.-S. Chung, *Appl. Catal.* 16 (1985)89.
- [18] M. Muhler, PhD thesis, Fritz Haber Institute, Berlin (1989).
- [19] H. Miura, et. al. *React. Kinet. Catal. Lett.*, Vol. 53, No. 2 (1994) 323-329.
- [20] W. D. Mross, *Catalysis Review - Science and Engineering* 24 (1983) 591.
- [21] R. L. Hirsch, J. E. Gallagher, R. R. Lessard, and R. D. Wesselhoft, *Science* 215 (1982) 121.
- [22] M. Muhler, J. Schütze, M. Wesemann, T. Rayment, A. Dent, R. Schlögl, and G.Ertl, *Journal of Catalysis* 126 (1990) 339.
- [23] B. D. Herzog, H. F. Rase, *Ind. Eng. Chem. Prod. Res. Dev.* 23 (1984)187.
- [24] R. A. Buyanov, V. V. Chesnovkov, A. D. Afanas;ev, V. S. Babenko, *Kinet. Catal.*18 (1977)839.
- [25] P. G. Menon, *J. Mol. Catal.* 59 (1990)207.
- [26] J. Lundin, L. Holmlid, P. G. Menon, L. Nyborg, *Ind. Eng. Chem. Res.* 32 (1990) 2500.
- [27] K. Engvall, L. Holmlid, P. G. Menon, *Appl. Catal.* 77 (1991) 235.
- [28] Ph. Courty, J. F. Le Page, *Stud. Surf. Sci. Catal.* 3 (1979) 293.
- [29] X. Yang, S. Weng, K. Jiang, L. Mao, Y. Euong, K. Jing, *Hyperfine Interactions* 69 (1991) 863.
- [30] W. J. Pöple, W. Büchele, A. Deimling, H. Peterson, Patent DE 4324905 A1 (1995), to BASAF AG.
- [31] G. E. Lewis, A. R. Smith, F. A. Sherrod, US Patent 4,804,799 (1989), To Dow Chemical.
- [32] P. W. Dellinger, R. G. Moore, F. A. Sherrod, A. R. Smith, US Patent 5,376,613 (1994), to Dow chemical.

- [33] T. G. Alkhazzov, et al. *Kinet. Katal.* 13 (1972) 509.
- [34] A.J. Bridgewater, R. Burch, and P.C.H. Mitchell; *Appl. Catal.* 4 (1982) 267.
- [35] D. Richard, P. Gallezot, D. Neibecker, and I. Tkatchenko; *Catal. Today* 6 (1989) 171.
- [36] A. Guerrero-Ruiz, A. Sepulveda-Escribano, and I. Rodriguez-Ramos; *Appl. Catal.A: Gen.* 81 (1992) 81.
- [37] M. Ledoux and B. Djelliulli; *J. Catal.* 115 (1989) 580.
- [38] K.M Minachev, V. V. Kharlamov, D.B Tagiyev, Z. G. Zulfugarov, *Zeolites* 4 (1984) 270.
- [39] A. Guerrero-Ruiz, I. Rodriguez-Ramos, *Carbon* 32 (1994) 23.
- [40] G.C. Grunewald and R.S. Drago; *J. Molecular Catal.* 58 (1990) 227.
- [41] T. Tagawa, K. Iwayama, Y. Ishida, T. Hattori, and Y. Murakami; *J. of Catal.* 79 (1983) 47.
- [42] Y. Murakami, K. Iwayama, H. Uchida, T. Hattori, and T. Tagawa; *J. Catal.* 71 (1981) 257.
- [43] G. Emig and H. Hofmann; *J. Catal.* 84 (1983) 15.
- [44] A. Schraut, G. Emig, and H. Hofmann; *J. Catal.* 112 (1988) 221.
- [45] G.E. Vrieland; *J. Catal.* 111 (1988) 1 and *J. Catal.* 111 (1988) 14.
- [46] G.E. Vrieland and P.G. Menon; *Appl. Catal.* 77 (1991) 1.
- [47] A. Schraut, G. Emig, and H.G. Sockel; *Appl. Catal.* 29 (1987) 311.
- [48] L.E. Cadus, O.F. Gorriz, and J.B. Rivarola; *Ind. Eng. Chem. Res.* 29 (1990) 1143.
- [49] G. Mestl, N. I. Maksimova, N. Keller, V. V. Roddatis, and R. Schlögl, *Angewandte Chemie, Int Ed* 40 (2001) 2066.
- [50] N. Keller, N. I. Maksimova, V. V. Roddatis, M. Schur, G. Mestl, Y. V. Butenko, V. L. Kuznetsov, and R. Schlögl, *Angewandte Chemie, Int Ed* 41 (2002) 1885.
- [51] Nadia Maximova, PhD thesis, Fritz Haber Institute, Berlin (2003)
- [52] T.G. Alkhazov and A.E. Lisovskii; *Kinet. Katal.* 17 (1976) 434.
- [53] E. Echigoya, H. Sano, and M. Tanaka; 8th International Congress on Catalysis, Verlag Chemie, Berlin, (1992) Vol. V, p. 623.
- [54] d.B. Tagiev, G.O. Gasymov, Z.G. Zulfugarov, and K.M. Minachev; 9th Actas Simp. Iberoam. *Catal.* 2 (1984) 944.
- [55] Guido Ketteler, PhD thesis, Fritz Haber Institute, Berlin (2003)
- [56] M. Boudart, *Top. Catal.* 13 (2000) 147-149.
- [57] G. Ertl, in: *Catalytic Ammonia Synthesis*, ed. J. R. Jennings (plenum, New York, (1983).
- [58] D. W. Goodman, R. D. Kelly, T. E. Madey and J. T. Yates, *J. Catal.* 63 (1980) 226.
- [59] G. Ketteler, W. Weiss, W. Ranke, and R. Schlögl, *Physical Chemistry Chemical Physics* 3 (2001) 1114.
- [60] equitherm version 3.0 VCH Scintefic software, VCH, Weinheim, (1993).
- [61] Muan, *Am. J. Sci.* 256 (1958) 171.
- [62] G. Ketteler, W. Ranke, and R. Schlögl, *Journal of Catalysis* 212 (2002) 104.
- [63] G. Ketteler, W. Weiss, and W. Ranke, *Surface Review and Letters* 8 (2001) 661.
- [64] G. Ketteler and W. Ranke, Interface-dependence of nucleation and self-assembly of ultrathin iron oxide films, 775 (2003), p. P6.1.1-P6.1.6.

- [65] G. Ketteler and W. Ranke, *Journal of Physical Chemistry B* 107 (2003) 4320.
- [66] C. Kuhrs, Y. Arita, W. Weiss, W. Ranke, and R. Schlögl, *Topics in Catalysis* 14 (2001) 111.
- [67] R.W.G. Wyckoff, in: *Crystal Structures*, second ed., vols, I-III, Inerscience, New York, (1982), p89.
- [68] R.M Cornell, U. Schwertmann, *the Iron-oxides*, VCh, Weinheim, (1996).
- [69] N. V. Dvoretiskii, E. G. Stepanov, T. N. Sudzilovskaya, G. R. Kotelnikov, V. V. Yun, *Inorg. Mater.* 25 (1989) 242.
- [70] N. V. Dvoretstii, E. G. Stepanov, Y. Yun, *Inorg. Mater.* 27 (1991) 1064.
- [71] I. Eleizer, R. A. Hiohard, *High Temp. Sci.* 10 (1978) 1.
- [72] Y. Joseph, G. Ketteler, C. Kuhrs, W. Ranke, W. Weiss, and R. Schlögl, *Physical Chemistry Chemical Physics* 3 (2001) 4141.
- [73] S. K. Shaikhutdinov and W. Weiss, *Surface Science* 432 (1999) L627-L634.
- [74] W. Weiss and W. Ranke, *Progr Surf Sci* 70 (2002) 1.
- [75] M. Ritter, H. Over, and W. Weiss, *Surface Science* 371 (1997) 245.
- [76] M. Ritter and W. Weiss, *Surface Science* 432 (1999) 81.
- [77] W. Ranke and W. Weiss, *Surface Science* 414 (1998) 236.
- [78] W. Ranke and Y. Joseph, *Physical Chemistry Chemical Physics* 4 (2002) 2483.
- [79] Y. Joseph, M. Wünn, A. Niklewski, W. Ranke, W. Weiss, C. Wöll, and R. Schlögl, *Physical Chemistry Chemical Physics* 2 (2000) 5314.
- [80] C. Kuhrs, Y. Arita, W. Weiss, W. Ranke, and R. Schlögl, *Topics in Catalysis* 14 (2001) 111.
- [81] S. K. Shaikhutdinov, Y. Joseph, C. Kuhrs, W. Ranke, and W. Weiss, *Faraday Discussions* 114 (1999) 363.
- [82] R. I. Masel, in *Principles of Adsorption and Reaction on Solid Surfaces*, (John Wiley & Sons, New York, 1996).
- [83] C. S. Fadley, M. A. VanHove, Z. Hussain, and A. P. Kaduwela, *Journal of Electron Spectroscopy and Related Phenomena* 75 (1995) 273.
- [84] Sh. K. Shaikhutdinov, R. Meyer, D. Lahav, M. Bäumer, T. Klüner, and H.-J. Freund, *Physical Review Letters* 91 (2003) 076102-076102-4.
- [85] W. Weiss, D. Zscherpel, and R. Schlögl, *Catalysis Letters* 52 (1998) 215.
- [86] D. Zscherpel, Freie Universität Berlin, FB Chemie, 1998.
- [87] G. Ketteler, W. Ranke, and R. Schlögl, *Journal of Catalysis* 212 (2002) 104.
- [88] C. Kuhrs, M. Swoboda, and W. Weiss, *Topics in Catalysis* 15 (2001) 13.
- [89] G. Ketteler and A. Schüle, (2003).
- [90] O. Shekhah, W. Ranke, A. Schüle, G. Kolios, and R. Schlögl, *Angewandte Chemie, Int Ed* 42 (2003) 5760.
- [91] O. Shekhah, W. Ranke, R. Schlögl. Submitted to *J. Catal.* 2004.
- [92] W. Ranke, O. Shekhah. Submitted to *Recent Research developments in Surface science* 2004.
- [93] M. Akimoto and E. Echigoya, *J. Catal.*, 35, 278 (1974).
- [94] I. L. C. Freriks, H. M. H. van Wechem, J. C. M. Stuiver, and R. Bouman, *Fuel*, 60 (1981) 463.
- [95] J. Matsui, T. Sodesawa, and F. Nozaki, *Applied Catalysis* 51 (1989) 203.
- [96] D. E. Stobbe, F. R. VanBuren, A. J. VanDillen, and J. W. Geus, *Journal of Catalysis* 135 (1992) 533.

Abstract

The economically important dehydrogenation of ethylbenzene (EB) to styrene (ST) is run at 870 K over potassium promoted iron oxide catalysts in the presence of steam. Here we present the continuation of model catalysis studies using thin epitaxial films (10-20 nm) of magnetite Fe_3O_4 , hematite $\alpha\text{-Fe}_2\text{O}_3$ and potassium ferrites KFe_xO_y of different composition. They allow the application of surface science methods for pre- and post-reaction surface characterization. The phases are identified from the LEED pattern and Auger (AES) spectrum. Catalytic conversions are measured using an in-situ stagnation point micro-flow reactor. The standard feed consists of EB: H_2O =1:10 (molar). The partial pressures of reactive gases ($p(\text{EB})$ and $p(\text{H}_2\text{O})$) are 3.3 and 33 respectively, the rest working pressure of 1 bar is He. The standard total flow rate is 25 ml/min. In addition, O_2 can be introduced or H_2O can be switched off. The low film thickness is an advantage; the whole “bulk” material is essentially in thermodynamic equilibrium at reaction conditions. The nature of the films also excludes pore diffusion effects.

When starting with Fe_2O_3 the high initial conversion drops within about 80 min by about an order of magnitude. Simultaneously, the film is reduced to Fe_3O_4 and covered by coke. Without water in the feed, the deactivation behaviour is similar but substrate reduction proceeds towards metallic iron and coking is heavier. This confirms that water is not involved in the catalytic reaction but it prevents substrate reduction beyond Fe_3O_4 and help in coke gasification. We conclude further that the final low activity is connected to coke. Addition of O_2 prevents both reduction and coking and the high initial conversion is maintained. The necessary amount of O_2 corresponds to that necessary to oxidize the produced H_2 and to gasify the coking products. Initial deactivation of the promoted catalyst is much slower and occurs mainly by coking which is counteracted by surface K, possibly as K_2CO_3 . K accumulates at the surface but is in equilibrium with the bulk concentration. It is slowly but continuously removed during reaction which accounts for a slow irreversible deactivation. “Steaming” the catalyst by switching off EB but continuing the water admission causes removal of coke but also a fast removal of K. We conclude that in the presence of EB and its reaction- and decomposition-products, surface K is protected against removal, possibly because it forms carbonate. Substrate reduction is also prevented by K. Striking is the similarity of the initial conversion rates for unpromoted and promoted catalysts. Since Fe_3O_4 also contains Fe^{3+} but is much less active, we believe that the existence of Fe^{3+} is necessary but not sufficient. As proposed before, the adsorption strength for EB and St may be essential. Both are bound so tightly on Fe_3O_4 that they may block the active sites. Investigations over the promoted catalyst with different potassium loadings show that the potassium rich phase (KFeO_2) is not the active phase, the β -ferrite $\text{K}_x\text{Fe}_{22}\text{O}_{34}$ is the active phase and the KFeO_2 is the potassium storage phase. The activation energy was found to be equal on the clean unpromoted and the promoted catalyst, which support that the active sites on both is the same. Unpromoted real catalysts in the form of pressed powder pellets were used for reactivity studies in the micro-flow reactor under the same conditions as for the model catalyst. The results show a good agreement but the conversion on real powder samples does not scale with the BET-surface, which means that there are diffusion limitations and not all the pores are accessible.

Zusammenfassung

Die wirtschaftlich bedeutende Dehydrierung von Ethylbenzol (EB) zu Styrol (St) wird bei 870 K über Kalium-promotierten Eisenoxid-Katalysatoren in Gegenwart von Dampf durchgeführt. Hier wird die Fortsetzung von Untersuchungen dargestellt, in denen dünne epitaktische Filme (10-20 nm) aus Magnetit Fe_3O_4 , Hämatit Fe_2O_3 und Kaliumferriten KFe_xO_y unterschiedlicher Zusammensetzung als Modellkatalysatoren verwendet werden. Das erlaubt, Methoden der Oberflächenanalyse vor und nach der Reaktion anzuwenden. Die Phasen werden mit Hilfe der Beugung langsamer Elektronen (LEED) und der Auger-Elektronenspektroskopie (AES) identifiziert. Katalytische Umsätze werden in einem in-situ Prallplatten-Mikroreaktor gemessen. Die Standardzusammensetzung des Edukts ist $\text{EB}:\text{H}_2\text{O}=1:10$ (molar). Die Partialdrucke der reaktiven Gase sind $p(\text{EB})=3.3$ mbar, $p(\text{H}_2\text{O})=33$ mbar, der Rest zum Arbeitsdruck von 1 bar besteht aus He. Der Standard-Gesamtfluss ist 25 ml/min. O_2 kann extra zugegeben und H_2O kann weggelassen werden. Die geringe Filmdicke ist ein Vorteil, da das gesamte Material im wesentlichen mit der Oberfläche im thermodynamischen Gleichgewicht ist. Der Film ist frei von Poren. Der anfänglich hohe Umsatz über Fe_2O_3 fällt innerhalb von etwa 80 min um fast eine Größenordnung ab. Gleichzeitig wird der Film zu Fe_3O_4 reduziert und mit Kohlenstoffablagerungen („Koks“) bedeckt. Ohne Wasser im Edukt verläuft die Deaktivierung ähnlich, allerdings wird das Substrat bis zum metallischen Eisen reduziert und verkocht viel stärker. Wasser ist also nicht an der katalytischen Reaktion beteiligt, verhindert aber die Reduktion über das Fe_3O_4 hinaus und unterstützt die Vergasung des Koks. Wir schließen weiterhin, dass die niedrige Endaktivität dem Koks zuzuschreiben ist. Zugabe von O_2 verhindert sowohl Reduzierung wie Verkokung und erhält den hohen Anfangsumsatz. Die notwendige Menge O_2 entspricht der Menge, die nötig ist, um das erzeugte H_2 und den Koks zu oxidieren. Die anfängliche Deaktivierung des promotierten Katalysators verläuft viel langsamer und geschieht vor allem durch Verkokung, der durch Kalium an der Oberfläche entgegengewirkt wird, möglicherweise in Form von K_2CO_3 . Im Gleichgewicht mit der Volumenkonzentration reichert sich K an der Oberfläche an. Es wird während der Reaktion kontinuierlich entfernt, was eine langsame irreversible Deaktivierung bewirkt. „Steaming“ durch Abschalten des EB unter Aufrechterhaltung der Dampfzufuhr bewirkt die Entfernung des Koks aber auch eine rasche K-Verarmung. Daraus folgt, dass K in Anwesenheit von EB und seiner Reaktionsprodukte gegen Austrag geschützt ist, möglicherweise weil es Karbonat bildet. K verhindert auch die Reduzierung des Substrates. Auffallend ist die ähnliche Höhe des Anfangsumsatzes für unpromotierte und promotierte Katalysatoren. Da Fe^{3+} auch in Fe_3O_4 enthalten ist, das aber viel weniger aktiv ist, glauben wir, dass Fe^{3+} notwendig aber nicht ausreichend ist. Wie früher vorgeschlagen könnte die Adsorptionsstärke für EB und St wichtig sein. Beide werden auf Fe_3O_4 so fest gebunden, dass sie aktive Plätze blockieren könnten. Messungen an promotierten Katalysatoren mit unterschiedlichem K-Gehalt zeigen, dass nicht das K-reiche KFeO_2 sondern das β -Ferrit $\text{K}_x\text{Fe}_{22}\text{O}_{34}$ die aktive Phase ist, während das KFeO_2 die K-Speicherphase darstellt. Die Aktivierungsenergie auf dem sauberen unpromotierten und promotierten Katalysator ist gleich, was die Annahme stützt, dass die aktiven Plätze auf beiden dieselben sind. Unpromotierte Realkatalysatoren in Form von Pulverpresslingen wurden unter denselben Bedingungen untersucht, wie die Modellkatalysatoren. Die Ergebnisse stimmen gut überein, aber der Umsatz skaliert nicht mit der BET-Oberfläche. Das deutet darauf, dass es Diffusionsbegrenzungen gibt und dass nicht alle Poren zugänglich sind.

Acknowledgement

First and foremost I should offer my thanks, Obedience and gratitude to God the great from whom we receive guide and help.

I would like to thank and express my appreciation to my supervisor **Prof. R. Schlögl** for giving me the opportunity, his advice and valuable discussions which made it this work successful.

I would like also to thank **Prof. Christman** for agreeing to be a member of my supervisory committee.

My Special and warmest thanks for **Dr. W. Ranke** for his patience , valuable discussions, continuous support, excellent cooperation, support, motivation, care and friendship.

Special thanks to **M. Swoboda** for his great support and help in solving the technical problems, cooperation und good friendship.

I would like to extend my gratitude to Achim Achüle and Grigor Kolios from the ICVT-University of Stuttgart for good cooperation in this joint project.

I would like to extend my gratitude to my colleagues **G. Ketteler, Y. Joseph D. Frickel, S. abourous, O. Kreilenko, R. Ahmed and all other colleagues in the inorganic chemistry department in the Fritz haber institute.**

Special thanks to my father, brothers and sisters for their support and encouragement.

Last and not least best regards for the DFG for the financial support of this project.

Osama Shekhah

Personal data

- Date of birth: 22-10-1973
- Place of birth: Jordan.
- Nationality: Jordanian.
- Marital state: Single.

Education

- 1979-1991 Elementary and secondary education, Jerash-Jordan.
- 1991-1995 B.Sc. in Chemistry at Yarmouk University, Irbid-Jordan.
- 1995-1997 M.Sc. in Inorganic Chemistry at Yarmouk University, Irbid-Jordan.
- 2001-2004 PhD. in Inorganic and Industrial Chemistry at Free University of Berlin in cooperation with Fritz-Haber-Institute, Berlin, Germany.

Job History

- 1995-1997 Teaching at chemistry department in yarmouk university , rbid, Jordan
- 1998-2001 Researcher in ICC at the royal scientific society, Amman, Jordan.

List of publications:-

- 1) Mahmoud SS, Arafa IM, Shekhah OI
Sol-gel synthesis, characterization and catalytic activity of Pd supported on silica and siloxane-modified silica
ASIAN J CHEM 12 (4): 1047-1056 OCT-DEC 2000
- 2) Veser G, Kuhrs C, Shekhah O, et al.
Towards the unravelling of catalytic reaction kinetics: Styrene synthesis over iron oxide catalysts
ABSTR PAP AM CHEM S 223: 033-CATL Part 1 APR 7 2002
- 3) Osama Shekhah, Wolfgang Ranke*, Achim Schüle, Grigorios Kolios, Robert Schlögl
Styrene Synthesis: High Conversion over Unpromoted Iron Oxide Catalysts under practical working conditions**
Angewandte chemie International edition 2003, 42, 5760-5763
- 4) Osama Shekhah, Wolfgang Ranke*, Achim Schüle, Grigorios Kolios, Robert Schlögl
Styrolsynthese: hoher Umsatz über unpromotierten Eisenoxidkatalysatoren unter prktischen Arbeitsbedingungen
Angewandte chemie 2003, 115, 5938-5941
- 5) O. Shekhah, W.ranke, R.Schögl
Styrene synthesis: In-situ characterization and reactivity measurement over unpromoted and K-promoted iron oxide model catalysts
Journal of catalysis. Accepted 2004
- 6) Wolfgang Ranke , Osama Shekhah
Surface science meets catalysis research: Iron oxide films for in-situ model catalysts
Review to Recent research developments in surface science. submitted February 2004